# Fluid Flow in Complex Porous Media: A Study of Spatial Correlation, Disorder and Deformation

**THOMAS DARWENT**

A thesis submitted in partial fulfillment of the requirements

of Nottingham Trent University for the degree of Doctor of

Philosophy

May 31, 2022

# Abstract

Fluid flow through porous media is studied for its importance to natural and industrial systems, such as oil recovery and $CO_2$ sequestration. In these scenarios, a fluid invades a porous medium and displaces or mixes with fluid that already exists there. This thesis focuses on how complexities arise in such processes when the connectivity of the pores is considered. In addition to the overall disorder in a system, the ways in which pores connect with each other have a significant effect on fluid invasion and mixing within a porous medium. Here, I develop and employ experimental techniques for exploring this connectivity in a variety of scenarios. First, spatial correlations in the pore-scale properties are introduced in the context of fluid-fluid displacement. Increasing the correlations' range leads to increasingly large areas of similarly-sized pore throats and more asymmetric invasion patterns with lower interfacial area and a lower fraction of trapped defending fluid. This work helps to show under what conditions spatial correlations will impact mixing and reactions in a porous medium. The second project investigates transport phenomena in disordered porous media. I inject a dyed fluid phase and observe how it mixes with a miscible, undyed defending fluid. A small level of disorder promotes mixing around the porous system. However, for higher disorders mixing is then restricted, as larger patches of obstacles collectively hinder flow. This work has significance in understanding how organisms will organise themselves to efficiently transport nutrients. Finally, I investigate the effect of a deformable porous medium. For elastic obstacles, the pressure drop of an interface trapped in a pore throat causes that throat to deform. I investigate this regime and explore how disorder restricts the appearance of fracture-like patterns. A group relating the change in pore shape due to elastic effects, relative to natural size variations, is shown to control the pattern selection. Fracture-like invasion patterns are found to be more strongly favoured when fluid is injected at a constant flow rate, as opposed to constant pressure.

# Acknowledgments

There are numerous people who have helped and given me guidance on the projects I have worked on throughout my thesis, all of which I would like to thank.

My Director of Studies, Dr. Lucas Goehring, has been invaluable throughout my PhD. He has guided me through difficult times and has dedicated so much of his time to supporting me and helping me become a better researcher. Without his support, this work would not be possible.

My supervisor and independent assessor, Dr David Fairhurst and Professor Carl Brown, who have provided me with support and guidance throughout.

My collaborators and co-authors, Ran Holtzman, Enrico Segre, Oshri Borgman, Felix Meigel, Karen Alim, Leonie Bastin and Soumyajyoti Biswas. All of whom have been superb colleagues to work with, helping me not only with our joint projects but also helping to support this thesis.

My lab colleagues, in particular Mixon Faluweki, Megha Emerse and Jay Marsden, who have given me endless encouragement and whom I will remain friends with for years to come.

The faculty at Nottingham Trent University who have helped immensely with my work and provided valuable resources to help make this thesis happen.

Finally, my biggest thanks goes to my wife and son, Nicola and Alexander. The past few years have been some of the most challenging years I've had and without their love and support I would not have been able to finish this work. Their encouragement and belief in me has kept me going and there is not enough thanks I can give them.

# List of Publications

**Published Paper**

O. Borgman, T. Darwent, E. Segre, L. Goehring, and R. Holtzman. Immiscible fluid displacement in porous media with spatially correlated particle sizes. *Advances in Water Resources*, **128**, 158–167, 2019

**Paper In Preparation**

F. Meigel, T. Darwent, L. Bastin, L. Goehring, and K. Alim. Transport dynamics in porous media emerge from junction and not pore statistics. *In preparation*, 2021

# Table of Contents

# List of Figures

# Chapter 1

# Introduction

## 1.1 Pattern Formation

### 1.1.1 Pattern Formation In Nature

Pattern recognition is a key component of the evolution of humans and our survival throughout history, whether this is because of our ability to recognise patterns on predators or to avoid consumption of poisonous plants by their color and shape. Even now, when most humans throughout their daily life do not have to be concerned with this type of survival, pattern recognition is still an integral part of our daily lives. From babies recognising sound patterns so they can understand how to communicate to predicting trends in market prices and the spread of diseases, patterns allow us to predict the outcome of an event, given some initial inputs.

It is easy to see patterns in nature on a daily basis, and indeed most people will do so simply by seeing themselves in a mirror. It is a common property of animals to be arranged symmetrically and it is simple to understand why. This could be for survival, for instance in the case of a fish, a symmetric body plan will allow it to be more streamlined, allowing it to avoid predators. It could also be for reproduction purposes. Studies have shown that a more symmetric face is found to be more attractive and an indication of how suitable of a mate an animal would be [1,2]. However, it is possible for symmetries to be broken by small fluctuations that eventually determine a system's properties. One of the first recorded cases of this was detailed by Jacobi in 1834 [3]. Jacobi discussed the various shapes a rotating body of fluid could take in hydro-static and gravitational equilibrium. If the kinetic energy compared to the gravitational energy exceeds a certain critical point, the axial symmetry of the fluid is broken while still being in equilibrium. This is known as a Jacobi ellipsoid.

Patterns, though, are not only defined by their symmetry. In fact, it is rarer to find a symmetric pattern in nature than one that is disordered and irregular. This is not to say structures that are disorderly do not contain some hidden pattern that is harder to describe. A fractal is an example of this kind of hidden pattern. In the case of fractals, these are geometric shapes that are repeated at smaller and smaller length scales. This type of phenomenon appears

in snowflakes, turbulent fluid flow [4] and even the rings of Saturn [5]. In these cases, viewing the structure at a smaller scale reveals no new details that weren't previously available. That is to say, each length scale is indistinguishable from any other.

For some time fluids have been known to display fractal and symmetric patterns, as previously mentioned. Leonardo da Vinci sketched the flow of water as far back as 1473 [6], carefully detailing the evolution of flow over time, turbulent currents and how obstacles changed the flow of the fluid. From these sketches he sought to understand the underlying effects that created these currents, and it is this which scientists still seek to understand to this day. We now know that these currents arise in various areas in nature, particular in planetary atmosphere. When layers of fluid pass each other in different directions, they drag on one another leading to turbulent motion which can cause spiral and wave like patterns that are visible on planets such as Jupiter and Saturn [7]. The same motion occurs in our own atmosphere, in the form of cumulus clouds which are formed from turbulence. Even with these chaotic flows, there is an underlying structure to their form but the sensitivity of these flows make it almost impossible to predict their future behaviour.

The appearance of patterns can easily lead an observer to believe that there is some intelligent designer carefully constructing the arrangement and detail of an object, but in modern times it is much more clear that these patterns arise from the underlying physics and chemistry of the universe. However, even to this day the mechanisms for generating these patterns are still not fully understood and have been, and still are, the focus of much research. This thesis aims to explore patterns that appear in a particular scenario that occurs, when a fluid enters a porous medium. In this case, there are known initial parameters that have been documented in previous works that allow us to predict, to a certain degree, the type of pattern we will see. However, as will be shown in this thesis, these parameters are not sufficient to fully understand what causes these patterns, as the level of disorder in the system can, itself, exert control over pattern selection.

### 1.1.2 Pattern formation In Porous Media

A porous medium is a system often containing revealing complex pattern formations. These systems consist of materials that contains open areas called pores. Fluids, which can be liquids or gases, can occupy these pores and even flow between pores under certain conditions. The material itself is usually some kind of solid structure, such as sponges [8] and metal foams [9], or is made up of a number of solid particles, such as soil or beads [10].

Generally, a porous medium is characterized by the porosity of the material, which is the

fraction of empty space, or void space, to the total volume of the material. There are numerous ways in which the porosity of a material can be measured, including CT scanning [11], mercury intrusion porosimetry [12] and water immersion porosimetry [13]. These techniques are essential as they allow for highly detailed mapping of a porous system, and in some cases, don't alter the properties of the porous medium in the process.

In many cases, the process that happens when a fluid enters a porous medium, an "*invading fluid*", is the displacement of a fluid already filling the porous system, a "*defending fluid*". There are generally two scenarios, either when the two fluids mix along their interfaces (the perimeter of the area that is filled by a fluid), or when they don't mix, called *immiscible* fluid displacement. This thesis investigates how varying parameters of the invasion, and in particular disorder, affects both these cases. The process by which a fluid invades into a porous medium is in part determined by the competing forces which push the invading fluid and those which try to resist the displacement of the defending fluid. The pressure across the interface of the two fluids can be described by the Young-Laplace equation [14]:

$$P = P_{nw} - P_w = \sigma(\frac{1}{r_1} + \frac{1}{r_2}) \qquad (1.1)$$

where $P$ is the capillary pressure, $P_{nw}$ and $P_w$ are the pressures of the non-wetting and wetting fluids respectively, $\sigma$ is the interfacial tension between the two fluids and $r_1$ and $r_2$ are the principal radii of curvature of the interface. A fluid is deemed non-wetting fluid is when the angle between the liquid–vapor interface and the solid–liquid interface, termed the "*contact angle*", is greater than 90°. When the two fluids meet, the fluid with the higher contact angle will have a lower "*wettability*" and may be classed as the non-wetting fluid in Eq 1.1.

Following on from this, we can write the Young-Laplace equation for an invading fluid in a circular pore throat [15]:

$$P_c = \frac{2\sigma \cos(\theta)}{a} \qquad (1.2)$$

where $P_c$ is the capillary entry pressure, $\theta$ is the contact angle between the invading fluid and the porous medium and $a$ is the pore throat width. This is shown by Fig 1.1. What this form of the equation gives us is a way to measure the pressure required to enter a pore throat. Therefore, for larger pore throats and greater values of $a$, the pressure required, $P_c$ is lower. Likewise, for narrower pore throats and smaller values of $a$, the pressure required is increased. For a porous medium made up of a variety of pore throat widths, the invading fluid will follow a convoluted path given its pressure fluctuations and enter through the possible pore throats with low enough capillary entry pressures.
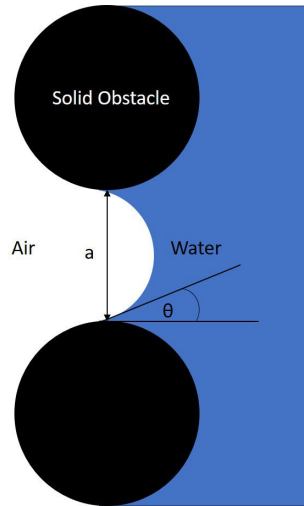
Figure 1.1: Diagram showing how the interface between two fluids, in this case air and water, is curved in a pore throat. The capillary entry pressure of a fluid into a pore is determined by the distance $a$, the interfacial tension $\sigma$ of the solid obstacles and the contact angle $\theta$ of the invading fluid.

The flow of fluid through a porous medium is also determined by properties of the fluids themselves, namely the viscosities of the invading and defending fluid. The viscous pressure drops in each fluid will mean that along the interface there will be a variety of capillary pressures which will also have an effect on fluid displacement. A dimensionless viscosity ratio, $M$, will then be a defining measure of the type of invasion that will occur:

$$M = \frac{\mu_i}{\mu_d} \tag{1.3}$$

where $\mu_i$ and $\mu_d$ represent the viscosity of the invading and defending fluid respectively. The importance that the viscosity ratio has on fluid invasion into porous media is demonstrated in Fig 1.2. The work done here by Aker et al. [16] shows simulations ran for two different viscosity ratios, when $\mu_d \gg \mu_i$, so $M \ll 1$, and for when $\mu_i \gg \mu_d$, so $M \gg 1$. The resulting patterns are dramatically different, showing a dendritic pattern for $M \ll 1$, and a compact front for $M \gg 1$.

Another important way to quantify the type of invasion that occurs is the dimensionless "*Capillary Number*", $Ca$. This value is the ratio of the viscous forces on a liquid to the interfacial tension between the two fluid phases. It can be written in the form:

$$Ca = \frac{\mu V}{\sigma} \tag{1.4}$$

where $V$ is a characteristic velocity. Thus the value of $Ca$ allows us to distinguish between different regimes of invasion. At low capillary values, capillary forces dominate. In these cases,

$M = 0.001$                    $M = 100$
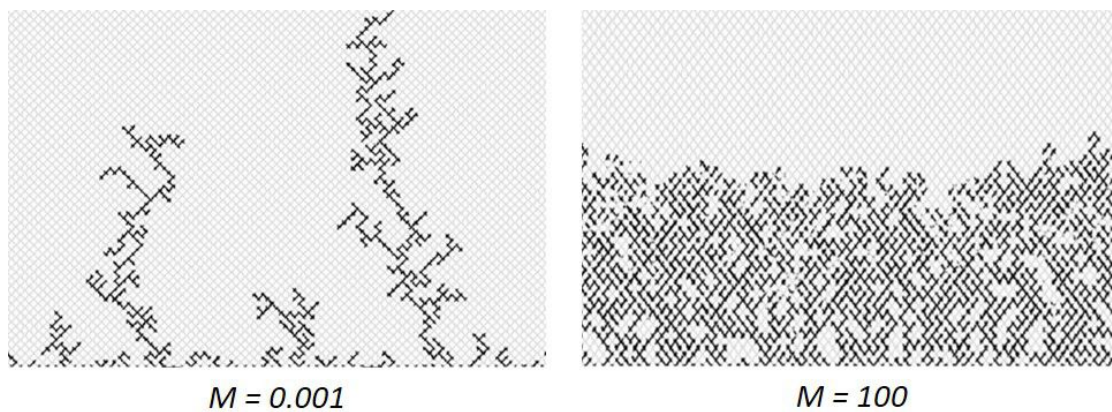
Figure 1.2: Simulations of two-phase drainage in a porous medium. The simulations are ran at two regimes, when $M \ll 1$ and the defending fluid viscosity is much greater than the invading fluid, and vice versa for when $M \gg 1$. Reproduced from [16].

the invading fluid will closely follow the geometry of the porous system, preferring to invade through the largest available pores. However, for high capillary values ($Ca > 1 \times 10^{-3}$) [17], these capillary forces become increasingly negligible when compared to the viscous forces at play, either from the rate at which a fluid is injected or the viscosity of the invading fluid. The effect that varying $Ca$ has on invasion patterns has been well documented [18,19] and is shown in Fig 1.3. In this experiment, a Hele-Shaw cell was used to investigate how air invaded into a water-glycerol saturated mono-layer of glass beads. A Hele-Shaw cell is made up of two-parallel flat plates which are separated by a small gap and here allows for studies of analogous 2-dimensional fluid flow in porous media. What Fig 1.3 shows is that as $Ca$ is increased, the invading air invades less and less of the porous system and has thinner fingers than at lower $Ca$. Therefore, whether varying the viscosity or the rate at which fluid is injected, the value of $Ca$ gives an indication of what patterns to expect.

The focus of much research, and of this thesis in particular, is into being able to predict the pattern produced by a fluid invading into a porous medium given initial conditions and known properties of the fluid and the porous medium. The purpose of such research has applications to many fields in industry and nature, ranging from $CO_2$ sequestration [20] to capillary vessels in the brain [21]. In many of these cases, the system is represented by some form of micro-model or numerical simulation [22] whereby a collection of particles, being something similar to pillars or beads, is trapped between a floor and a ceiling and a fluid is injected into the system at various rates. Using these replica systems, scientists are able to predict the evolution of fluid invasion in an actual system to some degree of accuracy. Recently, technological advances have allowed
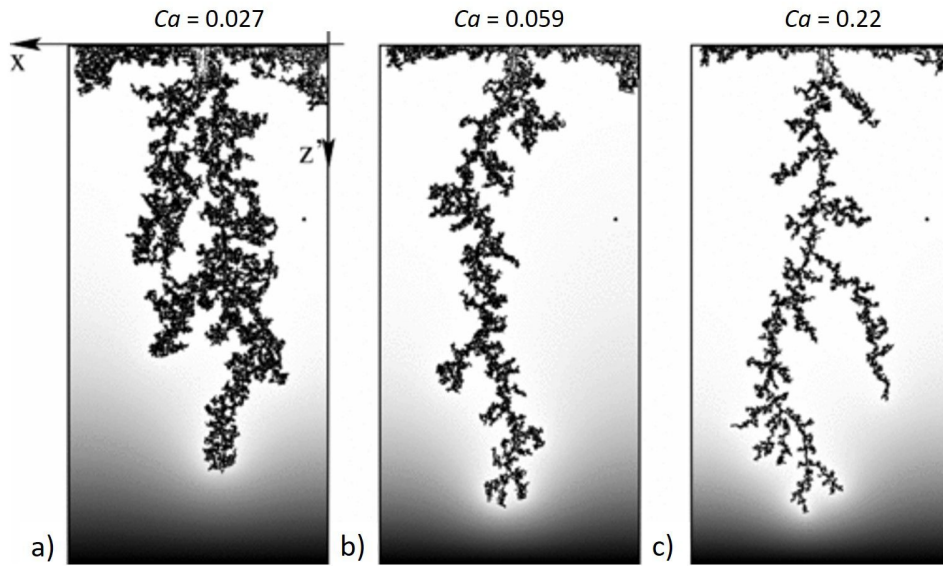
Figure 1.3: Invasion patterns produced by air invading into a water-glycerol saturated mono-layer of glass beads. Images from left to right shows effect of increasing $Ca$. Reproduced from [18].

researchers to obtain 3D images of a porous material and view the flow inside it to give even more accurate predictions of flow inside natural or industrial system [23].

The governing law for fluid flow through a porous medium is Darcy's Law and can be written as [24]:

$$Q = -\frac{kA}{\mu}\frac{(p_b - p_a)}{L} \tag{1.5}$$

where $Q$ is the volumetric flow rate, $k$ is the relative permeability of the porous medium, $\mu$ is the fluid viscosity, $A$ is the cross-sectional area of the porous medium, $(p_b - p_a)$ is the pressure drop across the medium and $L$ is the length of the medium. What this tells us is that fluid will flow faster through this porous medium if the medium is very permeable, or has a high porosity, or if there is a large pressure gradient across the medium.

However, fluid flow and the patterns produced within porous media cannot be determined nor understood by Eq 1.5 alone. There are several factors that determine fluid invasion into a porous medium. One of the simplest ways to affect the resultant pattern is to vary the rate at which the fluid is injected into a porous media. As shown in Fig 1.4, where a water-glycerol saturated packed bed of beads is invaded by air, just the effect of changing the injection rate creates a significant difference in the invasion pattern [25]. In this case, the granular media of beads are able to move and as the invading fluid enters the system, the pressure on the beads mean they become compact and close up their pore throats. For low injection rates, this leads
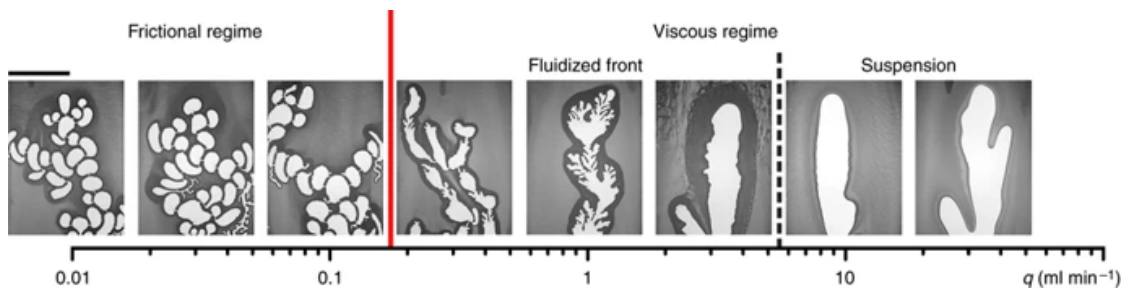
Figure 1.4: Air injection into a packed bed of polydispersed glass beads, packing fraction $\varphi = 0.58$, initially saturated by 50/50 water-glycerol solution. A stick-slip regime is prominent at low rates, transitioning into a standard viscous fingering regime as the injection rate is increased. Reproduced from [25].

to a build up in pressure and an eventual burst as enough pressure to invade the compact pores is reached. After invasion, the pressure is relaxed and the same process repeats. This results in the bubble-like pattern called the frictional regime. For higher injection rates, there is already enough pressure available for the invading fluid to burst through the compact pores and thus the bubbles transition into large finger-like structures.

Not only does how fluid is injected into a porous medium affect the resulting invasion pattern, but the initial geometry and properties of the medium it is being injected into also matter. Equation 1.5 shows how the flow rate of an invading fluid will be affected by the permeability of the system, for example. Experiments have already been undertaken that explore this by investigating the volume fraction of beads in a Hele-Shaw cell [26]. Shown in Fig 1.5 is a circular Hele-Shaw cell, where glass beads are contained between two glass plates and are mixed with a 50/50 water-glycerol solution. For air to invade via the central inlet, the solution is withdrawn from the cell using a syringe pump at a rate of 0.01 ml/min. This flow rate is chosen such that it is slow enough that viscous forces can be assumed to be negligible, $Ca \ll 1$.

What these experiments show is that previously well studied parameters such as the viscosity ratio, capillary number or porosity of the porous material, are not able to fully predict fluid invasion. The exact make-up of the material and how the material reacts to the invading fluid are complex factors which need to be explored to further understand the invasion patterns we see. In the following sections, I introduce some complex parameters that can be added to fluid invasion into a porous system and how these complexities affect invasion patterns.
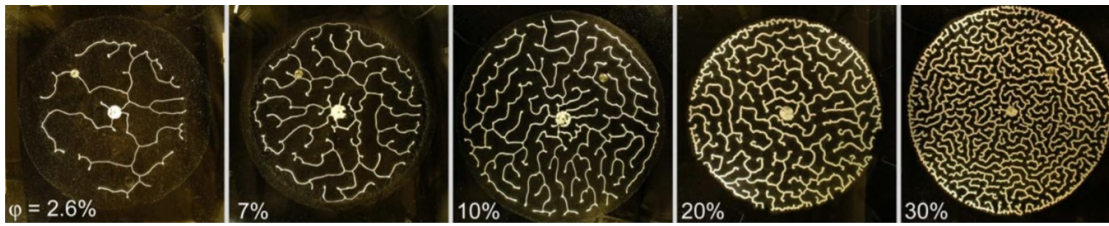
Figure 1.5: Glass beads mixed with a 50/50 water-glycerol solution held in a circular Hele-Shaw cell. Air invades via a central inlet by withdrawal of the defending fluid at a rate of 0.01 ml/min. The packing fraction of the glass beads increases from left to right, showing the effect this has on the invasion patterns. Reproduced from [26]

## 1.2 Disorder

Much work has been done investigating invasion patterns in porous media, where the obstacles that make up the medium are the same size or situated on a well-ordered lattice [27, 28]. In reality, this is often not the case, with a porous material being made up of obstacles with various sizes or positioned randomly within the system. What this leads to is a random assortment of pore throat sizes, which as has been described in Eq 1.2, has a direct effect on which pores are invaded. This "*disorder*" is then a factor in our understanding of invasion patterns in fluid-fluid displacement. However, given the random nature that makes up a disordered system, it is not a parameter which can be easily measured or quantified. A key goal of this thesis is to look at the effects of disorder on fluid transport in porous media, therefore, in ways where it can be more readily quantified.

Disorder, as mentioned, can be introduced by either positioning obstacles randomly throughout a system or by randomly varying the size of obstacles, for example which are otherwise on a well-ordered lattice grid. Much focus has been given to how introducing these types of disorders to various capillary numbers and viscosity ratios changes the invasion patterns [29, 30]. For example, shown in [31], is the effect disorder has on invasion patterns when both capillary number, $Ca$, and wettability, $\theta$ are varied. In this work, the porous system is made up of circular obstacles that are situated on a triangular lattice where a viscous fluid is displaced by an inviscid fluid via radial displacement. This means that the invading fluid enters via a central inlet and then invades the surrounding geometry radially outwards. In this case, disorder is introduced by giving each pillar a diameter, $d$, from a uniform distribution of width $\lambda$, $d \in [1\text{-}\lambda, 1\text{+}\lambda]\overline{d}$, where $\overline{d}$ is the average diameter of the pillars in the porous region. This tells us that for higher disorders, here characterised by the parameter $\lambda$, there will be a wider possible range of pillar sizes and
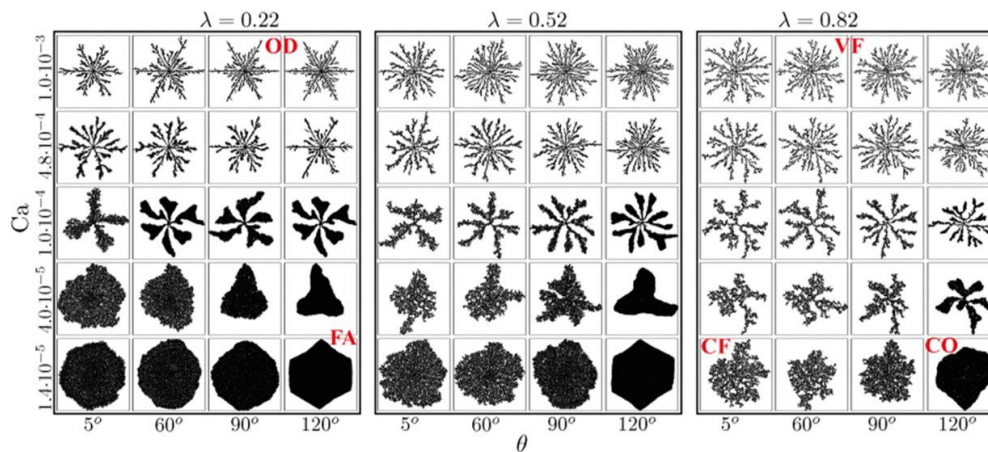
Figure 1.6: Simulated invasion patterns as $Ca$ and $\theta$ are varied for 3 different values of disorder, $\lambda$. Disorder is introduced by varying the size of the obstacles that are situated on an ordered lattice. Increasing $\lambda$ reduces how efficient the invading fluid is at displacing the defending fluid and reduces the effect of the underlying geometry. Reproduced from [31].

therefore a wide range of pore throat widths. The effect this type of disorder has on invasion patterns is shown in Fig 1.6. The figure shows how the patterns transition with varying disorder, as well as with $Ca$ and $\theta$. At high $Ca$, decreasing disorder transitions the patterns from viscous fingering (VF) to an ordered dendritic pattern (OD) as the effect of the underlying geometry shapes the invading fluid. At low $Ca$, the transition from high disorder to low disorder shows that there are less trapped clusters of defending fluid left behind, leading to a capillary fingering (CF) pattern, as the invading fluid explores more of the system. Increasing the wettability of the porous system at low $Ca$ and low disorder shows that the invasion pattern then creates a more faceted (FA) invasion pattern.

Clearly the geometry of the system, in particular the amount of disorder, is a major factor in understanding how fluid-fluid displacement in a porous medium works. Chapter 3 of this thesis expands on this notion in the context of fluid-fluid displacement and investigates how disorder when introduced again by random sizes of obstacles, is further complicated by adding a spatial correlation between like-sized obstacles, forming patches or areas where pillars of a similar size are grouped close together.

## 1.3  Dispersive Transport

In the cases mentioned previously, the invading fluid did not mix with the defending fluid during the invasion process. This creates some of the invasion patterns seen in Figs 1.3, 1.4 and 1.6.

However, in many natural and industrial cases [32–34], two fluids will mix with one another when the interfaces of each fluid meet, which can lead to the mixing or reacting of solutes or small particles within the fluids. This type of transport phenomena is crucial in sustaining life by mixing nutrients in an organism [35] or producing chemical energy [36]. Furthermore, the way in which the two fluid mix with each other, will have an effect on any invasion patterns within a porous medium, for example by creating precipitates capable of blocking up pore spaces [37].

There are two main ways in which a solute can be transported around a fluid. Firstly, diffusion arises from the random motion of molecules and will spread out a high concentration of solute into areas of low concentration. Secondly, dispersion of the solute arises from the motion of the fluid the concentration of solute is suspended in. What this means is that in non-uniform flow, where some areas of the fluid flow faster than other areas, the solute will be spread out as it samples different velocities. For flow in a simple tube, this can already occur due to drag on the tube wall, where solute in the center of the tube will flow faster than solute near the edge, thus spreading out the solute flow along the length of the tube.

As both methods of transport, diffusions and dispersion, occur simultaneously for solute in a flowing fluid, one method will tend to be favoured, in any situation, given the properties of the solute and the speed of the flowing fluid. This is quantified by the dimensionless Péclet number, which is the ratio of advective (transport of a solute by bulk motion of flow) to diffusive transport rate and can be written in the form:

$$Pe = \frac{\text{advective transport}}{\text{diffusive transport}} = \frac{Lu}{D} \tag{1.6}$$

where $L$ is a characteristic length, $u$ is the characteristic flow velocity and $D$ is the mass diffusion coefficient. This dimensionless group allows us the quantify which regime we are in for transport in a fluid. When $Pe > 1$, advective flow dominates and solute is spread out more due to the effect of dispersion. On the other hand, when $Pe < 1$, the speed of the fluid is slow enough that diffusion is the dominant effect on the transport of solutes within the fluid.

Shown in Fig 1.7, is the effect of greatly increasing $Pe$ on the flow of a tracer dye in a porous medium for two different porosities [38]. In this numerical work, tracer particles were tracked as they were injected into the system at $Pe = 24$ and $Pe = 2484$. In both cases, advective flow dominates over diffusive flow. This was further expanded upon by looking at the effect different porosities, here $\phi = 0.67$ and $\phi = 0.42$, would have on the mixing of tracer particles into the fluid-filled system. At the relatively low $Pe$, for $Pe = 24$, the tracer particles fill more of the porous system and have large mixing zones (yellow and green areas) between the bulk of the tracer particles (blue areas) and the fluid yet to mix with the tracers (red areas). However, when
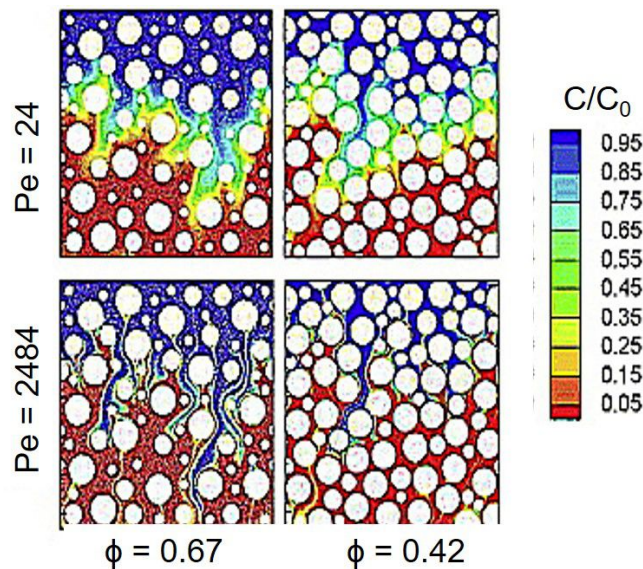
Figure 1.7: Distribution of relative tracer concentration at $Pe = 24$ and $Pe = 2484$. The simulations are ran for 2 values of porosity, $\phi = 0.67$ and $\phi = 0.42$. Reproduced from [38]

$Pe$ is greatly increased to $Pe = 2484$, these mixing zones are vastly reduced and the channels of tracer particles become more pronounced, creating thin lanes of tracer particles that prefer to sample the more open pore throats.

What this work shows is the $Pe$ has a significant effect on how particles or solute will mix with a defending fluid. For the same geometry, a fast flowing solution will inefficiently mix with the defending fluid and will instead create thin lanes of high-concentration fluid that travel through the porous region, with thin mixing zones around the boundary of each lane. The work done in [38] and shown in Fig 1.7, also looks into varying porosity. However, in Chapter 4 of this thesis, I will look at dispersive flows where the porosity is kept the same for varying values of $Pe$. Instead, disorder is introduced into the system by way of randomising the obstacle positioning. Investigated is how increasing degrees of disorder within a porous media can first promote and then inhibit the mixing of an injected dyed fluid into a miscible defending fluid.

## 1.4 Fracturing Patterns

As has been demonstrated so far, numerous experimental and numerical works have been conducted on rigid porous media and the effect that varying properties of the system can have on fluid invasion. What hasn't been studied to such an extent, however, is what happens when this medium becomes deformable under pressure. In most fluid-fluid displacement scenarios, an

a. viscous fingering     b. capillary fingering     c. fracturing
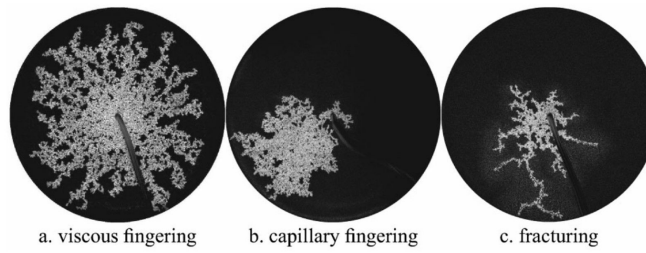
Figure 1.8: Experimental invasion patterns of air invading at a constant injection rate, $q$, into a confined water-saturated bed of beads with a weight, $w$, applied. a) q = 100 mL/min, w = 181N. b) q = 0.1 mL/min, w = 181N. c) q = 1 mL/min, w = 3N. Reproduced from [40]

invading fluid will exert a pressure of the surrounding solid material due to the pressure drop across the interface of the invading and defending fluid. In many natural systems, this would cause the positions of the obstacles that make up the porous system to be shifted or deformed, creating a coupling between the solid material of the porous medium and the fluid invading it. By using Eq 1.2 we can understand how fluid invasion would differ under these circumstances. As the obstacles that make up a pore throat are shifted or deformed, the pore throat width, $a$, will also change. As such, with widening and shrinking pore throats, the capillary entry pressure of each throat changes too. In fact, the widening of one throat will shrink any adjacent throat, and therefore restrict fluid flow through it. This scenario has significance in situations such as hydraulic fracturing [39] and $CO_2$ sequestration [20], where gases are pushed underground into porous material and deform the reservoir rock around it.

Some numerical and experimental work by [40] has investigated this effect and is shown in Fig 1.8. In this work, a plate is placed on top of a circular confined thin bed of water-saturated glass beads. Air is then injected via an external syringe pump into the center of the bed of beads. The plate is slightly smaller than the diameter of the bed of beads, such that the invading fluid will escape radially outwards towards the edge of the bed of beads. Key to this experiment is the weights placed on top of the plate. With increasing weight or confining pressure, the amount the beads are able to move decreases. The effect of this is shown in Fig 1.8. For the first two cases, figures 1.8a and 1.8b, the beads are confined by a weight of 181 N being applied. The creates a more rigid medium similar to those seen previously. An injection rate of 100 mL/min and 0.1 mL/min was used for 1.8a and 1.8b respectively. This creates the viscous and capillary fingering shown. However, for 1.8c, when the weight is reduced to only 3 N and an injection rate of 1 ml/min is used, the beads are able to be moved by the invading fluid. This creates a new *"capillary fracturing"* pattern which can be characterized by continuous thin fingers which invade only a relatively small section of the porous system.

What this work shows, is that if the obstacles that make up a porous system have a large enough elastic response, and the invading fluid exerts a large enough pressure to be able to change the pore throat width, a new pattern can be made. In this thesis much of the focus of chapter 5 is on how introducing disorder by way of particle sizes will restrict the pattern, causing a transition to a more crack-like pattern. Investigated experimentally is the production of these patterns for a porous system as a new dimensionless number, $\frac{\delta P}{P*}$ is varied. This dimensionless number is the ratio of elasticity, $\delta P$, to disorder, $P*$, in the obstacles in the porous medium and allows for a quantifiable way of determining if disorder or elasticity dominates the geometry.

## 1.5  Research Objectives

Here I present the objectives of this thesis:

- Implement novel experimental techniques to investigate the effects of disorder on fluid flow in porous media, using mechanical micromodels made via soft lithography.

- Introduce spatial correlations into microfabricated porous media to investigate its influence on fluid-fluid displacement.

- Explore mixing between a dyed and undyed fluid phase in a disordered porous medium, to determine how disorder affects dispersion.

- Use novel manufacturing techniques to investigate the effect of a deformable porous medium on invasion patterns.

# Chapter 2

# Methodology

## 2.1 Microfabrication

Throughout this thesis, I will be producing microfluidic chips as mechanical micromodels [41] to investigate how varying properties of the chip or fluid will have an effect on fluid-fluid displacement invasion patterns. To make these chips, I implement "*microfabrication*" techniques. This can refer to a number of different techniques, some of which are covered in [42]. However, in this chapter, I will outline the photo and soft lithography techniques that were used to create the microfluidic chips used in this thesis and highlight the particular aspects of the fabrication process that were altered for each project described in chapters 3,4 and 5. Further details, specific to each application, will be found in subsequent chapters.

### 2.1.1 Photolithography

Lithography itself is the process by which a pattern is imprinted on some kind of surface [42]. These patterns can be made into engraved molds which detailed reproducible objects can be easily made from. "*Photolithography*" refers to the lithographic process by which a pattern is imprinted onto a surface by exposing it to light. To do this, a mask is needed where the desired pattern is made opaque and light is not incident on the surface directly below the opaque pattern. To produce these masks, I created carefully designed patterns on a computer-aided design (CAD) software, QCAD. The details of each design will be explained later in the chapters where they are used. The designs are sent off to be made into 5 inch chrome photomasks by JD Photo Data. The masks are made out of a soda lime glass base material with a negative polarity. The masks use a 64k dpi resolution, meaning any features greater than 10 $\mu$m in size can be accurately printed onto the mask.

The manufacturing process is adapted from the manufacturer's recipes for the SU8-3000 series photoresists [43]. It starts with a silicon wafer being placed on a hotplate at 200°C. This is so the surface of the wafer becomes dehydrated and improves the coating process and the strength of the contact between the photoresist and the wafer. The wafer is then carefully placed into a spin coater contained in a fume cupboard so that the amount of dust that can contaminate the

surface is limited. A small amount ( 5 ml) of SU8 photoresist is then placed in the center of the dehydrated silicon wafer. SU8 is an epoxy-based negative photoresist, where upon exposure to UV, the photoresist becomes cross-linked and the remainder of the unexposed photoresist can be washed away. There are various SU8 photoresists with a wide range of viscosities, ranging from 45 cSt to 12,000 cSt [43]. Selecting the appropriate photoresist is therefore key to achieving the correct thickness during the coating process. For example, I used SU8-3025 photoresist, which is suitable for thicker designs up to about 100 $\mu$m in a single layer [43]. Once the photoresist has been placed on the silicon wafer, it is first spin coated by ramping up to with an acceleration of 100 rpm/s 500 rpm and held at this speed for 10 seconds. The speed is then increased to 1,000 rpm at an acceleration of 300 rpm/s and held at this speed for 30 seconds. The spin coater is then ramped down to 0 rpm at a deceleration of 300 rpm/s. This achieves a uniform thickness of around 60 $\mu$m of SU8-3025 photoresist across the wafer.

Once the photoresist has been coated into the silicon wafer, it is placed onto a hotplate again at a temperature of 65°C for 1 minute to reduce the stress on the layer. the temperature is then raised to 95°C for a soft bake. The length of time at which the wafer is baked at 95°C for depends on the thickness of the photoresist layer, but for my 60 $\mu$m layer, this was 20 minutes. This is an important step in the manufacturing process as it removes the solvent that exists in the photoresist and helps to solidify the layer. The reason the bake time differs is that for thicker layers of photoresist, it becomes more difficult to evaporate enough solvents. It is also important to perform this bake on a hotplate rather than in an oven. This is because in a convection oven, a skin may form on the photoresist layer which will make it harder for further solvent to evaporate.

Once the wafer has been appropriately baked, it can be exposed to a UV light through a photomask with the designed patterns. For the designs created in this thesis, this is done using a mask aligner (SUSS MicroTec MJB4). This piece of equipment places the photomask in direct contact with the top of the silicon wafer before exposing it to UV light. The usefulness of this equipment is that the photomask can be securely held and aligned with the wafer. The exact length of exposure can also be controlled. This is important as the length of exposure needed is dependent on the intensity of the UV from the mask aligner and the thickness of the photoresist layer. For a 60 $\mu$m thick layer, this is typically around 8 seconds. The patterned photomask is designed such that the pillar areas are opaque and therefore will mean the areas below these points are not exposed to the UV. This makes sense as we want these points to be wells in the photoresist. The wafer is then baked again after exposure at a temperature of 95°C. This is for usually a shorter amount of time (5 minutes) than the pre-exposure bake and is done to complete the polymerization of the SU8 photoresist. Again, an intermediate baking step at a temperature of 65°C for 1 minute is done to reduce the stress of immediately heating the wafer to 95°C.
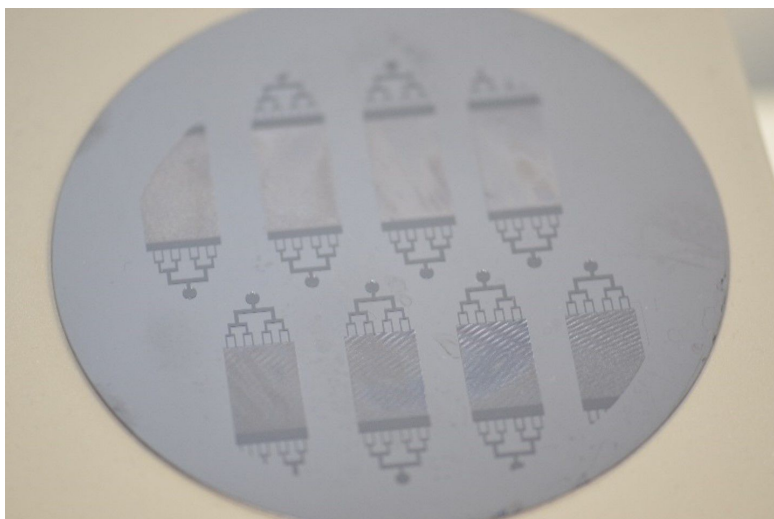
Figure 2.1: Photo of fully developed master mold created using photo-lithographic method. The raised darker grey patterns seen on the silicon wafer contain thousands of small divets which can be used to create chips with pillars of specific sizes in specific positions.

Once the photoresist is developed, the unexposed areas of photoresist are removed by submerging the wafer in microposit EC solvent. This helps to remove the unwanted SU8 photoresist and the wafer in the solvent bath is further placed in a sonicator to help agitate the photoresist layer and more effectively remove it. Again, the length of time that the wafer is agitated in the sonicator depends on the thickness of the photoresist layer, but for a 60 $\mu$m layer I typically used 9 minutes. After the wafer has been agitated, the unexposed photoresist layer can be washed away by first rinsing with isopropyl alcohol (IPA) followed by rinsing with de-ionised water. The wafer is finally cleaned by using a nitrogen jet to remove any remaining fluid on the wafer. An example of a completed wafer with a micromodel design appearing as an embossed pattern of photoresist is shown in Fig 2.1.

The reason this method is so effective in microfluidic experiments is that it is possible to produce microscopic features accurately and repeatedly following a set manufacturing method. Not only that, but the resulting master molds produced, for example shown in Fig 2.1, allows for multiple chips to be made using the same mold over and over again. The method for doing so is explained next.

## 2.1.2  Soft Lithography

Using the master mold created following the photo-lithographic method described in section 2.1.1, soft lithography can be utilised to create reproducible chips containing the designs imprinted on the silicon wafer master mold. This is done by pouring a liquid elastomer over the master mold,
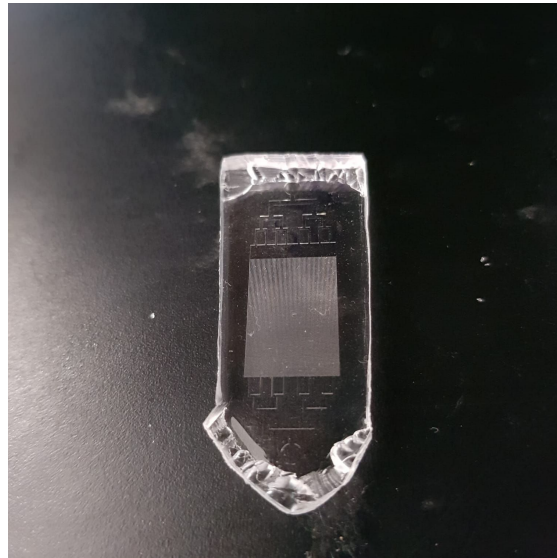
Figure 2.2: Example of a PDMS chip cut out of master mold. The PDMS chips have to be carefully cut and peeled out after being cured. The designs imprinted on the silicon wafer are also imprinted into the PDMS chips..

which in the case of this thesis is poly-dimethilsiloxane (PDMS). This is a combination of a sylgard 184 base and curing agent (Dow Corning), which is mixed at a particular ratio. The ratio of base to curing agent will affect how rigid the PDMS chips are. In all of the experiments in this thesis, the ratio of base to curing agent used is 10:1, giving a Young's modulus for the chips of about 1.5 MPa [44].

Once the base and curing agent has been properly mixed and poured over the master mold, the mixture is degassed in a vacuum chamber for 30 minutes. This removes any air bubbles in the mixture and on the surface of the wafer that would cause defects in the PDMS chip. Then the liquid elastomer can be cured by heating in an oven. To do this, a convection oven is preheated to a temperature of 75°C and the master mold and liquid elastomer are placed inside for 1 hour. This solidifies the PDMS but keeps it elastic enough to be easily removed from the master mold. This is done by carefully cutting around the designs on the master mold using a scalpel. The PDMS is then carefully peeled back to leave the designs on the PDMS chips. To create inlets and outlets for fluid to flow through, small holes are punched into opposite ends of the PDMS chips. An example of some PDMS chips cut out of the master mold is shown in Fig 2.2.

Because of how the master mold is made, the inlet areas stick out from the wafer and therefore will create depressions corresponding to open areas within the PDMS chips. On the other hand, any pillars in the PDMS will appear as holes in the master mold, and will therefore stick out of the PDMS chips. An SEM image of the PDMS pillars is shown in Fig 2.3. This SEM image
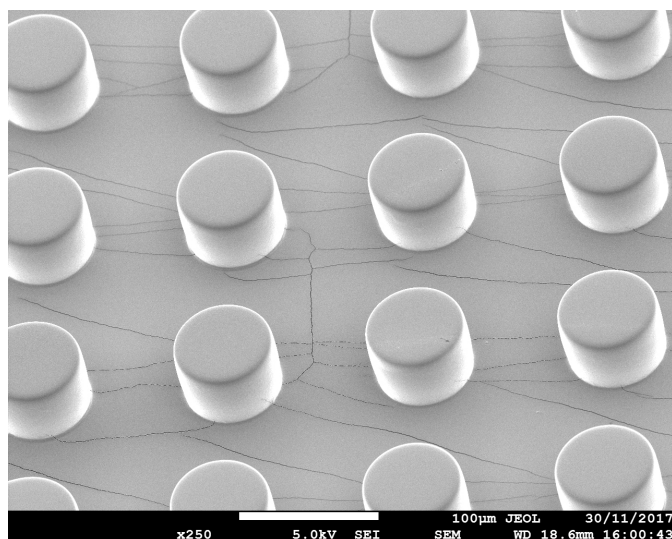
Figure 2.3: SEM image of PDMS pillars showing the uniformity of the final product of the soft lithography process. Cracks on surface of PDMS are due to the plasma cleaning process which hardens the surface of the PDMS

shows how the pillars stick out from the surface of the PDMS chips and are all almost identical to one another. This is down to the accuracy at which designs are imprinted onto the master mold using photo-lithography and how easily the pillars are removed from the master mold during the soft lithography step.

Separate to the production of the PDMS chips, glass slides are also coated with a thin layer ( 20 $\mu$m) of PDMS. To do this, a 10:1 mixture of sylgard 184 base to curing agent is made and a 5 ml drop of mixture is poured on the glass slide. This is then spin coated at a speed of 2,000 rpm, accelerated to at a rate of 300 rpm/s, and held at this speed for 30 seconds. The glass slides are then baked in a convection oven at 75°C for 1 hour. Once a set of PDMS-coated glass slides and PDMS chips have been made, the two are plasma cleaned so they can adhere to one another. The slide and chip are placed inside a plasma cleaner and a vacuum is created by withdrawal of air from the chamber. One plasma is created in the chamber, the slide and chip are left for 8 minutes. After this time, the plasma cleaner is switch off and air is allowed to fill the chamber. The slide and the chip can now be carefully stuck to one another, making sure not to create any air pockets as the two are stuck together. This now creates a porous region completely made from PDMS for which fluid can flow in and out of via the punched holes.

# Chapter 3

# Impact of Particle Size Correlations on Immiscible Fluid Displacement in Porous Media

The flow of fluids and gases in porous materials, such as soils and rocks, is complex and presents a challenge when attempting to understand their underlying physics. One of the main complexities in these systems is due to the disorder in the constituent particle sizes. In a natural system, particles will be a variety of sizes and therefore a system will have a wide variety of pore throat sizes which will affect the way fluid flows through the porous medium. Past work has been undertaken, both experimentally and numerically, in an attempt to better grasp the effect disorder has on fluid flow in a porous medium [31]. This work has particles situated on a lattice with the sizes of these particles given random radii between a specified allowed range of values. There is a defending fluid with a known viscosity initially saturating the system and a fluid is injected into the system with given input parameters. The effect that disorder has is then investigated by analysing the resulting invasion pattern.

This project looks to further investigate disorder in a system by implementing equivalent experimental and numerical analogue porous media. Experimentally, the analogue porous medium consists of an array of solid, cylindrical pillars on a triangular lattice, where heterogeneity is provided by variations in the pillar radii (Fig. 3.1).

Specifically investigated here is how changing the pillar sizes of a disordered system affects fluid flow into circular patches of such pillars. The range of pillar sizes is kept constant, but a parameter termed the "*correlation length*" is introduced where the size of the particles is varied. With increasing correlation length, the pillars are arranged so that similar sized pillars are relatively near to one another. A larger correlation length means that pillars with significantly different radii are placed further from one another, and this leads to increasingly larger areas of similarly-sized particles. Thus, areas containing large pore throats exists, which fluid flow favours over flow through the areas of large particles and narrow pore throats (3.2). This work
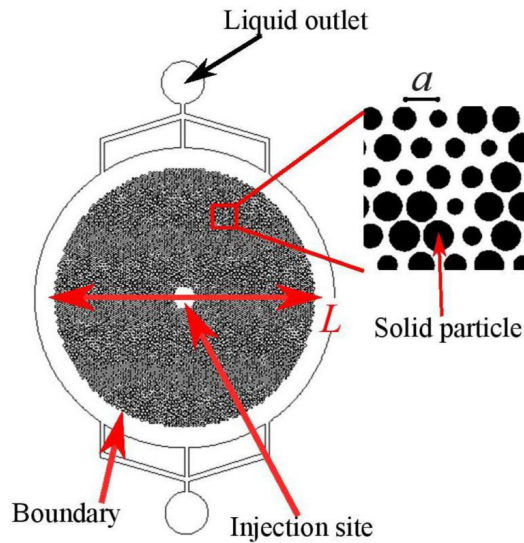
Figure 3.1: Experimental microfluidic cell design, showing a central air injection site, and a peripheral boundary zone connected to the liquid outlet ports. The porous medium of diameter $L$, is made of variably-sized cylindrical pillars placed on a triangular lattice with spacing $a$. A close-up view shows the variation in the size of the solid particles (pillars). Figure adapted from [45].

has been published in [45].

This is expanded further by investigating whether varying the capillary number, $Ca$, reduces the effect of particle size correlations or emphasises it. As introduced in Chapter 1, the capillary number is defined as the ratio of viscous forces to the surface tension between the two fluid phases. Here, it can be written in the form

$$Ca = \frac{\mu V}{\sigma} \tag{3.1}$$

where $\mu$ is the defending fluid's viscosity, $V$ is the characteristic velocity of the invading fluid, and $\sigma$ is the interfacial tension. In this case, the characteristic velocity $V$ is chosen to be the velocity at the edge of the pore space. This is the volumetric flow speed at which the invading fluid is injected into the system, divided by the open cross-sectional area of the cell's outer perimeter (the circumference of the circular porous region multiplied by the open fraction). The capillary number is an important number in fluid invasion and helps to categorise the type of invasion. For low values of Ca, capillary forces dominate, whereas for higher values of Ca, viscous forces will instead dominate.

The soft lithography and microfluidic manufacturing methods used here, outlined generally in chapter 2, allow for a wide variety of designs, for instance other ordered lattices [22] or random
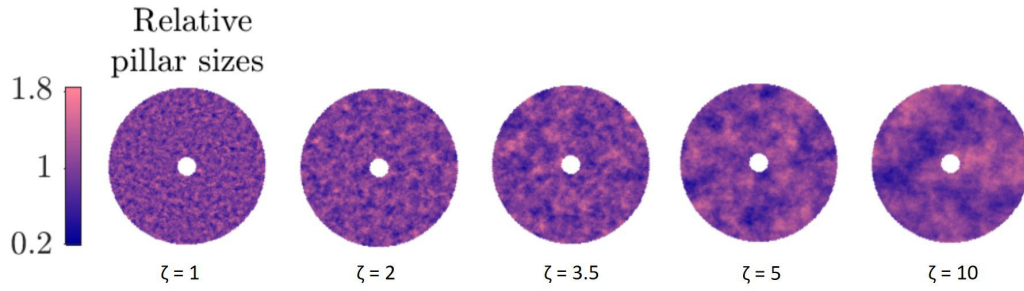
Figure 3.2: Colourmap of porous system with increasing correlation length, $\zeta$. Pink and blue areas represent large and small pillar respectively. With increasing correlation length, there are areas where similar sized pillars are grouped together.

pillar arrangements.

The experiments exploit microfabrication techniques, along with high-precision syringe pumps and cameras, to provide pore-scale observations of exceptional resolution and enable verification of the modeling results in order to provide better insight on the pore-scale physics of fluid invasion is disordered systems. The simulations, produced by Oshri Borgman, Enrico Segre and Ran Holtzmann, are based on the model of [46], and are compared with the microfluidic experiments of similar pore geometry. This model provides a mechanistic description of partially-wetting fluid-fluid displacement, and represents the basic interplay between capillary and viscous forces, invasion dynamics and wettability.

First described in this chapter is a summary of the geometry used for both the experiments and simulations, followed by the specific setups and techniques used for both sides of the project. The results of both are then presented and compared with one another to help consolidate their reliability. The impact these results have on the current understanding of fluid flow in complex porous media is then discussed and concluded.

## 3.1 Numerical Simulations, Experimental Setup and Image Analysis

### 3.1.1 Sample Geometry, Numerical Simulations

The sample geometry used for the numerical simulations is sketched in Fig 3.1 and consists of a circular cell of diameter $L = 120a$, containing cylindrical pillars on a triangular lattice, where $a = 45$ $\mu$m is the lattice constant (the distance between the centers of two adjacent pillars). The pillars, as well as the cell, have a height of $h = 65$ $\mu$m. Their diameters $d$ have a mean size
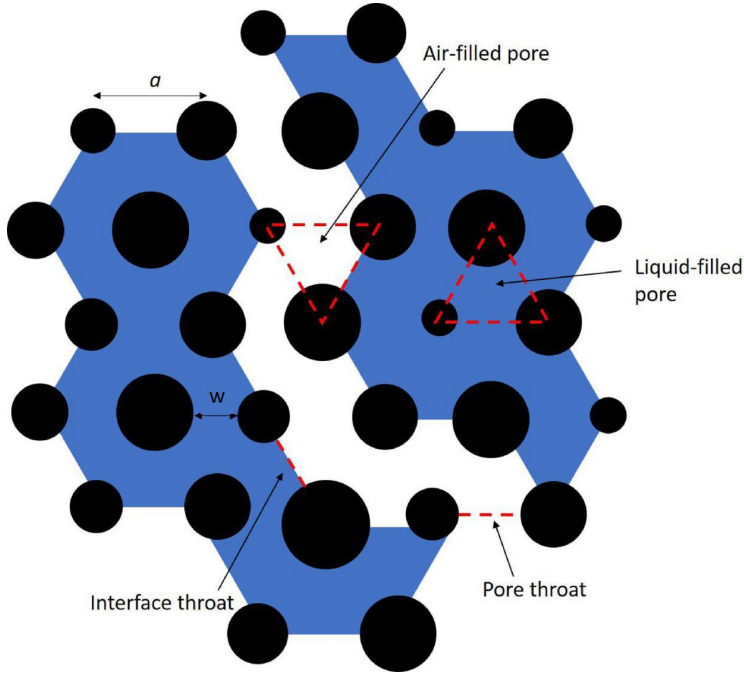
Figure 3.3: Sketch of pore geometry and pore-scale invasion. Particles, or in the case of the experiments pillars, are represented by filled black circles. Blue and white areas are used to represent the different fluid phases, here air displacing water. $a$ is the lattice spacing and $w$ represents the pore throat size.

$\bar{d} = 25$ $\mu$m and standard deviation $\sigma_d = 5$ $\mu$m, arranged in a spatially correlated pattern (Fig 3.2). The values of $d$ are limited to the range $[d(1 - \lambda), d(1 + \lambda)]$, where $\lambda = 0.8$; this constraint prohibits blocked throats due to particle overlaps, with the minimum throat width allowed being 10 microns. A pore is defined as the open volume between a set of three adjacent pillars, and a throat is defined as the constriction between two adjacent pillars, as sketched in Fig 3.3. The throat apertures thus have a mean size of $\overline{w} = 20$ $\mu$m, and the pore volumes are related to their surrounding pillar and throat sizes.

To introduce spatial correlations in the pillar sizes, a random rough surface $H(x, y)$ is generated (Fig 3.4) such that its Fourier transform is a Gaussian distribution of intensities, centered around zero, with random phases following methods documented elsewhere [47]. This is prepared by summing $10^4$ sinusoidal waves, whose amplitude, phase and orientation are selected from random uniform distributions, and whose wave numbers were drawn from a normal distribution. The width of this distribution, in the Fourier domain, is inversely proportional to the correlation length $\zeta$ of the surface (in units of the lattice length). The diameter of each pillar is now defined such that $d_i = \bar{d}(1 + H_i)$, where $H_i$ is the height of the correlated surface at a specific pillar coordinate $(x_i, y_i)$. Imposing spatial correlations in *particle* sizes also results in
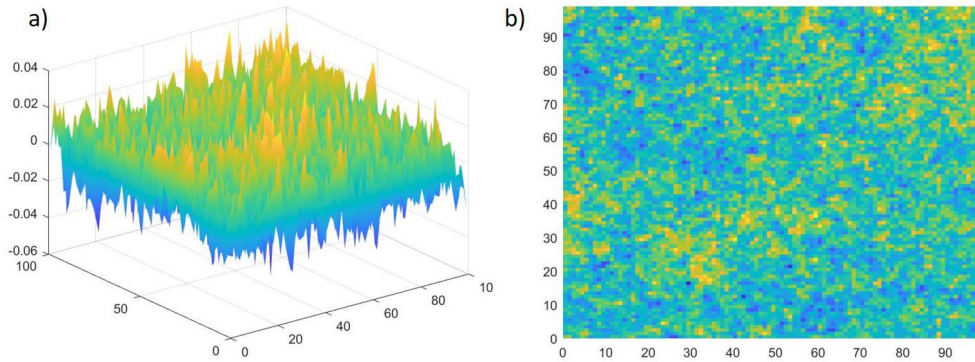
Figure 3.4: Rough surface generated to form correlated porous medium. a) Rough surface centered around 0. b) Top down view of rough surface. Height of each pillar is mapped from this rough surface, with 0 height being the mean pillar diameter.
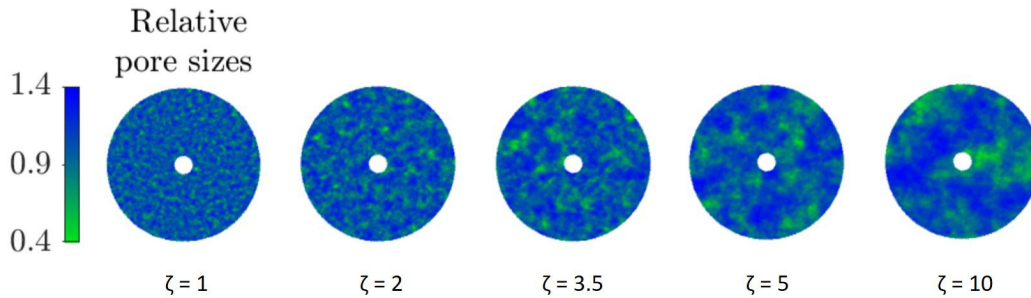


Figure 3.5: Colourmap of pore sizes in a porous system with increasing correlation length. Blue and green areas represent large and small pore sizes, respectively. With increasing correlation length there are larger areas of relatively wide pore throats through which the invading fluid will preferentially flow.

spatially-correlated *pore* sizes (Fig 3.5). The method for generating these spatially correlated geometries were supplied to us as a MatLab code.

### 3.1.2 Microfluidic Displacement Experiments

The experiments use a similar geometry to the numerical simulations. In the case of the experiments, the particles are 3-dimensional pillars made from poly(dimethylsiloxane) (PDMS). The lattice length in the experimental cells is $a = 130$ $\mu$m, the pillar mean diameter $\bar{d} = 80$ $\mu$m and the pillar size disorder is given by $\lambda = 0.5$, with spatial correlation lengths of $\zeta \in \{1, 2, 3.5, 5, 10\}$. These values allow for a minimum throat width of 10 $\mu$m, which ensures for the reliable fabrication of the prepared designs, while maintaining a high degree of size heterogeneity. There is an
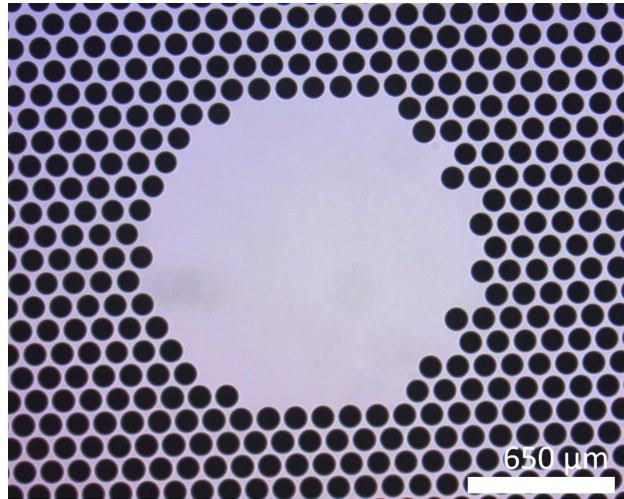
Figure 3.6: Microscope image of the photomask for the $\zeta = 5$ system. The image is centered around the inlet of the system and the circles show where the pillars will be produced in the lattice when manufactured and highlights the lattice structure.

uncertainty in pillar diameter of $\sim$1.0 $\mu$m (i.e. each pillar is within $\sim$1.25% of the designed size). This was measured by observing the pillars under a microscope and using ImageJ [48] to take measurements of the diameter of the pillar. To do this, multiple pillars from different chips were measured by drawing a circle around the circumference of each pillar and using the software to measure the diameter. To reduce the effect of human error, each measurement was performed 3 times independently. By knowing the calibration for a particular magnification, the uncertainty can be calculated from measurements of various pillars of different sizes.

Microfluidic micromodels are produced using soft lithography techniques, detailed in Chapter 2. A high-resolution chrome-quartz photomask (see Figure 3.6) and a negative photoresist (SU8 3025) is used to manufacture reusable templates. PDMS is poured over these master templates, degassed under vacuum, and cured for 1 h at 75°C. The PDMS covering a designed pattern is then cut and peeled off the master, and inlet/outlet holes punched. This patterned slab, and a PDMS-coated glass slide, are primed in an oxygen plasma and adhered to one another, forming a microfluidic chip of solid pillars separated by open channels with a thickness of h = 65 $\mu$m$\pm$3 $\mu$m. The thickness of these cells is measured on a Dektak stylus profilometer over various areas of the chip. An example design is shown in Fig. 3.1.

PTFE tubes (Adtech Polymer Engineering Ltd) are inserted into the inlet and outlets, and are sealed in place with a UV-curing adhesive (AA 3526, Loctite). A mixture of water and glycerol is chosen to be the defending fluid, as this allows for control of $Ca$. A Discovery Hybrid Rheometer is used to measure the viscosity of the mixture. By varying the ratio of glycerol to

| Glycerol % | Viscosity *(Pa.s)* | $Ca$ |
|:---:|:---:|:---:|
| 0 | 0.00100 | $1.93 \times 10^{-6}$ |
| 5 | 0.00107 | $2.07 \times 10^{-6}$ |
| 9 | 0.00127 | $2.45 \times 10^{-6}$ |
| 17 | 0.00165 | $3.18 \times 10^{-6}$ |
| 50 | 0.00664 | $1.28 \times 10^{-5}$ |
| 70 | 0.01918 | $3.70 \times 10^{-5}$ |
| 90 | 0.29763 | $5.74 \times 10^{-5}$ |

Table 3.1: Viscosity measurements for various amounts of glycerol in a water/glycerol mixture, and the resulting $Ca$ value given a constant withdrawal speed of 469.39 $\mu L/h$.

water, the viscosity of the mixture, and hence $Ca$ can be adjusted (see Table 3.1).

A water/glycerol mixture is then pumped through the central inlet to fill the cell. Any trapped air bubbles disappear after a few minutes due to the diffusion of air into the PDMS, leaving the cell saturated with liquid. The cell is then mounted horizontally under a digital camera (Nikon D5100) with the glass slide facing upwards. The entire apparatus is housed in a darkened box, with a low-angle LED strip surrounding the cell to highlight interfacial features. A syringe pump then withdraws liquid out of the cell through the outlet ports on its perimeter, allowing air to invade via the central inlet (see Fig. 3.1). Time-lapse images are taken every second until the liquid-air interface reaches breakthrough, invading the open area surrounding the porous medium. The syringe pump withdrawal rate is fixed at $Q = 1.30 \times 10^{-10}$ m$^3$/s, and Ca is varied by changing the composition (and hence viscosity) of the water/glycerol mixture to give $Ca$ values of $1.9 \times 10^{-6}$, $3.2 \times 10^{-6}$, $1.3 \times 10^{-5}$ and $3.7 \times 10^{-5}$, as summarised in Table 3.1. For calculating the values of $Ca$, the surface tension is assumed to be constant at $7.28 \times 10^{-2}$N/m for the range of viscosities used. Previous work [49] has shown that there will in fact be a small change of approximately 10% from 0%-70% glycerol, but this correction is considered negligible compared to other sources of uncertainty and is not considered in my $Ca$ values. Overall, 24 experiments were performed with various Ca and $\zeta$. The receding contact angle between the water/glycerol mixtures and PDMS was measured as 73° ± 8° using a drop shape analyzer (DSA-10, Krüss Scientific).

### 3.1.3 Pore-scale Model and Simulation Parameters

Described here is the numerical model, which was designed and implemented by Oshri Borgman, Ran Holtzman and Enrico Segre in collaboration with this work. The model is a hybridization

of two complementary pore-scale modeling approaches: pore-based and grain-based.

To obtain statistically-representative results from the simulations, averages and deviations for various metrics of the displacement patterns were computed from an ensemble of 10 realizations (namely, samples with the same statistical attributes but with different random seeds), for each $\zeta \in \{1, 2, 3.5, 5, 10\}$.

$Ca$ is varied in the simulations by varying the inlet pressure, rather than using an explicit constant flux condition. The average flow rate is calculated as $Q = V_{tot}/t_{tot}$, with $V_{tot}$ and $t_{tot}$ being the total displaced volume and time at breakthrough, respectively. This then provides a characteristic velocity of $v = Q/A_{out}$, where $A_{out}$ is the cross-sectional area of the cell's outer perimeter, which is open to flow (i.e. the sum of cross-sectional areas of the pore throats on the perimeter). Other parameters used in the simulations are the interfacial tension, $\sigma = 71.67 \times 10^{-3}$ $N/m$, and the viscosities of the invading and defending fluids, $\mu_i = 1.8 \times 10^{-5}$ Pa s and $\mu_d = 1 \times 10^{-3}$ Pa s, respectively. These values model the displacement of water by air. Finally, the contact angle in the simulations was set to $\theta = 73°$, to match the experimental conditions.

Pore-network models resolve pore pressures and interpore fluxes from pore topology and geometry [50], while grain-based models incorporate the different pore filling mechanisms that arise due to wettability effects, by linking the meniscus geometry to the local capillary pressure, grain size and contact angle [28]. An advantage of the numerical model implemented is its ability to capture the impact of flow dynamics (in particular, fluid viscosity effects and meniscus readjustments, as in [51]), along with the impact of partial wettability on pore-scale displacement mechanisms [46]. The key here is that the model used is efficient and can be run on a suitable laptop or computer, rather than the high end computers sometimes required for full CFD (computational fluid dynamics) models. The simulations are done in MATLAB®.

The basic status of each pore is determined by its fluid content, $\Phi$, where $\Phi = 0$ or 1 for a pore which is completely filled by the defending or invading fluid, respectively. The invasion front is defined by the interface separating fully invaded pores, where $\Phi = 1$, from accessible non-invaded ($\Phi = 0$) or partially invaded ($0 < \Phi < 1$) pores. A pore is considered accessible if it is topologically connected through the defending fluid to the outer boundary; as a result, the volume of the trapped clusters of the defending fluid is fixed, and they cannot be invaded or refilled in the simulations.

Along the invasion front the fluid-fluid interface is approximated by a sequence of menisci, shaped as circular arcs. Each arc intersects a pair of particles at the prescribed contact angle $\theta$ and has a curvature

$$\kappa = 1/R = \Delta p/\sigma, \tag{3.2}$$

where $R$ is the radius of curvature of the meniscus, and $\Delta p$ is the capillary pressure (the pressure jump across the meniscus), computed from the Young-Laplace law (Eq 1.1). The angle $\theta$ is measured through the defending fluid (i.e. $\theta < 90°$ for drainage), and represents an *effective* advancing contact angle, including any dynamic effects [52,53]. Knowledge of $R$ and $\theta$ allows for the ability to analytically resolve the geometry, and hence stability, of each meniscus.

To track the progression of the fluid invasion, at each time step, the following steps are involved: (1) locate the position of the invasion front from the filling status $\Phi$ and define the connected networks of pores within both fluids; (2) evaluate the pressure $p$ in each pore, and calculate the flow rate $q$ for each throat; (3) check for new meniscus instabilities and update the flow network accordingly; and (4) update the filling status of each invaded pore by $\Phi(t + \Delta t) = \Phi(t) + q^{inv}(t)\Delta t/V$, where $q^{inv}$ is the inflow of invading fluid, and $V$ is the pore volume.

An effectively constant injection rate is enforced by setting the hydraulic resistance of an 'inlet' region—a circle with a diameter of about 12 pores, surrounding the center of the cell— to be orders of magnitude larger than elsewhere. This ensures a practically constant pressure gradient that is maintained throughout the simulation, regardless of the front position, and a nearly constant flux of fluid into the sample. Simulations are terminated by the breakthrough of the invading fluid, i.e. once any pore on the outer boundary is invaded.

The time-step $\Delta t$ is chosen so that only a small fraction of a pore (not more than 30% of any invaded pore) may be filled by the invading fluid, in each step. When a pore invasion ends (i.e. when $\Phi = 1$) the interface configuration is updated by replacing any unstable menisci with new ones that touch the particles upstream from the newly invaded pore. The finite pore filling time in the model, while allowing pores which are partially-filled to re-empty if the direction of meniscus advancement is reversed, enables the model to capture dynamic (viscous) effects, overcoming a long-standing computational challenge [50,54].

## 3.2 Results

Microfluidic experiments were performed alongside simulations. These experiments were restricted to the low $Ca$ range due to equipment limitations. These limitations included the speed and size of the syringe pumps, the size of the syringes that fit the pumps, and difficulties with withdrawing highly viscous fluids from the system. In calculating the ensemble averages and standard deviation for each $\zeta$, averages were made over all the experiments in the range of the $Ca$ values tested. The motivation behind this is to increase the number of experimental values for each $\zeta$, improving the statistical significance of the analysis. This is justified by the small expected effect of $Ca$ on the invasion pattern in the quasi-static limit (low $Ca$) where viscous
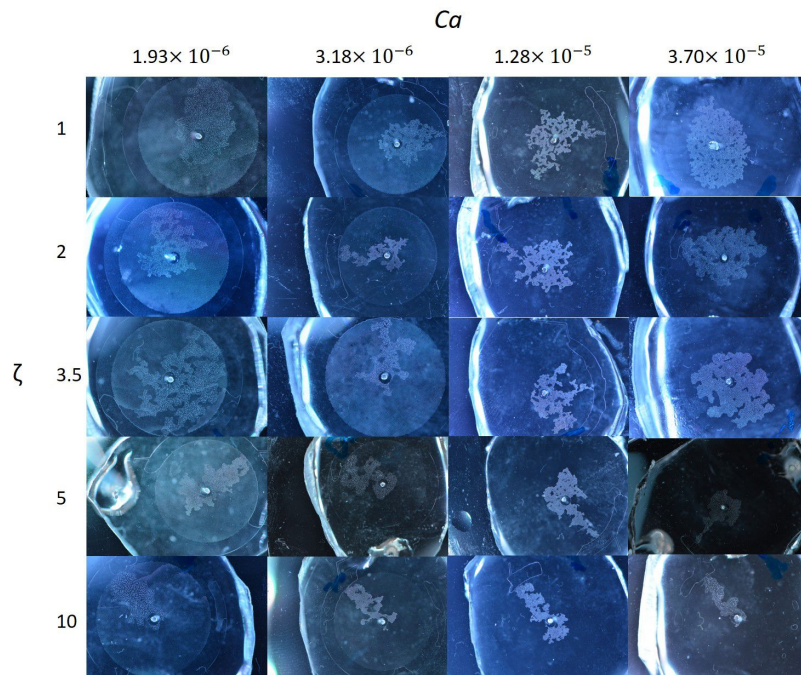
Figure 3.7: A selection of experimental invasion patterns at breakthrough for various capillary number values and each $\zeta$ value. The amount of displacement noticeably reduces as $\zeta$ increases but at this low Ca range, the effect of varying Ca is minimal.

effects are negligible [55]. Experimental data looking at the effect $\zeta$ has on the metrics, studied later in this chapter, with increasing $Ca$ confirms this assumption. However, this can lead to large error, particularly in the case of when $\zeta = 10$ where only 2 experiments were averaged over. Because of this, randomness in the patterns lead to significant uncertainty in the average values of the metrics investigated. While the current experimental setup was limited to low $Ca$, it is noted that the impact of correlation is most significant at these $Ca$ values, according to the simulations. The close agreement in this limit thus adds particular strength to these results.

### 3.2.1   Displacement Patterns

The microfluidic experiments produced at values of $Ca \leq 1.28 \times 10^{-5}$, are almost completely controlled by capillary forces rather than viscous forces and the invasion patterns (see Fig 3.7) produced are determined by the pore throat sizes throughout the system. However, due to limitations in the experiments, only the low $Ca$ range was able to be explored. The simulations performed by Oshri Borgman, Ran Holtzman and Enrico Segre, are able to go further and look at the effect $\zeta$ has in the higher $Ca$ range (see Fig. 3.8).

In the low $Ca$, low $\zeta$ domain, both the experiments and simulations show that the invasion
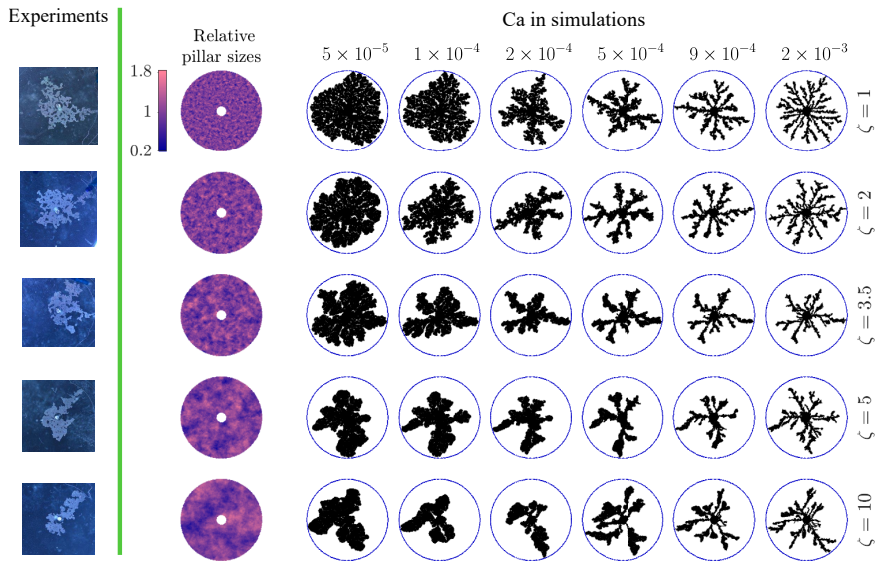
Figure 3.8: Displacement patterns at breakthrough in samples of various correlation lengths $\zeta$ and at different values of the capillary number Ca. Increasing $\zeta$ increases the size of regions or patches of similarly-sized pillars (e.g. a patch with larger openings and hence lower capillary thresholds and flow resistance), promoting preferential invasion through these regions, and resulting in patterns which follow more closely the underlying pore geometry. The left-most column shows images of experiments at Ca=$1.3 \times 10^{-5}$, where invading fluid (air) appears brighter. The remaining results are from simulations, including representative maps of the relative pillar sizes for each $\zeta$. Here, the invading and defending fluids appear in black and white, respectively, while the solid pillars are not shown. The perimeter of the porous medium is denoted by a blue circle. The same sample geometry, i.e. the set of *relative* pillar sizes, is used for all displacement patterns, and is shown in each row. Reproduced from [45].

patterns explore more of the system, as compared to longer correlation length samples, as the size of pillars are homogeneous across the porous medium and viscous effects are minimised. Keeping $Ca$ in the low regime and increasing $\zeta$ causes a change in the invasion patterns seen. Rather than the invading fluid exploring widely throughout the system, the invasion directs itself towards areas of larger pore throats, and thus the pattern loses its circular shape as it finds more preferential pathways. The simulations show that the impact of $\zeta$ is relatively limited at high Ca, where viscous fingering patterns (long thin fingers) inevitably emerge, as pressure screening inhibits invasion behind the most advanced edge of the displacement front [18].

Nevertheless, at higher $Ca$, increasing $\zeta$ reduces the number of invading fluid fingers, and lowers the displaced volume at breakthrough. In many ways these invasion patterns resemble a skeleton or backbone of the patterns produced for lower $Ca$ invasions at the same $\zeta$ value, showing

a. $\zeta = 10$     b. $Ca = 1.92 \times 10^{-5}$     c. $Ca = 5 \times 10^{-5}$
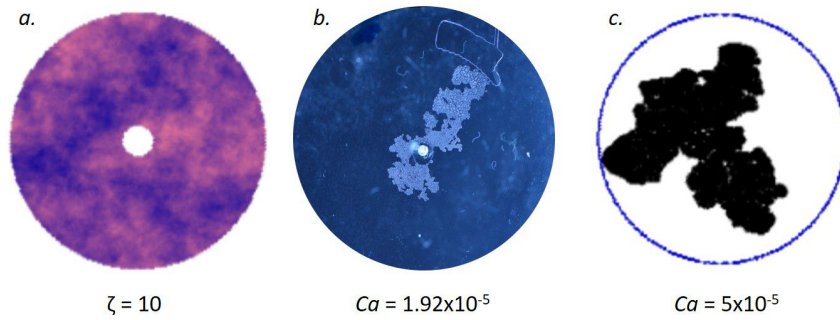
Figure 3.9: Sample of patterns taken from Figure 3.8 at $\zeta = 10$. a) Shows the underlying pore geometry with pink and blue areas representing areas of large and small pillars, respectively. b) Experimental invasion pattern in same geometry. The invading fluid follows path of small pillars (blue area), with a limited, highly asymmetric invasion area. c) Simulation in same geometry at slightly higher $Ca$. The simulation explores more of system than the experiments, but the pattern isn't circular and doesn't explore fully the system.

that regions of large or small pores remain the preferred locations for guiding or inhibiting the invading fingers, respectively (see Fig 3.9). Thus, the number of fingers is limited compared to the less correlated samples, in which fingers propagate equally and freely in all directions.

### 3.2.2 Interfacial Features

Of interest in the displacement patterns is the interface between the two fluids and the shape and volume of the invading fluid's fingers [18]. The interfacial area (defined as the number of pores at the interface) between the fluids is related to the pressure-saturation relationship [56,57], and has a direct effect on the rates of fluid mixing and chemical reactions [58]. Here, it is characterised by $A^*_{\text{inter}}$, which is the ratio of interfacial pores to invaded pores at breakthrough, which is then normalized by the invaded area.

As shown in Fig 3.11 and Fig 3.12a by the numerics, this interfacial area decreases as the correlation length is increased, regardless of flow rate. At low flow rates, there exists a notable transition from capillary fingering at low $\zeta$ to smoother displacement patterns at high $\zeta$. In contrast, when $Ca$ is increased, there is an increase in $A^*_{\text{inter}}$ due to the transition into the viscosity-dominated regime of the displacement patterns [31,59]. The experiments come close to the values produced by the numerics, as shown in Fig 3.11, and also indicate there is a negligible effect of $\zeta$ on the invasion pattern for low $Ca$. Here, the experiments average over all $Ca$ values for each $\zeta$. This then provides suitable validation of the numerics and should provide confidence in results only produced by the simulations.
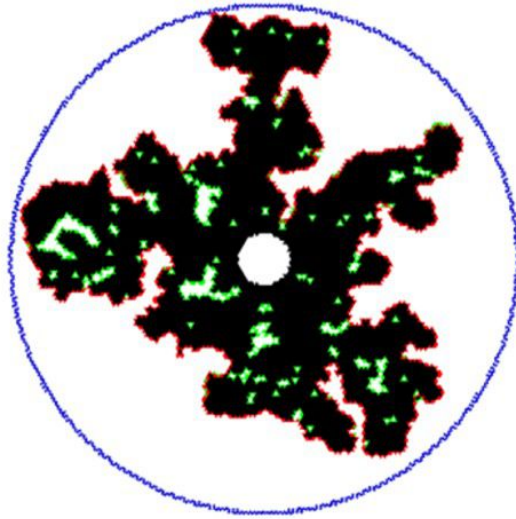
Figure 3.10: Example of $A^*_{\mathrm{inter}}$. The interfacial area is made up of the front area pores (red) and the trapped pores (green). The value of $A^*_{\mathrm{inter}}$ equals this interfacial area normalized by the invaded area (black).

Another characteristic highlighting the transition from capillary to viscosity-controlled displacement is the increase in the relative *front* area, $A^*_{\mathrm{front}}$, with $Ca$; here, $A^*_{\mathrm{front}}$ is defined as the ratio of the total front area (excluding trapped clusters, cf. Fig. 3.12c) to the invaded volume, at breakthrough. This occurs across all $\zeta$ values, as the increase in pore-size correlation brings the competing contributions of two phenomena—reduction in the invaded volume, and in the interface roughness.

Finally, the width of the invading fingers investigated here is defined as the mean distance from any interfacial point to the nearest point on the skeleton of the pattern. As shown in Fig. 3.12b, it is found that the mean finger width, $W$, is generally higher for larger $\zeta$. This correlates with the increasing sizes of the regions with large pores, through which the invasion proceeds at low Ca, when capillarity is dominant. At sufficiently high Ca, viscous screening leads to the emergence of thin fingers, and minimizes the impact of the underlying porous microstructure (i.e. $\zeta$). In the simulations, for large $Ca$, $W$ tends to a value similar to that found for invasion into uncorrelated porous media [31], further exemplifying the reduced effect of correlations at higher flow rates.

### 3.2.3 Preferential Displacement and Invasion Selectivity

The invasion is considered to be "selective" if it samples only a narrow range of pore sizes from the entire size distribution available to it. Similarly, the term "preferential" is used to describe a

Figure 3.11: Results from both experiments (blue) and simulations (red) for $A^*_{\text{inter}}$. Lines show average value over multiple runs with the clouds representing the error in those averages. Experimental results closely match those produced by the simulations and both show the negligible effect $\zeta$ has on $A^*_{\text{inter}}$ at low $Ca$ ($Ca \leq 1.28 \times 10^{-5}$).

displacement advancing through distinct pathways or channels, rather than in a uniform radial front (i.e. certain routes are *preferred*). Selective invasion can result in preferential patterns, which is the case here for larger $\zeta$: by selectively invading through the connected regions of larger pores, the invading fluid propagates in more preferential patterns.

The difference between a preferential invading pattern and one which has a uniform radial front can be quantified by investigating the pattern's acylindricity, $\beta^*$, which is calculated from the second moment of a best-fit ellipse to the invaded area [60]. Briefly, the Gyration Tensor $T$ is calculated from the location of all invaded pores.

$$T = \frac{1}{N} \begin{pmatrix} \sum_i x_i & \sum_i x_i y_i \\ \sum_i y_i x_i & \sum_i y_i \end{pmatrix} \tag{3.3}$$

where $x$ and $y$ are the spatial coordinates and $i$ runs over all $N$ invaded pores. The acylindricity $\beta^*$ is calculated from the eigenvalues, $\lambda_k$, of this tensor.

$$\beta^* = \lambda_y^2 - \lambda_x^2 \tag{3.4}$$

For a perfectly circular invasion pattern, $\beta^* = 0$, whereas for a single needle-like growth along one direction, $\beta^* = 1/3$. Qualitatively, it can be seen that $\zeta$ has a significant effect on the shape

(a)

(b)

(c)
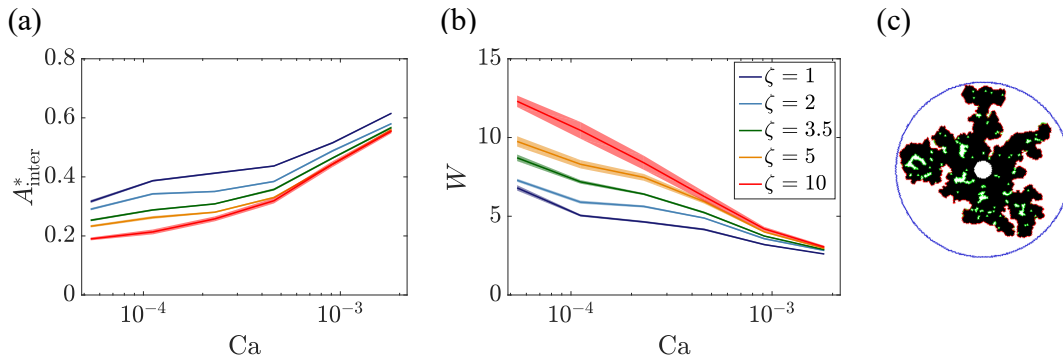


Figure 3.12: In numerical simulations, increasing the correlation length of the particle sizes, $\zeta$, reduces the relative interfacial area, $A^*_{\text{inter}}$, and increases the invading finger width, $W$. a) $A^*_{\text{inter}}$ is lower for larger $\zeta$, due to the increasing smoothness of the displacement patterns, and increases with the capillary number Ca, as viscous forces become dominant. b) The finger width increases with $\zeta$, and decreases with Ca. For each $\zeta$ is plotted the ensemble average (lines) and the standard error (shading) of 10 independent realizations. c) The front area (marked in red) is the leading part of the interface only, excluding trapped clusters (green) and the interfacial area is the sum of the front area and the perimeter of the trapped clusters. Here the invading fluid is shown in black, and the cell perimeter in blue.

of the invasion patterns, as the invading front finds a preferential paths in one or a few directions (see Fig 3.7). Further, the experiments show that quantitatively, there is an increase in the measured acylindricity from low $\zeta$, but the effect is limited when transitioning from intermediate to higher $\zeta$ (see Fig 3.13). The patterns are therefore already finding the preferential pathways around the intermediate values for $\zeta$ and further increasing $\zeta$ has no significant effect. Similar to the experiments, the simulations show that the patterns become less symmetric with increasing $\zeta$. The highest values of $\beta^*$ are obtained for low-to-intermediate Ca and high $\zeta$, when capillary forces dominate pore invasion, and the underlying heterogeneity has the greatest impact (Fig. 3.14d).

The simulations look into more detail of the effect that $\zeta$ and $Ca$ have on preferential displacements. As shown in Fig. 3.14, the mean width of the invaded throats (normalized by the mean throat width, i.e. $\overline{w_{\text{inv}}}/\overline{w}$) increases with $\zeta$ for all flow rates, indicating that the correlations result in a more selective invasion. While the selectivity does also increase with Ca, it saturates for faster flows, where viscous forces dominate, and may even decrease at the highest Ca studied. As discussed in Section 3.2.1, viscous fingers at high flow rates will still grow more readily into correlated regions of larger throats, and be inhibited by tighter pores. Once any finger falls behind the main front, pressure screening will further limit its advance. Thus, although finger
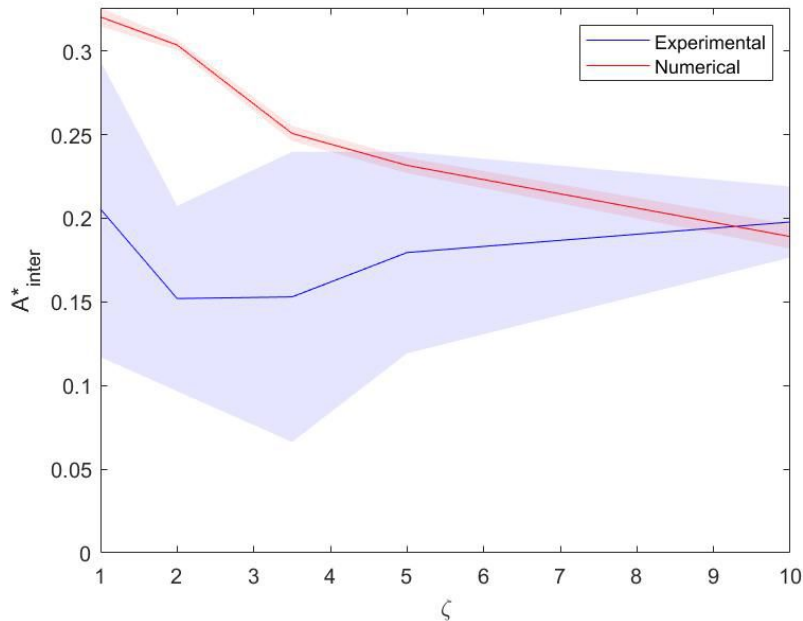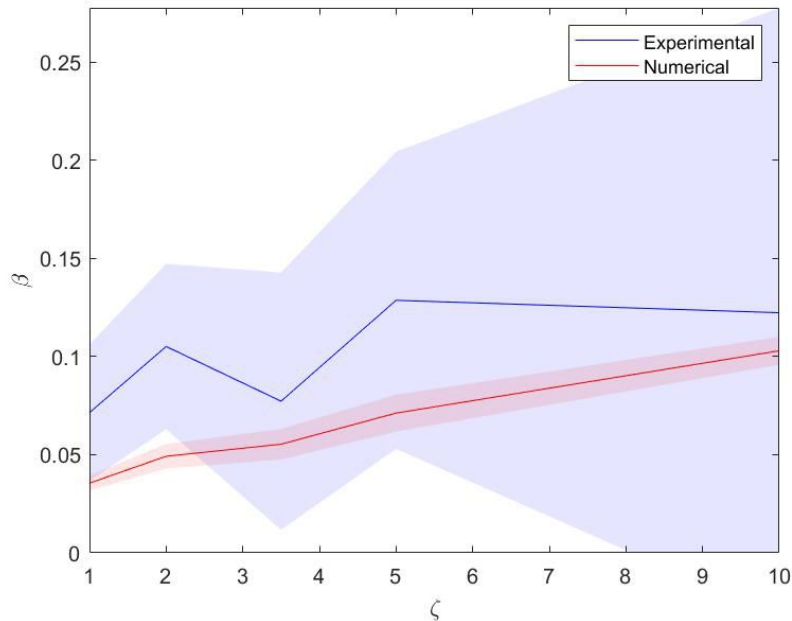
Figure 3.13: Results from both experiments (blue) and simulations (red) for acylindricity. Lines show average value over multiple runs with the clouds representing the standard error in those averages. Experimental results show a small but significant effect on $\beta$ at low to intermediate $\zeta$, with negligible effect at intermediate-high $\zeta$.

propagation depends more on the viscous resistance to flow—a nonlocal feature, as opposed to the local capillary resistance—an interplay between these two resistance terms at the leading edge of the invasion front promotes selective invasion of the largest pores. Increasing $\zeta$ also promotes more preferential fluid displacement into the connected clusters of larger pores. This is characterized here with a series of metrics that describe whether the invasion front is smooth and symmetric (less preferential), or rough and asymmetric (more preferential). For example, the average radius of the displacement front at breakthrough decreases with increasing $\zeta$, as shown in Fig. 3.14b. High values of $R_f$ (the mean front radius, scaled by the system size — see Fig. 3.14e,f) mean that the invading fluid front has approached the cell boundary in all directions in a more even manner. Hence, a decrease in $R_f$ shows that most of the displacement occurred through a smaller part of the cell, e.g. through fewer fingers. Another indication of the more preferential invasion at higher $\zeta$ is the increase in the front width $\sigma_f$—the standard deviation of the front location around $R_f$ [61]—as presented in Fig. 3.14c. The gradual transition from capillary fingering to viscous fingering, between intermediate and high Ca, results in an increase of $\sigma_f$ (i.e. a wider front, which is more pronounced for smaller $\zeta$) and a decrease of $R_f$. In brief, shown here is that increasing $\zeta$ results in more selective fluid invasion, which leads to preferential
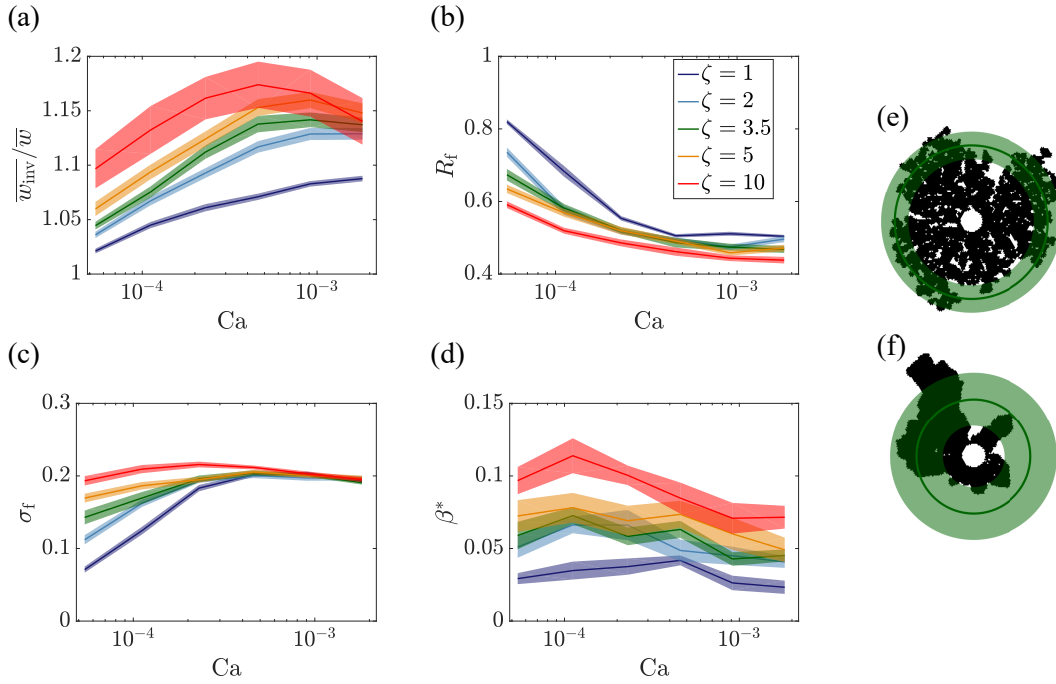
Figure 3.14: Results taken from the simulations. Spatial correlation leads to more selective, preferential and asymmetric displacement. (a) At larger $\zeta$ the invasion is able to *select* for a higher mean invaded throat width $\overline{w_{\text{inv}}}/\overline{w}$. (b) This allows for a more *preferential* route of the displacement front to breakthrough, and the mean radius of the displacement front, $R_{\text{f}}$, decreases with both increasing correlation length $\zeta$ and capillary number Ca. (c) Similarly, the displacement front width, given by the standard deviation of the front position, $\sigma_{\text{f}}$, increases with both $\zeta$ and Ca. (d) Additionally, displacement patterns become less *symmetric* with increasing $\zeta$, as quantified here by the rescaled acylindricity $\beta^*$, which is zero for a circular pattern. For each $\zeta$ is a plot of the ensemble average (lines) and standard error (shading) of 10 realizations. Example displacement patterns for $\zeta=1$ (e) and $\zeta = 10$ (f), at Ca $= 1 \times 10^{-4}$, illustrate the definitions of the mean front radius $R_{\text{f}}$ (dark green circle) and width $\sigma_{\text{f}}$ (green shading). For $\zeta=1$ the displacement front is further from the injection point on average (large $R_{\text{f}}$), while the front positions are more narrowly spread out (small $\sigma_{\text{f}}$), than for $\zeta=10$. Reproduced from [45].

displacement patterns; these are characterized by a lower front radius, higher front width, and lower symmetry.

### 3.2.4   Displacement Efficiency

The sweep efficiency of an invasion determines how well a defending fluid can be displaced or withdrawn and is of major importance to applications such as oil production and groundwater
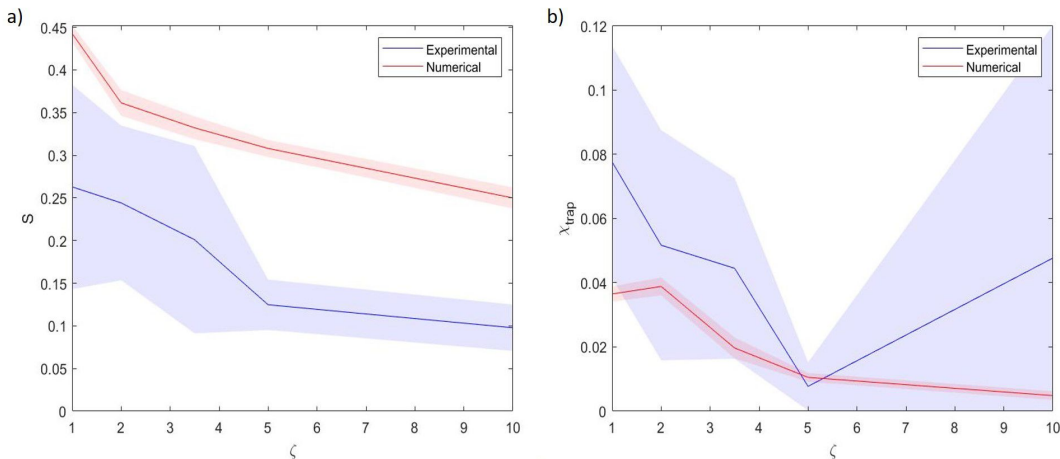
Figure 3.15: Results from both experiments (blue) and simulations (red) for a) saturation b) trapping fraction. Lines show the average values over multiple runs with the clouds representing the standard error in those averages. a) Both experiments and simulations shown same downward trend in $S$ with increasing $\zeta$. b) Experiments match the downward trend of the trapped fluid fraction shown by simulations, up to at least $\zeta = 5$.

remediation. [62, 63]. A typical measure of sweep efficiency is the invading fluid saturation at breakthrough, $S$. Experiments show that at low Ca, with increasing $\zeta$ the amount of invaded area is reduced as the fluid is forced into fewer, more preferential pathways, and thus reduces $S$ (Fig. 3.15). The simulations are then able to expand on this further and investigate the effect that increasing Ca has on the significance of $\zeta$ (Fig 3.16a). Due to the narrow, extended nature of viscous fingering, their emergence at high $Ca$ also significantly reduces $S$, and more sharply at lower $\zeta$.

The displacement efficiency is related to (and affected by) trapping— the amount of isolated clusters of defending fluid that are immobile and disconnected from one another. The trapped fraction $\chi_{\text{trap}}$ depends in a complex manner on both the sample geometry and the flow rate, leading to a non-monotonic dependence on $\zeta$ in the experiments. This is also shown to be the case in the simulations, which are non-monotonic for $Ca$ at low $\zeta$ values (see Fig 3.15). Here, $\chi_{\text{trap}}$ is defined as the volumetric ratio of the trapped defending fluid to the total injected fluid, at breakthrough. The initial downtrend in $\chi_{\text{trap}}$ with $\zeta$ stems from the transition from a homogeneous system to a heterogeneous one. At low $\zeta$ there exist many small, uninvaded pores containing trapped fluid as there is no preferential pathway for the invading fluid to take. Then as $\zeta$ increases, and larger clusters of more open pore throats are grouped together, the fluid takes a more direct approach through the system before breaking out, leaving fewer and
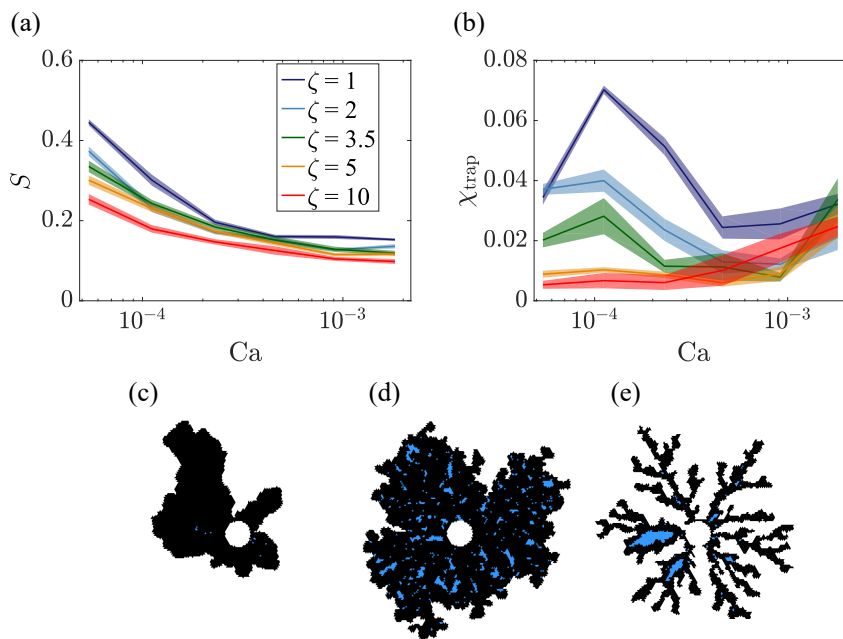
Figure 3.16: Results taken from the simulations. Effects of correlated heterogeneity on fluid displacement efficiency and trapping. a) The sweep efficiency—i.e. the breakthrough saturation, $S$, of the invading phase—is reduced for longer-range correlations, due to the preferential invasion of larger pores. The effect of $\zeta$ is less apparent at high $Ca$, where viscous fingering is responsible for low efficiency. b) The fraction of trapped defending liquid, $\chi_{\text{trap}}$, is higher for shorter-range correlations, at most $Ca$ values. Increasing $\zeta$ suppresses trapping under capillary-controlled invasion, as demonstrated by comparing displacement patterns for $\zeta=10$, $Ca = 1 \times 10^{-4}$ (c) and $\zeta=1$, $Ca = 1 \times 10^{-4}$ (d). The increase in trapped liquid (blue regions) with $Ca$ at viscous-dominated regime (high $Ca$) is related to trapping *between* viscous-controlled invading fingers (see panel (e), for $\zeta=1$, $Ca = 2 \times 10^{-3}$). For each $\zeta$ the ensemble average (lines) and standard error (shading) of 10 realizations is plotted. Reproduced from [45].

fewer areas of trapped fluid. The sudden increase in $\chi_{\text{trap}}$ at higher $\zeta$ is likely due to the large areas of small pore throats for which the fluid does not invade. The invading fluid will preferentially invade the larger throat areas and wrap around the smaller throat areas, leaving behind large clusters of defending fluid. The trend in $\chi_{\text{trap}}$ with Ca (shown by the simulations in Fig 3.16b) is due to the transition between three distinct trapping modes [31]: (i) For *low* Ca, the invading fluid efficiently fills the pore space, and trapping is limited (see case in Fig. 3.16c); (ii) at *intermediate* Ca, capillary fingering patterns emerge, which trap multiple small islands of defending fluid ("capillary trapping", Fig. 3.16d); (iii) at *high* Ca, viscous fingering becomes more dominant and trapping occurs in fewer, but larger, volumes in between distinct fingers (here

called "viscous trapping", Fig. 3.16e). In the transition between capillary and viscous fingering (between intermediate and high Ca), trapping first decreases as capillary trapping becomes less efficient, and then rises again due to viscous trapping. For the shorter-range correlations, the highest flow rates are characterized by more fluid fingers, compared to intermediate flow rates (see Fig 3.8). In these cases the higher number of fingers leads to more coalescence, and hence more trapping of the defending fluid, as compared to the simulations with long-range correlations.

It is noted that for the sample geometries and flow rates considered here, trapping is not the primary control on displacement efficiency. This is mostly evident at high $\zeta$ and low Ca, where the displacement occurs through few distinct regions; while these regions are essentially contiguous, with a few small trapped islands, the preferential nature of the invasion pattern only allows it to explore a smaller section of the porous medium (compared to low $\zeta$) with a much lower overall efficiency.

### 3.2.5   Comparing Experiments and Simulations

As was shown in Fig. 3.8, the impact of the correlation length $\zeta$ on the resulting displacement patterns is similar in both the experiments and simulations, at least for the low $Ca$ that are accessible experimentally. As shown in Figures 3.11, 3.13 and 3.15, most metrics show similar magnitudes and trends in the experiments and simulations, with two minor exceptions. First, while there were similar values of $A^*_{\text{inter}}$ for experiments and simulations for $\zeta = 10$, the decrease in $A^*_{\text{inter}}$ with $\zeta$ is apparent in the simulations alone (Fig. 3.11). The second small discrepancy is the consistently lower saturation at breakthrough, $S$, in the experiments vs. the simulations (Fig. 3.15a).

As was previously mentioned, the experimental results were averaged over a range of relatively low $Ca$ values (specifically $Ca = 1.9 \times 10^{-6}$, $3.2 \times 10^{-6}$, $1.3 \times 10^{-5}$ and $3.7 \times 10^{-5}$) as higher values were unobtainable with the small scale of the experimental setup. The results of each measured metric against $Ca$ are shown in Fig 3.17. What is clear from these results is that varying $Ca$ in this range shows no significant effect on any of the metrics measured. In fact, the effect $\zeta$ has on these metrics is only observable when averaged over the whole range of $Ca$ values, and not when compared for individual $Ca$ values. This is to be expected in this range of $Ca$, which is well into the quasi-static limit. The point of these experiments was to first test the limits of the experimental setup by varying the ratio of water/glycerol mixture, and thus viscosity, and the speed of the syringe pump being used. The experiments were also a validation that there was no significant effect of the capillary number on invasion patterns in this low range.
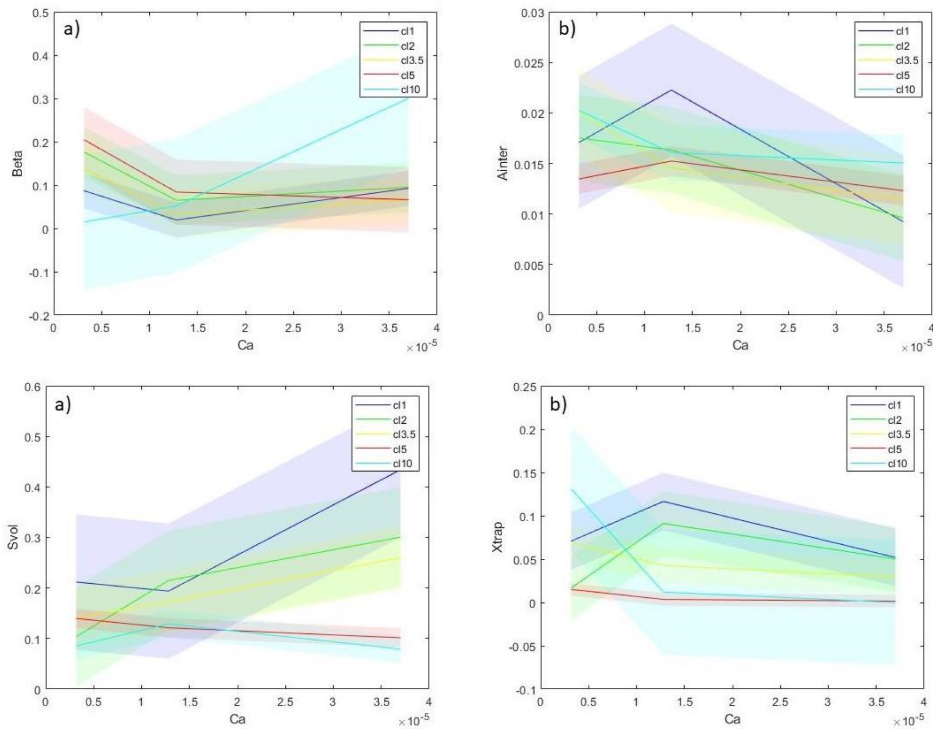
Figure 3.17: Experimental data for invasion metrics against $Ca$. Each solid line represents the average value taken over multiple experiments with the corresponding cloud representing the standard error in those averages. Results show the general lack of effect $Ca$ has on any aspect of the invasion pattern at this low range of $Ca$.

## 3.3 Discussion

### 3.3.1 Implications for Viscous Flow and Solute Transport

The impact of spatial correlation on fluid displacement patterns, exposed in this study, implies that correlations can be expected to strongly influence additional aspects of fluid invasion such as flow rates, solute transport and reaction rates. The selective invasion of larger pores is characteristic of better correlated porous media (Fig. 3.14), and the resulting preferential displacement patterns increase the relative permeability of the invading phase (at a given saturation), as compared with uncorrelated media [64]. This effect is due to the control exerted on the relative permeability by the fluids' spatial distribution and connectivity, changing, for instance, the constitutive relationship between relative permeability and saturation or capillary pressure [64, 65]. This is in line with previous observations of the effect of pore-size disorder (in uncorrelated samples) on fluid displacement patterns [31] and its impact on relative permeability [66].

Since solute transport is largely controlled by fluid flow, correlations in the microstructure can

also lead to preferential solute transport pathways and localized reaction hotspots. A similar link between flow focusing and transport has been recently shown for uncorrelated heterogeneity [67], and it is to be expected that correlations would intensify this impact. Specifically, the findings of the suppressive effect of pore-size correlations on the creation of fluid-fluid interfacial area (Fig. 3.12) suggest a consequent effect on solute concentration gradients, solute mixing, and reaction rates [58, 68] between the solutes carried by the invading fluid and those resident in the defending fluid. For instance, in light of the positive effect of viscous fingering on fluid mixing and reaction rates [69–71], it is expected that increasing correlations—by delaying the transition to viscous fingering—would reduce the mixing rate at a given flow rate. Transport heterogeneity, associated with differences in flow velocities between regions with high and low conductivity, was also shown to influence solute dispersion [72, 73], again suggesting a link between pore-size correlations—and their effect on fluid transport—and solute transport.

Finally, the relationship between flow intermittency and pressure fluctuations during immiscible displacement was recently demonstrated in drainage experiments in uncorrelated porous media [74], and in drying experiments and simulations in correlated porous media [75]. The latter study also shows how increasing the correlation length leads to larger avalanches, as larger patches of similarly-sized pores become accessible with an increase in capillary pressure; this is consistent with the interpretation of increasing invasion selectivity presented here.

### 3.3.2 Environmental Relevance of Structural Heterogeneity

The effect of spatial correlations on fluid displacement, forcing it to become more preferential, has implications for a variety of environmental processes at various length scales. For example, it has been shown that structural heterogeneity can impact water infiltration in soils and the emergence of preferential flow [76], the development of unsaturated zones at the river-aquifer interface [77], and the distribution of saline and fresh water within the continental shelf [78]. The occurrence of structural heterogeneity, in the form of high permeability zones within aquitards, can also compromise their ability to act as barriers for water and contaminant migration [79]. In addition, the contrast in permeability between different geological layers may control the mechanisms for attenuation of $CO_2$, when considering leakage from an underground reservoir used for carbon capture and storage [80–82]. These studies show the importance of considering the structural heterogeneity of porous materials, due to their impact on flow rates and fluid phase distribution. While upscaling pore-scale results to core or field scale remains a significant challenge [83], pore-scale studies such as the one presented here serve as important building blocks for simulations of environmental phenomena at regional scales (e.g. [84]).

## 3.4   Summary

Presented here is a systematic investigation of the impact of correlated heterogeneity on fluid displacement patterns, and its interplay with flow rates, in partially-wettable porous media, by combining high-resolution microfluidic experiments with pore-network simulations. It is found that at low-to-intermediate flow rates (i.e. low or moderate $Ca$, where capillarity dominates over pore invasion) increasing the correlation length results in a lower sweep efficiency, reduced trapping of the defending fluid and lower interfacial area, with displacement patterns that are more preferential, and which follow more closely the underlying pore geometry. These patterns are further characterized by wider invading fingers and lower symmetry. The simulations extend the experimental results into the higher $Ca$ regime, when viscosity dominates, and where it is found that the impact of correlation becomes relatively limited, although the pattern symmetry and trapped fraction are still lower than for uncorrelated porous media.

These results highlight the importance of considering not only the disorder in the system but also the spatial distribution of pore sizes and their connectivity. Applications where these effects could be present include water distribution in the subsurface [76, 77], transport, mixing and reaction of contaminants and nutrients [58, 73, 85], and fluid displacement patterns in engineered porous materials [53, 86]. These are merely a few examples of applications in which structural heterogeneity plays a key role in fluid and solute transport across scales, emphasizing the need for models that properly incorporate such pore-scale heterogeneity.

# Chapter 4

# Effect of Disorder on Dispersive Transport in Porous Media

Transport processes in porous media via fluid flow is a common and integral part of both the natural world [35, 87] and industrial processes [34, 36, 88]. There are various forms of transport in fluid flow that can be considered, those such as of mass, heat and momentum. For instance, in reactors there are chemical reactions within a fluid which can generate heat, which is then transported across a system as fluid flows [89]. Alternatively, mass can be transported within a fluid in biological systems such as when nutrients are passed around a microorganism or a plant, [90]. It is clear then, that an understanding of transport phenomena in fluids is essential to not only grasp natural processes, but to help develop industrial mechanisms that support the modern world in which we live. This chapter considers the motion of a dissolved phase, or solute, moving with a fluid in a porous medium. This work has been drafted for publication [91], with my contribution forming the experimental basis of this paper.

One way that dissolved mass can be transported in a fluid is via diffusion. Diffusion is the process by which mass is transported through a fluid by the random motion of molecules. Fick's laws are one of the underlying models of diffusive transport [92]. They state that mass will flow from areas of high concentration to areas of low concentration. The rate at which mass flows via this method is then proportional to a diffusion constant and the concentration gradient. This can be seen in the equation for Fick's first law of diffusion:

$$\boldsymbol{J}_{\text{diff}} = -D_M \boldsymbol{\nabla} c \tag{4.1}$$

where $\boldsymbol{J}_{\text{diff}}$ is the diffusion flux vector, $D_M$ is the molecular diffusion coefficient and $c$ is the concentration of the dissolved mass. From this equation, it can be seen that the greater the difference between areas of high and low concentration, the faster the flux will be. Likewise, the greater the diffusion coefficient, which varies depending on the viscosity and temperature of the liquid and the size of the diffusing particles, the faster the flow via diffusion. This form of diffusion will always be present, including for fluids in porous media, and for fluids that are not otherwise moving.

Fick's first law, along with the continuity equation for the dissolved mass, can be in turn used to derive Fick's second law:

$$\frac{\partial c}{\partial t} = -\boldsymbol{\nabla} \cdot \boldsymbol{J} = D_M \boldsymbol{\nabla}^2 c \tag{4.2}$$

Dispersion is similar to diffusion in that it is a means through which mass moves from areas of high concentration to areas of lower concentration. It can be written in the same form as Fick's first law [93]:

$$\boldsymbol{J}_{\text{disp}} = -E \boldsymbol{\nabla} c \tag{4.3}$$

where here $E$ represents the dispersion coefficient. The main difference between dispersion and diffusion is that dispersion is due to macroscopic deviations in the flow pattern, rather than Brownian motion, as in the case of diffusion.

When there is an overall flow through the system, there is also transport of the solute carried by the flow, in other words advection, represented by the flux:

$$\boldsymbol{J}_{\text{adv}} = \boldsymbol{v} c \tag{4.4}$$

where $\boldsymbol{v}$ is the velocity vector. By inspecting flow through a simple tube or pipe, it can be shown how dispersion occurs due to the shear effects acting on the fluid by the tube walls. For non-flowing fluid inside a tube, particles will diffuse around the tube simply due to molecular diffusion as described in Eq 4.1. For this, all particles everywhere will behave in the same manner. However, when fluid is flowing, shear effects will cause the fluid closest to the tube wall to flow slower than the fluid in the center of the tube. The particles will now randomly sample different velocities as they randomly move up and down the width of the tube, which will cause a sharp step in the concentration of particles to be smeared out across the pipe, and on the larger scale, across the system itself. This effect is known as Taylor dispersion [94], as sketched in Fig 4.1.

For a system where both advection and diffusion occur, the total flux is the summation of all three effects, diffusion, dispersion and advection:

$$\boldsymbol{J} = \boldsymbol{J}_{\text{diff}} + \boldsymbol{J}_{\text{adv}} + \boldsymbol{J}_{\text{disp}} = -D_{\text{M}} \boldsymbol{\nabla} c + \boldsymbol{v} c - E \boldsymbol{\nabla} c \tag{4.5}$$

and then introducing the continuity equation gives the advection-diffusion coefficient:

$$\frac{\partial c}{\partial t} + \boldsymbol{\nabla} \cdot (-D_{\text{M}} \boldsymbol{\nabla} c + \boldsymbol{v} c - E \boldsymbol{\nabla} c) = 0 \tag{4.6}$$

where there are no other sources of concentration, $c$, other than at the boundaries. Since they have the same functional form, we can write the diffusive and dispersive contributions using an effective diffusion constant, a result of both Taylor dispersion and molecular diffusion:

$$\frac{\partial c}{\partial t} = \boldsymbol{\nabla} \cdot (D_{\text{eff}} \boldsymbol{\nabla} c - \boldsymbol{v} c) \tag{4.7}$$
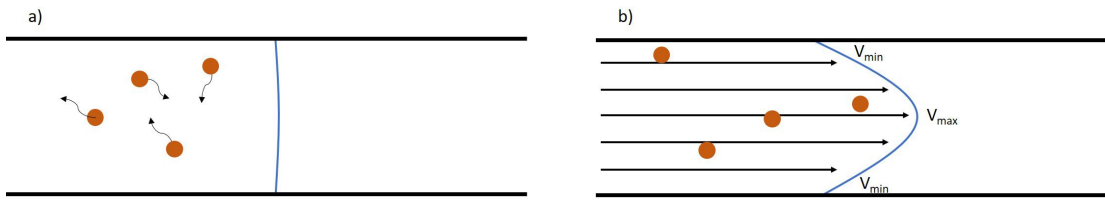
Figure 4.1: Effect of flow in a tube on particle transport. (a) If there is no flow in the tube, then particles will drift via molecular diffusion and a sharp concentration front evenly spreads across the length of the tube, parallel to the tube walls. (b) However, if there is a flow in the tube, then drag on the flowing fluid leads to faster flow in the center of the tube compared to near the edge of the tube. For particle transport, this causes non-uniform spread of concentration, as particles near the center of the tube are moved across the tube at a faster rate than particles close to the tube wall.

$$D_{\text{eff}} = D_M(1 + \frac{Pe^2}{48}) \tag{4.8}$$

From Eq 4.8, it can be seen that the effective diffusion constant, $D_{\text{eff}}$, is greater than the effect of molecular diffusion alone and is more and more dominant depending on the value of the Péclet number, $Pe$ [95]. In this case, the dispersion coefficient, $E$, can be written in terms of the Péclet number [96]. As previously explained in Chapter 1, the Péclet number is a dimensionless number and is the ratio of the advective transport rate to diffusive transport rate. It can be written in the form:

$$Pe = \frac{\text{advective transport}}{\text{diffusive transport}} = \frac{Lu}{D_M} \tag{4.9}$$

where $L$ is a characteristic length scale, $u$ is the flow velocity and $D_M$ is the molecular diffusion constant. The characteristic length scale in this case is the tube radius. For $Pe \gg 1$, dispersion can be orders of magnitude greater than expected by molecular diffusion, and is the dominant mode of spreading out concentration fields.

For a porous medium, the pore throats that connect pores are analogous to the tubes in the above discussion, where the pore throat width is comparable to the diameter of the tube, in which advection and diffusion occur. The porous medium itself is then a network of these tubes and will enhance the effect of Taylor dispersion on the transport of mass through the system.

For any macroscopic fluid invasion pattern, it has been shown, both in this thesis and other works [26, 46], that the make-up of the porous medium dictates the flow of the fluid. This may be the porosity of the medium, the viscosity of the fluid or the rate at which the fluid enters
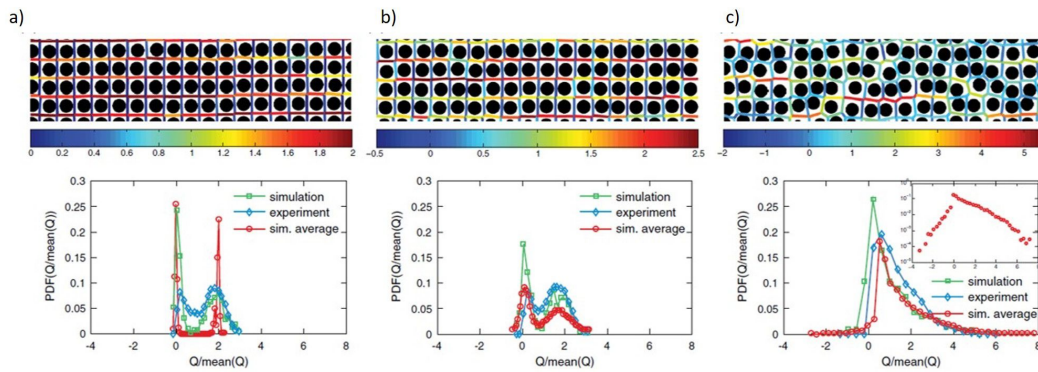
Figure 4.2: Images from left to right show effect of increasing disorder. ***a)*** At low disorder, the distribution of flow is almost completely dominated by the fast advective lanes flowing left to right, and the slow vertical diffusive lanes connecting the faster lanes. ***b)***As disorder is increased and thus the standard deviation of pore throat sizes, the distribution of flow changes into an exponential distribution of flow speeds. Figure reproduced from Alim et al [67].

the medium. At the microscopic level, the fluid will tend to favour larger pore throats and thus flows faster through certain pathways than others, since these throats will generate less drag and be easier to move through. But it is only by understanding how this mechanism acts over a complex network of pore throats that it becomes clear why certain branches, or lack of, emerge in macroscopic patterns. If all pore throats are of the same size and are parallel to the axis at which fluid flows across the system, for example from an inlet to an outlet, then fluid will flow through each pore at the same rate. What this means on the macroscopic scale is that an invading fluid will not contain "lanes" where the fluid flows faster which would lead to a smooth front, or uniform invasion pattern. One could then introduce disorder into the system, via varying particle sizes or positioning of the particles that make up the porous medium. In both cases, the size of the pore throats and the angle the pore throat is relative to the flow axis changes. If this is the case, fluid will now start to favour certain paths and fingers of more advanced invading fluid will start to form, destroying the uniform pattern that would otherwise occur with no disorder.

What is known so far, and is of importance to this project, is the effect disorder has on the distribution of flow speeds in a porous media (see [67]). For a porous medium where particles are arranged on a square lattice, the space between particles can be envisioned as a network of tubes. The standard deviation of tube sizes, which is a characteristic of the amount of disorder in the system, has been shown to directly determines the distribution of flow speeds throughout the system [67]. At low disorder, adjacent fast-flowing advective lanes, where the flow of fluid is the dominant mechanism for invasion of solute into these lanes, are connected by a slow flowing
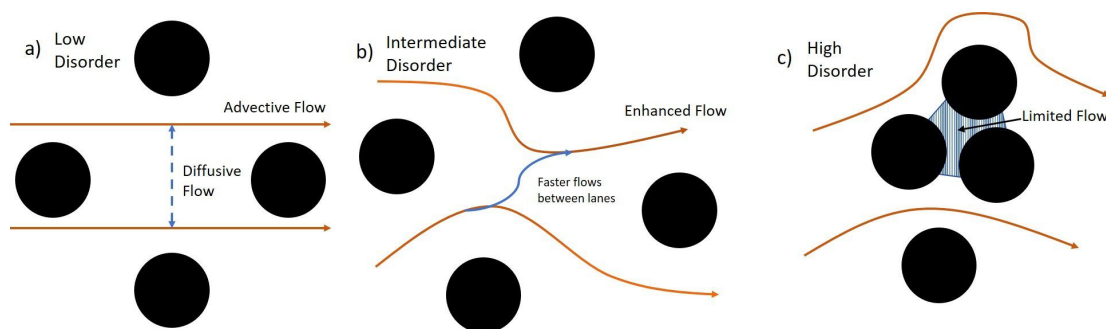
Figure 4.3: Effect of disorder on flow patterns. a) At low disorder, obstacles are regularly positioned on a lattice with fluid flowing from left to right. Fast flowing lanes are connected by slower flowing lanes. b) At intermediate disorders, obstacles are displaced from their original lattice position. This opens up the pores perpendicular to the flow axis and allows for faster flowing fluid between parallel lanes, which enhances the flow. c) At high disorders, there exist clusters of obstacles that are closely packed and areas where obstacles are far apart. This creates islands where flow between pores is severely restricted along with patches of much faster flowing fluid.

diffusive lane, where diffusion is the dominant mechanism for invasion of solute into this lane. This variation in flow speeds is almost constant throughout the whole system, and leads to two narrow peaks in the probability distribution function of the flow distributions (Fig 4.2a). This means that there are almost only two distinct flow speeds, the speed of flow in the advective lanes and the speed of flow in the diffusive lanes. As disorder increases, along with the standard deviation of the tube sizes, these sharp peaks transition into broader Gaussians (Fig 4.2b). Further increasing the disorder finally transitions these Gaussians into a singular exponential distribution of flow speeds (Fig 4.2c), with the distribution decaying with increasing flow speeds. This project expands on this breakthrough work, and looks to investigate how solute transport via fluid flow is affected by this evolution of flow distributions with increasing disorder.

The underlying mechanism for mass transport in porous media can be described by imagining a well-organised porous system where the obstacles that make up the porous medium sit on a regular lattice (Fig 4.3). The system can then consist of a rectangular array of obstacles, with fluid injected from one edge, and flowing out the opposite edge. If a fluid containing particles much smaller than the obstacles that make up the porous medium is injected into the system, then the majority of the fast moving particles flow along the same direction as they are injected. This then leads to lanes of fast, advective flow which are perpendicularly linked by slow, diffusive lanes. In the sketch presented in Fig 4.3, the net flow of particles can be seen to be to the right.

However, introducing disorder into the system by randomly shifting the particles that make up the structure of the porous medium away from their original lattice positions causes the symmetry in the system to break. Throughout the porous medium, pores that only contained slowly moving flows transition into fast-flowing pores as pore throats open up and flow is enhanced by the mixing between lanes. However, what also happens with increasing disorder is the emergence of areas of closely packed particles. In this scenario, flow into these pores is restricted and the pores are only invaded by slow-moving diffusive flows. The opposite case also arises, where there are areas of large open pore throats which contain the fastest flowing fluid in the system. Investigated here is how increasing disorder, and therefore transitioning between the three stages of ordered fast/slow lanes, well-mixed lanes, and the emergence of patchiness, will affect the flow of transported material like dissolved solute or suspended particles.

## 4.1 Methodology

The general methodology for manufacturing the experimental systems is outlined in Section 2.1. Summarised here are specific modifications to the manufacturing process needed for this particular project. The experiments described in this chapter make use of microfluidic chips with different levels of disorder, through which fluids are pumped that carry fluorescein dye or tracer particles.

### 4.1.1 Manufacturing

As with other chapters, soft lithography techniques are implemented to produce the micromodels used for these experiments. For this, a chrome-quartz photomask is used alongside SU8-3025 photoresist to create a reusable mold. From this, poly(dimethylsiloxane) (PDMS) can be poured into the mold, cured and cut out to create a PDMS copy of the design. This PDMS is then primed in an oxygen plasma and stuck to a similarly primed PDMS-coated glass slide.

For this project, the porous medium consists of solid cylindrical pillars of height $60\mu$m $\pm3\mu$m are made following the method described in Chapter 2. The height of these pillars are measured using a Dektak stylus profilometer where height profiles are taken across various areas of each master mold and across the different designs. The pillars linked to a hexagonal lattice and form into a rectangular porous medium as a whole (Figure 4.4). At either end of the rectangular area are two large circular regions into which holes are punched, allowing tubing to be inserted. Fluid is injected through one of these holes and exits the system via the opposite hole. Connecting these circular regions to the rectangular region is a symmetrical network of branching channels. The channels are designed so that a sharp step in the injected concentration of particles or
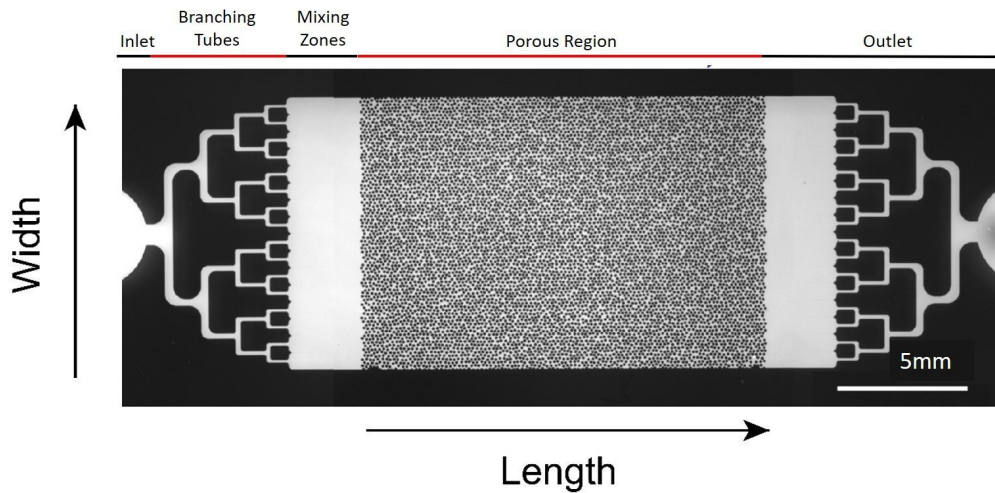
Figure 4.4: Image of porous system realised in a microfluidic chip. The system is made up of an inlet and outlet at either end which is carefully made by punching a hole to allow fluid to enter. This leads to a set of branching tubes with a geometry designed to produce a smooth fluid interface upon entering the mixing zone. The majority of the system is made up of the porous region, with obstacles designed using a MatLab code. Figure reproduced and adapted from [91].

dye will not spread out too much before reaching the porous area. How the geometry of these channels was finalised will be explained in more detail in Section 4.1.2. The open rectangular area directly after the inlet channels allows for the concentration of particles from each channel to mix before entering the porous area, further helping to create a flat front of concentration.

The porous medium is designed around a MatLab code provided by Karen Alim and Felix Meigel, to allow matching geometries to be studied numerically [97]. In the design process, pillars of diameter $120\mu$m are initially situated on a hexagonal lattice with lattice length $162\mu$m. Disorder is then introduced into the system by then randomly shifting each pillar by a percentage of its diameter in a random direction. However, if 2 pillars are within $10\mu$m of each other, the pillars are reset back to their original lattice position and randomly shifted again until they meet this criterion. This is to accommodate any manufacturing errors that can occur, which for my purpose means that if any two objects are within $10\mu$m, this may cause them to overlap or not form properly. The percentage shifts chosen were 1%, 6%, 11%, 16%, 26% and 56% of the pillar diameter. The wide range of disorders used allows for different regimes of disorder to be investigated, with the intermediate disorders chosen based on numerical results which identified a regime of interest.

### 4.1.2 Dispersion Experiments

The aim of the experiments was to track a sharp front between water dyed with fluorescein dye, and undyed water, as the front passes through a porous medium. To help define the fluorescein dye within the porous medium, the chips are kept within a large black box to block out external light. Within this box are the chips themselves, a UV light to cause the dyed-water to fluoresce and a digital SLR camera used to record how the dyed-water flows through the system (Fig 4.5). The camera is connected to a computer located outside the box. A syringe pump, also outside the box, is connected to the chips by a PTFE tube. This syringe pump is used to inject the dyed-water and is controlled by the same computer that is connected to the camera. Before injecting the dyed water straight into the chip, plain water is first injected via one inlet until the meniscus emerges from the opposite outlet. The system is then left for some time until any air bubbles that are generated from the injection of the water dissipate by dissolving through the PDMS. A tube containing the dyed-water was next connected to the external syringe pump and then inserted into this outlet to avoid an air bubble being generated between the plain and dyed water. This dyed water is then pushed through the system via the syringe pump at a set speed. Images are then taken at 30 s intervals until the entire system has been flushed with the dyed water. The UV lamp was turned on and off again in sync with the images being taken. This was to avoid over-exposure of the fluorescein by the UV light, which would have affected the measured intensity over the 30 minute period that the experiment took, due to bleaching of the fluorescein molecules. When the molecules are excited by the UV light, they become susceptible to interactions from other molecules. This can lead to permanent changes in the molecules and over long enough time will reduce the intensity of the dye [98].

### 4.1.3 Optimising Microfluidic Design

After initial experiments and analysis, an issue was found that led to unreliable results. Due to the design of the inlets used for injection into the porous media area, plumes were arising that eventually influenced the leading front later into the injection, as shown in Figure 4.6(a).

The first approach to try and reduce this effect was to add another layer of smaller branches that are closer together, with the intention of creating a flatter interface before entering the porous media. However, while slightly improving the front, the undesired effect was still significant enough to cause issues with the final results, see Figure 4.6(b).

To try and further reduce this effect, I used ANSYS [99] to create a finite element model of the microfluidic chip in which I solved for the equilibrium laminar flow profile to test a range of inlet designs and the resulting front they produce. This also allowed for flexibility in testing new
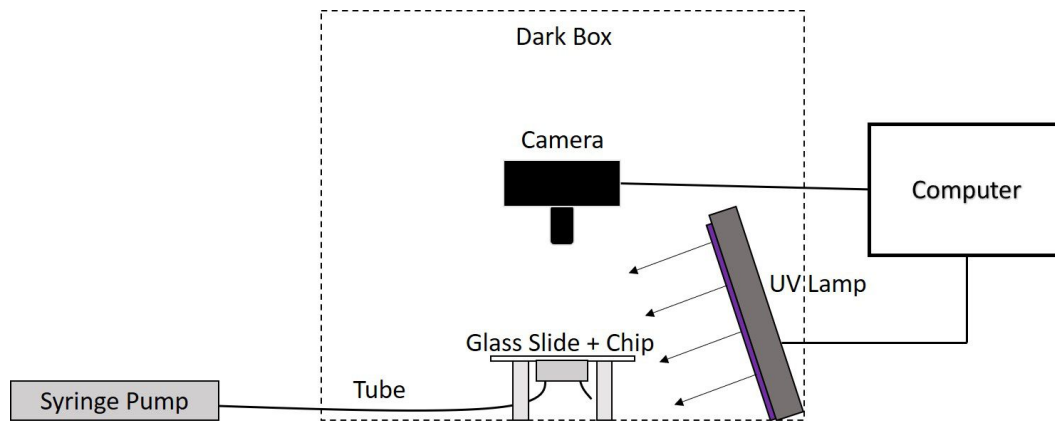
Figure 4.5: Setup used for experiments. A PDMS chip and glass slide is placed on top of a set of metal pillars to keep the chip level. This is then placed under a camera with the glass slide facing towards the camera. This is done to allow for easier imaging of the fluid and pillars in the chip. A UV lamp is placed next to this to illuminate the chip. All of this is kept inside a dark box to block out external light when imaging the fluorescein dye. A PTFE tube is connected to an external syringe pump and is used to inject the dyed-water into the PDMS chip. The lamp and camera are then controlled by a computer outside the dark box. This allows for images to be taken without having to open the box during the experiment.

inlet designs at various different flow speeds prior to manufacturing them. Initially, designs were made with right-angled branches that joined up at the end of the series of inlets, to encourage the concentration front from the inlet to evenly spread out in the open area before reaching the porous medium (Figure 4.7(a)). However, this still seemed to produce plumes after exiting the inlets and was therefore not a suitable design.

Following on from the idea of allowing the concentration from each inlet to spread out before reaching the porous area, in the ANSYS finite element model another layer of inlets was added that were closer together, as shown in Fig 4.7(b), and the concentration should therefore be able to merge to its nearest neighbouring inlet. This idea comes from the improvement in the concentration front between Fig 4.6(a) and Fig 4.6(b). While to some degree this was the case, it still created fewer but larger plumes originating back from the 2nd split in the inlets and meant that the concentration was still not a flat front as hoped.

Another ANSYS design attempted to make use of the fact that the concentration was already diffusing inside the inlets before it had chance to reach the porous medium. The idea was that if the length of each inlet tube was reduced, and therefore the time taken to reach the open area was also reduced, then there would be less time for the concentration to diffuse and mix prior to the experiment in the porous region, as shown in Fig 4.7(c). This was combined with the
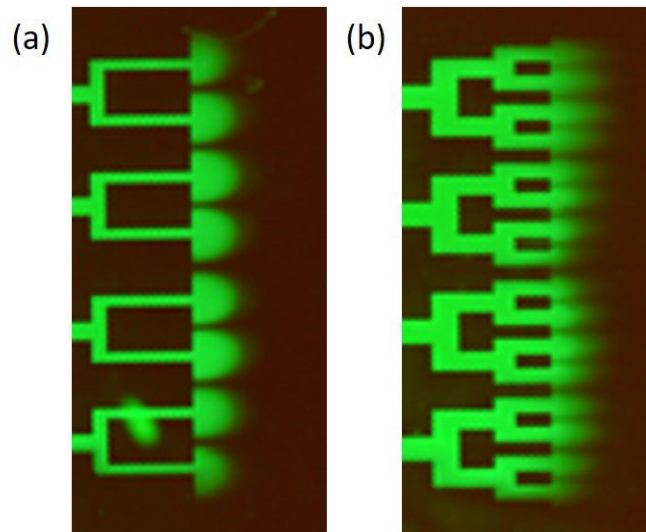
Figure 4.6: Plumes produced by branching tubes can be seen in the mixing zone of the system. a) The initial designs had a thin set of branching inlets leading into the mixing zone. This produced plumes and a ragged concentration front, which would have affected measurements of the concentration within the porous region. b) To try and address this, the tubes were first widened and another layer of branching tubes was added. While this reduced the size of the plumes, there was still an effect which caused gaps in the dye upon entering the mixing zone. It is also noticeable that the plumes aren't as advanced as each other and that plumes close to the edge and the center are lagging behind other plumes.

previous idea of trying to get the concentration from each inlet to merge smoothly. This still led to plumes being generated before the concentration front could enter the porous medium. However, this meant that the source of the problem did not come from either the length of the tubes or the distance apart, although these did have some effect on the resulting invasion.

As a result of the above designs, it was noticed that in most of the simulations there appeared to be stagnation points at the corners of each layer of inlets, for example these can clearly be seen by the bright low-concentration points in the corners of the feeding channels in Fig 4.7. This meant that when each set of inlets split, some of the front reached the final inlet layer faster than other routes. A few designs were than tested to see if the removal of these stagnation points would lead to a smoother front. Firstly, as shown in Fig 4.8(a), the existence of sharp corners in the inlets was removed with the idea that without these corners the stagnation points would not be able to arise. However, in this first design, because of the way in which the inlets were designed to allow for no sharp corners, the paths from the injection point to the exit of the inlets was not equal and therefore created a very rough invading front.

Secondly, rather than attempt to completely remove the corners, the corners were rounded
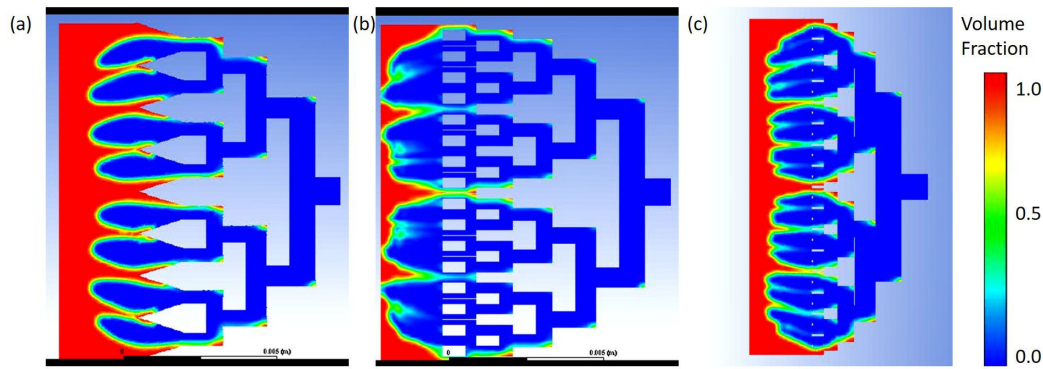
Figure 4.7: ANSYS simulations of different branching inlets. (a) Inlets end with a set of narrow angled openings, aimed at allowing the dyed-phase to spread out before mixing with the dye from other inlets. However, the dye phase didn't spread as planned and the plumes were still produced. (b) For this design, another layer of inlets was added aiming to force the plumes from each set of inlets close enough together to be able to mix. This removed some of the individual plumes but instead created a set of 4 large plumes. (c) In this design, the aim was to allow for the dyed to spend less time inside the inlets before entering the mixing zone. To do this, the distance between each split in the inlets was reduced. Again, while this removed some individual plumes, there still existed a smaller amount of larger plumes.

slightly with the hope that this would remove the stagnation points, or at least reduce their effect, see Fig 4.8(b). While this had a positive effect, it still did not lead to an ideal flattening of the front, with even more stagnation points arising within the inlet tubes.

Finally, the inlet channels were thinned, with the idea that narrower tubes would mean that the fluid would be forced to fill the corners of each tube and therefore remove the stagnation points. This was again combined with another layer of inlets that were close together to allow the concentration to merge before entering the porous medium, as shown in Fig 4.8(c). The resulting flow was one that created a far smoother front than had been previously seen, and a complete removal of the stagnation points within the tubes. This design was therefore reproduced in QCAD and made into a photomask to produce the micromodels.

After optimisation of the imaging process at NTU, it was decided to make use of the imaging setup of our collaborators at the Max Planck Institute for Self-Organization and Dynamics to complete the final measurements in the chapter at the highest possible intensity resolution and accuracy. However, as a result of Covid-related travel restrictions, this was not possible to do personally. As a result, chips were fabricated and prepared at NTU, then shipped to our collaborators, where the experiments were run by my colleague Leonie Bastin. The methodology remained the same for the experiments, except for the imaging protocol, as a specialised fluo-
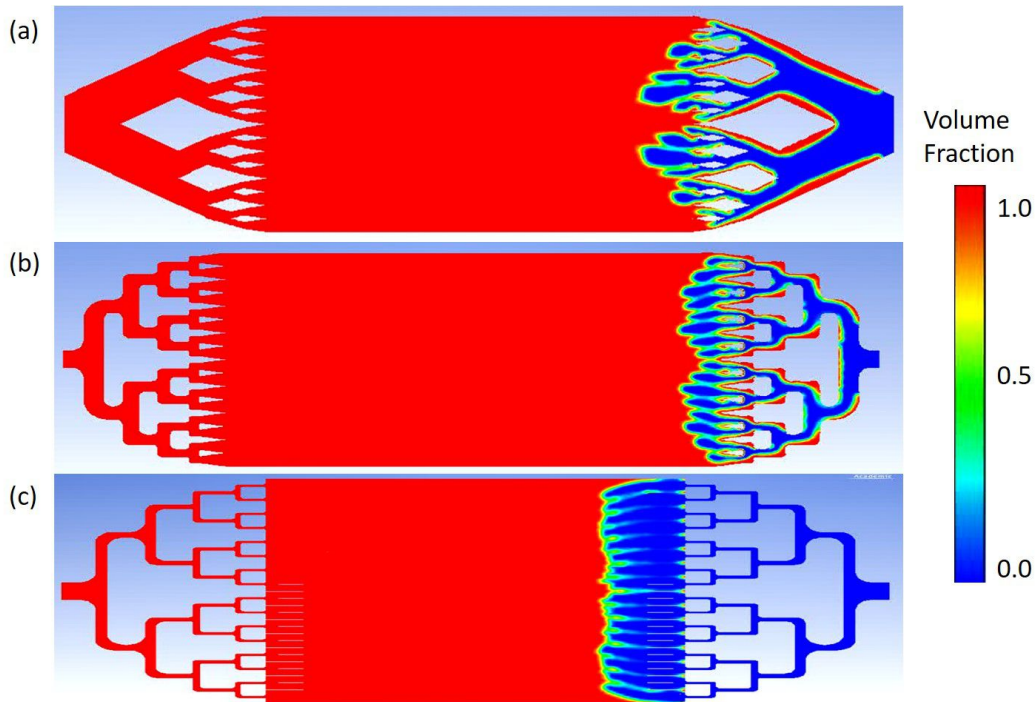
Figure 4.8: ANSYS simulations of different branching inlets focusing on removing diffusive regions within the inlets. a) Inlets where corners were removed altogether so that diffusive pockets shouldn't exist. However, diffusive areas still existed at the sides of the tubes and caused a very uneven front leading into the mixing zone. b) Rounded corners were used instead of sharp corners aiming to allow the dyed-phase to enter fill the corners. The dye, however, still struggled to fill the tubes, although the plumes entering the mixing zone were closer together than previous attempts. c) Rounded corners were used again, but the tubes were thinned until the final layer of inlets. By thinning the tubes, the dyed-phase was able to fill the tubes and help produce a smooth front leading into the mixing zone. This design was used for the final experiments.

rescence microscope was used, capable of calibrated intensity measurements of the entire chip simultaneously.

### 4.1.4 Image Analysis Process

Each experiment consists of a series of images taken at a regular time interval until the fluorescein-dyed water saturates the system (see Fig 4.9). Each of these images are analysed so as to create a picture of how the concentration in the system evolves over time.

MatLab is used to analyse the resulting images. Images are first rotated so that they all align, with the dyed-phase flowing vertically downwards. A rectangular section of the porous medium is chosen to be analysed and is cropped from each image, as shown in Fig 4.10(a). The
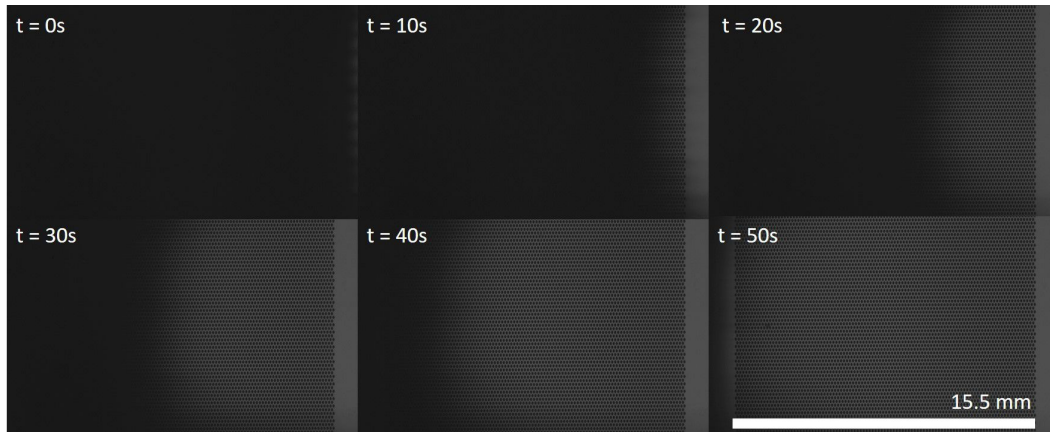
Figure 4.9: Experimental images of fluorescein dyed-water being injected into a water saturated system. The system has 1% disorder and the dyed-phase is injected at a rate of 300 µL/h. The dyed-water is injected until the dyed-phase fills the system, as seen at $t$=50s. Images are taken by Leonie Bastin

red channel is then extracted from each image. An image for normalising the intensity values is then created by averaging the final 3 images in the sequence, when the dyed-phase has entirely filled the system. A mask image is created using the final image in the sequence, which will be used to ensure that the pillars do not affect intensity measurements across the length of the section being analysed. For this, a threshold value is set for every pixel, which if a pixel is equal to or less than will be set to 0 or if greater than will be set to 1. This leaves the pillars as objects that stand out from the surrounding fluid area. However, rather than rely only on thresholding to outline the pillars, the center coordinates of these objects are then used as the coordinates to place circular objects of a given radius. This gives the final mask image which is used to determine which pixels within the fluid area are of interest and which corresponds only to the PDMS pillars, see Fig 4.10(b). Before each image is analysed, a Gaussian filter of width = 3px is applied to the images to reduce noise close to any obstacles. The resulting filtered picture is then normalised by dividing the image by the average reference image of the last 3 images in the sequence. Finally, the images are multiplied by the binary mask image to select which pixels are to be analysed. Any pixels that are 0 in the mask image will set the same pixel in the product image to NaN, otherwise it will keep its normalised intensity value, as shown in Fig 4.10(c) and Fig 4.10(d).

To generate an intensity profile, the average pixel value of each column down the width of the image is calculated, ignoring any of the NaN values produced by the mask image. This is done across the length of the image to produce an intensity profile that changes over time as the dyed-phase progresses across the system, shown in Fig 4.11. To calculate the front width, the
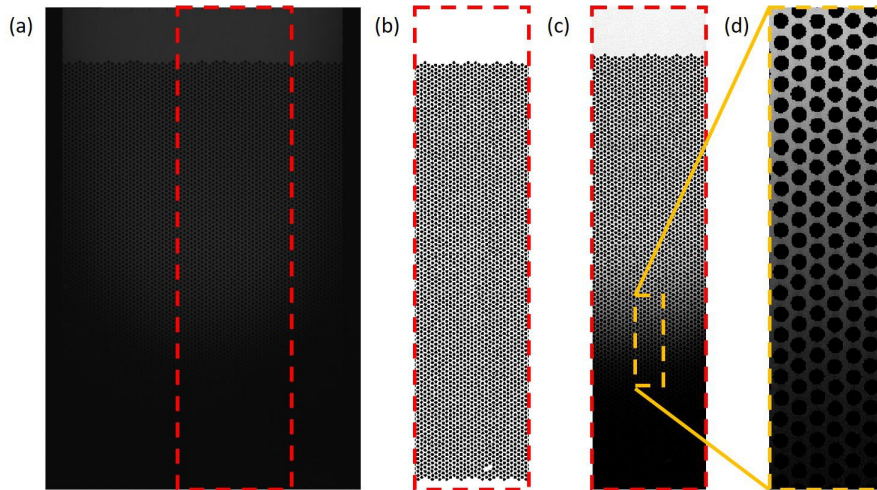
Figure 4.10: Image analysis process for dispersion experiments. a) A slice of the system is chosen for analysis to avoid potentially unreliable intensity measurements near the edge of the chips. b) A mask image is produced of cropped area. Mask is produced by thresholding the cropped area and then placing circular objects over the center of the objects detected in the thresholded image. c) The mask can then be placed over the greyscale image so that obstacles and the regions around the obstacles have intensity values set to NaN, so as to reduce the effect of camera resolution on the final results. d) Close-up of area in masked greyscale image.

intensity profile is cut at the 0.75 and 0.25 mark, and the distance between these two points is calculated.

For the original experiments performed at NTU, looking at the profiles, an issue that arose from this analysis was that the profiles, which are normalised against the final image in the time series, consistently rose above 1, see Fig 4.12. This should not be the case as it implies that the concentration in some areas in greater than the maximum possible concentration that occurs when the medium is fully saturated. Further exploration into this found that part of these effects resulted from pre-processing and a non-linear response of the digital camera to increasing illumination. While they were reduced by going to a raw or fully uncompressed image format, these systematic distortions of the intensity signal were not eliminated. As such, we planned to replace the SLR digital camera by making use of an illumination-calibrated imaging system available at our collaborator, see Section 4.1.3. While it was originally intended that I prepare these experiments and then bring them there to perform them myself, as a result of international travel restrictions, the experiments were performed on my behalf by Leonie Bastin using the more suitable intensity measuring equipment. The resulting profiles produced from these images, following the same protocols that I had already developed, are closer to what was
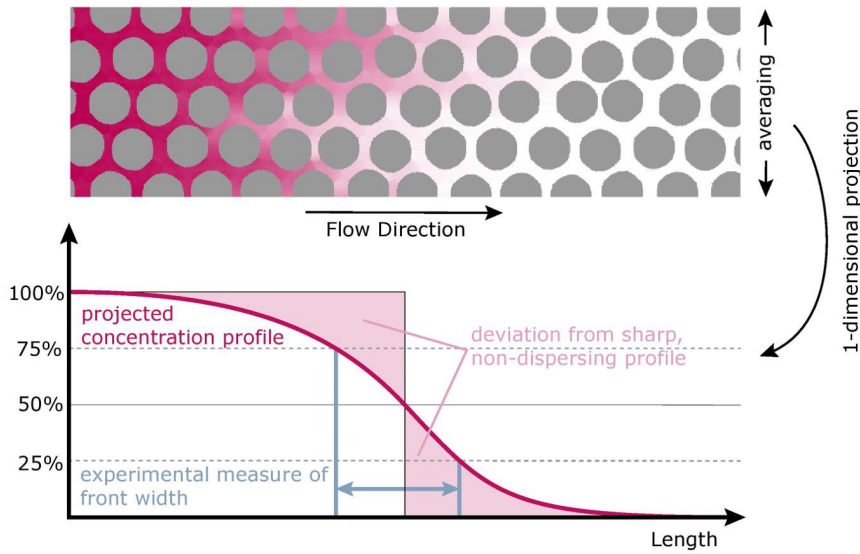
Figure 4.11: Experimental images are translated into intensity profiles. Here, we can see how taking an intensity profile along the length of the chip begins to fade as measurements lead into the non-dyed phase. The graph also shows how the profile would look for the theoretical example of a simply diffusive concentration. Reproduced from [91]

expected and were suitable for extracting results from (Figure 4.13).

In order to characterise the dispersive effects, a simple metric was found to be most robust, and to allow for direct comparison between experiments and a numerical model of the corresponding process. Of particular interest, is the image when half the maximum concentration has reached half the length of the chip. At this point, we look at the distance between when the profile crosses the 75% and 25% marks of the relative intensity. We classify this distance as the front width. For a sharp front, where dispersion of the dye has not occurred, the distance between these two points will be small. For the opposite case, where the dye has spread out due to effect of diffusion and dispersion, the distance between these two points will be greater, meaning a larger front width.

### 4.1.5   Numerical Model

To explore the effects of disorder on dispersion more completely, a numerical simulation of the process was developed by Felix Meigel and Karen Alim at the Max Planck Institute for Dynamics and Self-Organization. Here, I will summarise the details of their model, similar to how we present it in a joint paper [91].

To simulate the spread of a diffusive solute in the porous media, a Crank-Nicolson routine
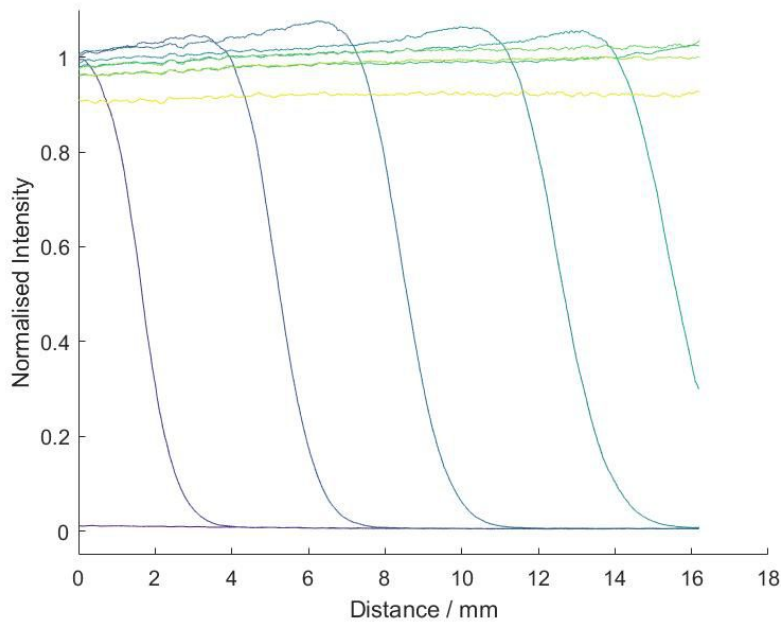
Figure 4.12: Series of intensity profiles taken from experiments. The intensities, ignoring intensities defined by the mask image, are calculated along the length of the system by averaging intensities down the width of the system. This is then done for each image in the experiment to show how the intensity values evolve over time. The values are normalised against intensity values taken from when the dyed-phase fully saturates the system.

was employed [100]. To this end, the porous media was interpreted as a network of tubes and solute transport by the means of advection and diffusion were considered. The simulation routine involved three major steps: in a first step the porous media the network structure was extracted by skeletonization of the experimental domain. In this step, also the varying radius of tubes were extracted. Equipped with a porous network structure, the hydraulic resistance along each tube was computed under the assumption of slowly varying radii along the tubes. In a second step, Kirchhoff's circuit laws were employed to compute the flow profile in the network. In a third step, the network topology and the flow profile are used to numerically integrate the advection-diffusion Eq 4.6 along individual tubes using a Crank-Nicolson integration routine. To minimize numerical artifacts, tubes were approximated with circular cross-sections. At junction points, merging and splitting conditions were implemented analogous to the Crank-Nicolson routine along individual tubes. To avoid boundary effects, a different padding of the porous medium was used, in contrast to the experimental routine, as an empty area in front and behind the porous medium is prone to numerical artifacts during skeletonization. Instead the individual tubes in the beginning and end of the porous medium were elongated by a factor of 4. Along the inlet
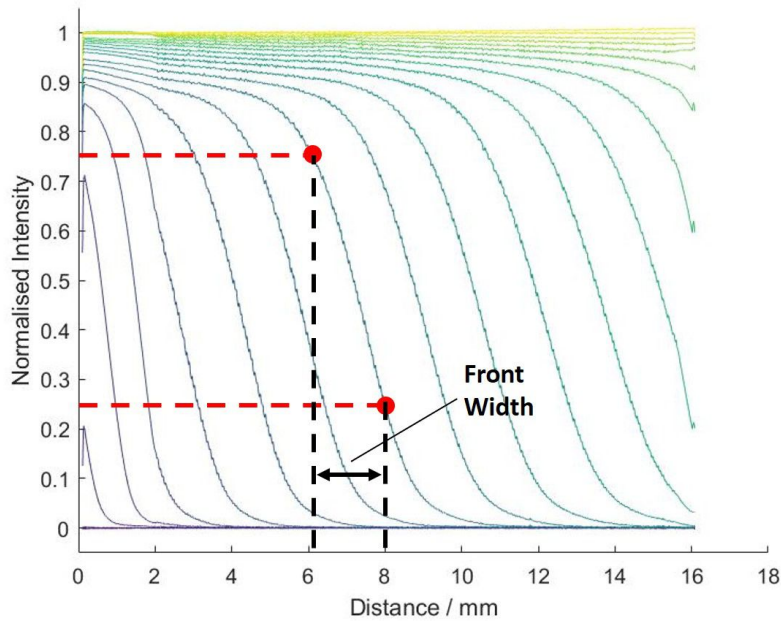
Figure 4.13: Series of intensity profiles taken from experiments run in Germany by Leonie Bastin. Intensities are measured in the same way as explained in Fig 4.12. The profiles are now improved by taking the images using an illumination-calibrated imaging system. Shown here, is how the front width is defined. This is the real-space distance between the positions of the 0.75 normalised intensity value and the 0.25 normalised intensity value.

side of the porous medium, a fixed concentration $C_0$ was set. At the other end of the porous medium an open outflow condition was implemented, which estimated transport by advection and diffusion over the last simulation point. A constant pressure drop across the porous medium was implemented, and for all simulations the same $P_{in}$ was set at every inflow tube and the pressure $P_{out}$ at every outflow tube. The simulation routine was thoroughly tested to reproduce analytical solutions in simple network geometries (Data not shown, see [97]). To simulate the spread in different network for different Péclet numbers, instead of the flow velocity the diffusion constant was altered, granting better numerical stability.

## 4.2 Results

### 4.2.1 Particle Tracking

The following particle tracking work was done in collaboration with and while supervising MSc student Matthew Bates.

Before macroscopic transport in a disordered medium was investigated, initial experiments

were performed to confirm that the microscopic flow in the systems matched what was seen in previous work [67] and that the underlying idea of symmetry breaking influencing transport in the fluid was correct. To investigate this, a technique known as digital particle image velocimetry (PIV) is implemented to non-invasively visualize the distribution of flow in a sample. Microparticles (1 $\mu$m polystyrene) were selected after testing a variety of sizes and volume ratios to produce the best images for analysis while not affecting the fluid flow. Particles in a 1:10,000 particle/water suspension were found to produce the suitable density of particles such that the imaging software could still track each particle but that the size and amount of particles was not too great that pores would get blocked and influence the fluid flow. Each experiment consisted of taking over 100+ images as these particles flowed through the system, along with a constant current of water.

An open-source tool (PIVLab) for MatLab was used to help understand how the flow speeds varied with different disorders. The software separated each image into "interrogation area", with pass 1 having a size of 128 pixels and pass 2 having a size of 64 pixels, and performed a cross-correlation. The resulting matrix was used to find the most likely displacement within each interrogation area. Once the displacement for each particle and the timestep between images is known, an average velocity for each interrogation area can be calculated and produces the colourmaps of the flow, as shown in Fig 4.14.

In Fig 4.14(a), it is shown for low disorders that the fast flowing particles follow the lanes parallel to the direction in which the particles were injected. This intuitively makes sense as in the absence of any disorder in the obstacle positions, the symmetry of the pores will mean that flow in the cross-channels will be small. However, for low disorders there still exists comparatively slow diffusion of the particles over longer time scales, seen by the measured flow speeds in Fig 4.14(a). However, Fig 4.14(b) shows that for higher disorders, lane mixing begins to occur. Here, because there are uneven flows in adjacent lanes, there must (by flow conservation) be a stronger mixing through the cross-channels. This transition from distinct lanes of slow and fast-moving particles at low disorder to mixing between lanes and a wider range of flows for intermediate disorders is consistent with the work previously produced in [67] (Fig 4.2). Confirmation of this effect for the systems produced here allows for the expansion of this previous work into investigating transport in the systems and what effect disorder will have on it.

### 4.2.2 Calibration

In order to measure the flow of concentration across the porous medium, fluorescein-dyed water was injected into the system and its intensity over time at various areas in the system was
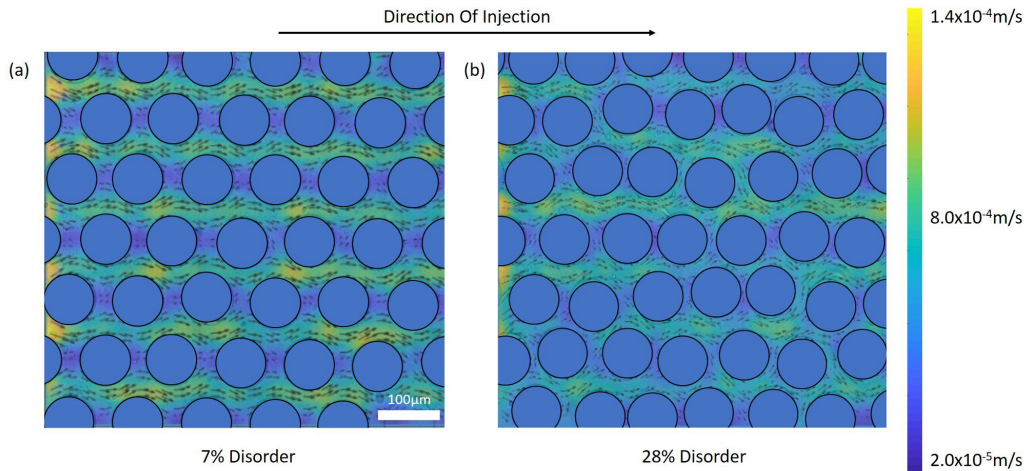
Figure 4.14: Initial experiments confirming effect of disorder on flow in a system with pillars situated on a hexagonal lattice. Blue represents low flow speed, with yellow being faster speeds. a) Low disorder system. Fast flow is in the lanes parallel to the direction in which fluid is being injected. These lanes are connected by slow lanes, where the microparticles move mainly through slow diffusion. b) Medium disorder system. Initially slow lanes become faster advective lanes as flows speed up around pillars. This results in initially fast lanes slowing as flow is directed elsewhere.

measured. However, a way is needed to relate the intensity of each pixel into a corresponding concentration. To do this, calibration experiments were performed by injecting solutions of various concentrations, ranging from $1.13 \times 10^{-5}$g/ml to $9.39 \times 10^{-3}$g/ml, of fluorescein-dyed water into an existing chip of thickness 60 $\mu$m. The fluid was pumped through the system until it exited through the opposite outlet and all pores are visibly filled with the fluid. An image of this uniformly dyed system is then taken. The same setup as shown in Fig 4.5 is used, with the analysis of the images varying for these calibration measurements.

Before measurements on each image can be undertaken, a mask image is created to identify which pixels in each image are most suitable for measuring the intensity. This is done because of the camera resolution and effects on intensity measurements caused by the PDMS chip itself. To select the suitable pixels, the image is converted into a binary black and white image and skeletonised (Figure 4.15) to reduce the effect that camera resolution has on the intensity close to the pillars. To do this, the image is rotated so that the length of the chip can be analysed (Fig 4.15a). The green channel of the image is extracted and a slice of the original image is cropped to ignore effects on intensity that occur close to the edge of the chips (Figure 4.15b). The cropped image is converted into a black and white binary image (Fig 4.15c) by thresholding the image. This is simple to do as the pillars contain almost no green colour and will be easily separated
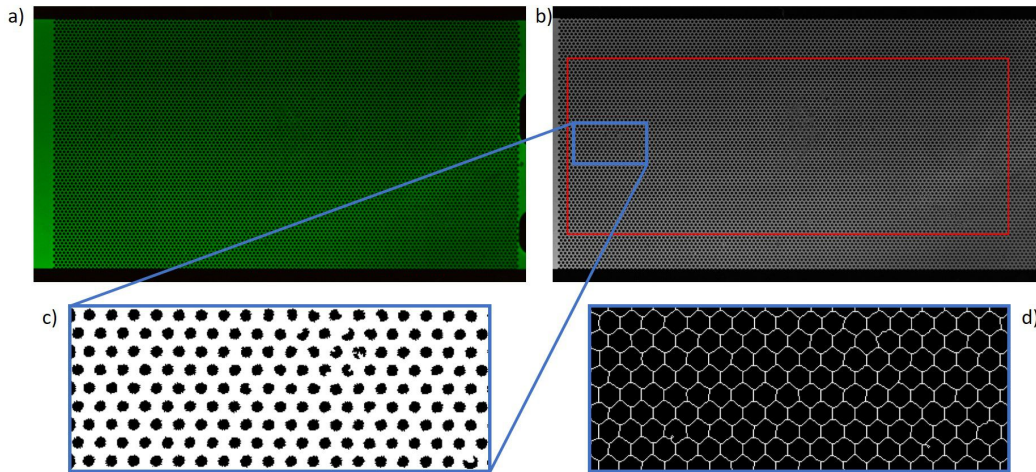
Figure 4.15: Image analysis process for calibration images. a) Chips are filled with only fluorescein-dyed water so that the maximum intensities for each concentration can be measured. b) Once the chip is filled, the green channel is extracted and a slice of the porous region is cropped. c) The image is thresholded to create a binary image where the obstacles have pixel intensity values of 0 and the fluid pixels have a value of 1. d) To ensure that the measurements of the intensity aren't affected by camera resolution near the obstacles, the thresholded image is skeletonised so that only the pixels in the center of the pores are measured. To do this, the thresholded image in (c) is eroded until only a network of 1 pixel wide lines remain. These pixels are used to select which greyscale pixels from (b) are measured to calculate an average intensity for the concentration used.

from the green fluid around them. The thresholded image is then eroded until only a skeleton of the system exists (Fig 4.15d). For this, starting from the thresholded image, any white pixels that neighbour black pixels are converted into black pixels until there exists lines only 1 pixel in width, which correspond to pixels along the midline of each pore and throat. These pixels are the same positions that will be analysed in each image going forward.

The greyscale values for all the pixels corresponding to the skeletonised pixels in the mask image are averaged to give an intensity measurement for the known concentration that was injected. This whole procedure is then repeated for a range of concentrations to produce an intensity vs concentration graph which can be used to find the local concentration values for each experiment (Fig 4.16). The graph shows that when the concentration reaches just above $2 \times 10^{-3}$g/ml, the intensity begins to saturate and adding more fluorescein to the solution causes the image to darken and hence the measured intensity to drop. There are a few reasons why this may occur. It may be that after the density of dyed to water reaches a certain ratio, multiple scattering causes the intensity of the fluorescent signal to dim rather than increase. It may
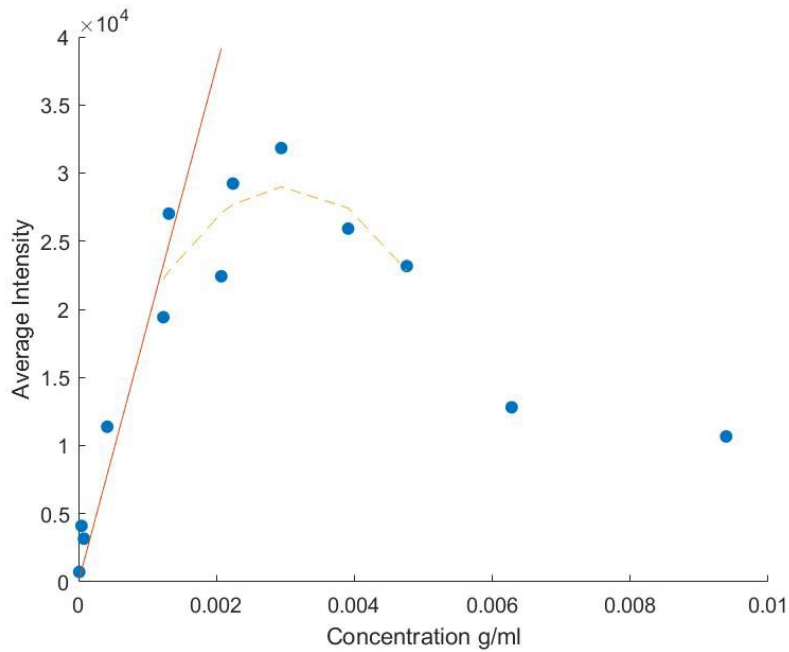
Figure 4.16: Average camera intensity measurements for various concentrations of fluorescein injected into a porous system. the pixel intensity of the dyed fluid rises linearly until around $2 \times 10^{-3}$g/ml, when the intensity begins to plateau and then drop. This is may be due to either automatic camera corrections or multiple scattering in the fluid.

also be due to automatic camera corrections, when it encounters a higher range of intensities. Finally, the reduction in intensity could be the result of fluorescence quenching [101, 102]. One plausible type of quenching is collisional quenching, when an excited fluorophore interacts with other molecules in the same solution and is deactivated. This effect is more common at higher concentrations and could be the cause of the trend shown in Fig 4.16. Either way, for the experiments that follow, the maximum concentration used was $2 \times 10^{-3}$g/ml. This meant that as the concentration would spread out over time, and therefore any area within the system should always have a concentration lower than $2 \times 10^{-3}$g/ml, and the concentration at each point could be reliably measured.

### 4.2.3 Front Width

The key experimental measurement in this chapter is a characterisation of dispersion, based on how much of a sharp concentration front spreads out as it invades a porous medium. As mentioned in Section 4.1.4, from the intensity profiles taken as dyed-water is injected into the system, we inspect the profile for when half the normalised concentration meets the halfway point down the length of the chip. The front width is then defined as the distance between the points
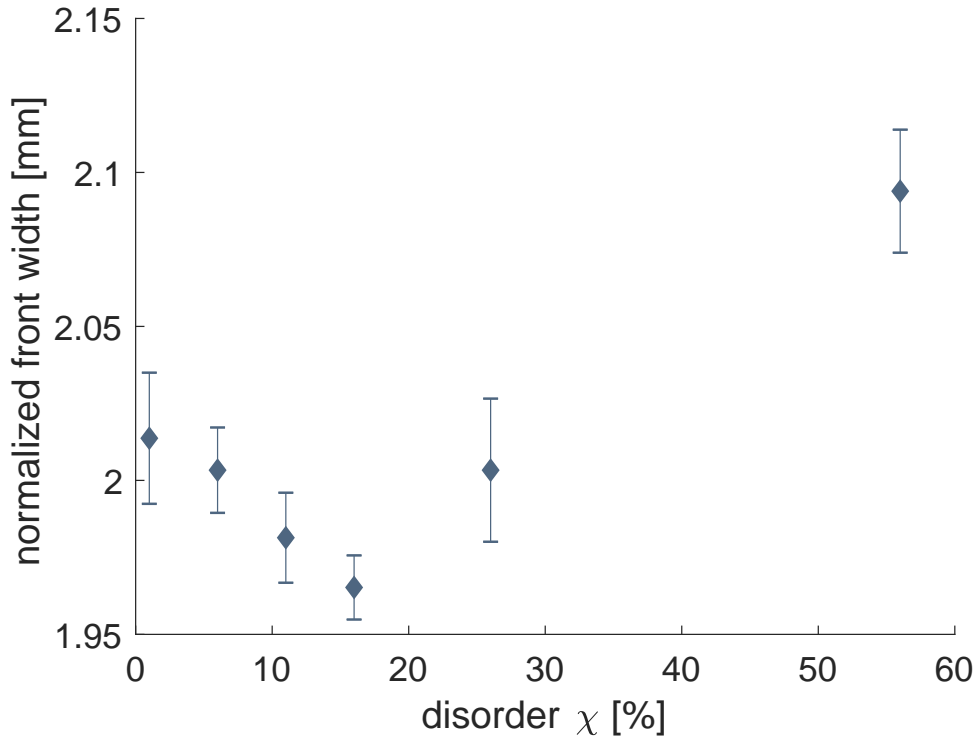
Figure 4.17: Scatter plot of experimental average front width measurements. Points represent average front width measurements on the normalised intensity profiles for each set of disorders along with standard error associated with each average. Graph shows non-monotonic trend with increasing disorder.

where intensity, $I = 0.75I_{max}$ and $I = 0.25I_{max}$, as shown in Fig 4.13. From this definition, it can be seen that for a dyed-phase with a sharp interface and a flat invading front, this distance will be almost 0. However, even with a sharp interface, if the front is slightly curved then this will cause the front width to increase. This is due to average intensity measurements across the width of the system meaning that the intensity profile will not suddenly drop to 0 as with a flat invading front. Alternatively, if there is a flat invading front, but the interface is not sharp, meaning the amount concentration gradually declines going into the non-dyed phase, this will also cause the front width to increase.

The major result from these experiments, and the corresponding simulations, is the appearance of a non-monotonic trend in the front width as disorder is increased (Figure 4.17). This is not initially an obvious result, as it would easily be expected that increasing disorder would increase the amount of dispersion that occurs, and therefore increase the front width. For the rest of the chapter, I will focus on elucidating and explaining this result.

For low disorders, there is a slight decrease in the variance of the measured front width as

disorder is increased, which can be understood by looking back on Section 4.2.1. This regime relates to the transition from Fig 4.3a to Fig 4.3b. For no disorder, there exist diffusive pockets between lanes into which dyed-water may only slowly fill. These diffusive pockets will cause the front to spread out because they will trap volumes of low-concentration fluid behind the advancing front, which will slowly mix with the incoming fluid, diluting it. For any measure of intensity across the length of the chip these regions will also contribute to small areas of lower intensity behind the front of the flow. Both of these effects mean that the front width will be larger than if all the pores behind the invading front were uniformly filled. However, this case change for even a small increase in disorder. Now, the flow velocity into these diffusive pockets increases, and mixing between the lanes is permitted close to the leading edge of the invading front. In this case, almost all the pores behind the front are filled and a smoother front is generated due to the mixing. All this means that the front width will be reduced, and therefore the variance in the front width will also decrease slightly.

After this dip in variance for small disorders, the variance begins to rapidly increase with increasing disorder. This can be explained by referring to Figure 4.3c. Because of the large amount of disorder, pillars will now randomly cluster together to create areas of low flow velocity, and therefore the filling of these pores will only take place over considerable time scales. It is not difficult then to see how this would affect intensity profiles across the length of the chip, as rather than the relatively small trapped areas of low concentration that occurred for no disorder, there now exists larger areas of low concentration behind the main line of the invading fluid, which dramatically affects the size of the front width. Not only this, but at high disorders there exists slow diffusive lanes. Similarly to diffusive islands, which are pockets within the dyed-phase that are only filled by slow diffusion of the solute into the pores, these are long thin areas for which the dyed-water flows around, only filling slowly due to diffusion of the dye. These occur as the pore throats to access these lanes are restricted due to the added disorder in the system and the fluid favours other pore throats around these areas. These lanes will have a significant effect on the intensity profiles and will cause dips in the smoothness of the flow front.

We can compare the experimental results to those generated by the simulations (Fig 4.18) at a $Pe \approx 30$. Error bars are calculated over 6 measurements for both experiments and simulations. We find that the trends from both the simulations and experiments are in close agreement with one another. Most importantly, the non-monotonic trend appears in both the simulations and the underlying theory (see below). This helps to reliably prove that the trend is not due to any experimental errors and is in fact expected for the given geometry.

Theory derived by colleagues Karen Alim and Felix Meigel [91] can more closely explain why this non-monotonicity arises. To do this, the porous medium is constructed out of minimal units

termed junction blocks. These junction blocks consist of two consecutive parallel pores connected via a perpendicular pore, relative to the flow axis. Theory shows that the variance in first passage time, the time taken for a particle to exit a junction block via the opposite parallel pore or the perpendicular pore, can be approximated by a series expansion. However, for high $Pe$ values, the 1st and 3rd order coefficients of the expansion are found to be equal to 0. Furthermore, the signs of the first few non-zero coefficients can be shown to alternate in sign. Therefore, at these high $Pe$ values, the variance in the first passage time can be written as:

$$Var(T) \approx |\Lambda_0| - |\Lambda_2|\chi^2 + |\Lambda_4|\chi^4 \tag{4.10}$$

where $\Lambda_0$, $\Lambda_2$ and $\Lambda_4$ are coefficients and $\chi$ is the level disorder. This then predicts that for initially increasing, but still small disorders, the variance of the first passage time should decrease and for high disorders, where the $\chi^4$ term dominates, the variance will increase. This increase in the variance of the first passage time lends itself to the same non-monotonicity seen in the front width measurements. If the variance in the amount of time it takes a particle to enter and exit a pore junction increases, then so will the roughness of a concentration profile. When the theory line is plotted alongside experimental and numerical data, we find that it agrees closely with both for small disorders before increasing rapidly. While the values at higher disorders may differ, the trend of the theory agrees with experiments and simulations that a non-monotonic trend should occur.

### 4.2.4 Effect of Peclet Number on Results

To complement the result shown in section 4.2.3, the simulations produced by Felix Meigel and Karen Alim also investigated the effect of varying the diffusivity of the concentration, and therefore the $Pe$ number. Shown in Figure 4.19(a) is a qualitative example of how varying the $Pe$ number will have an effect on the flow of solute through pores for the same disorder.

For low disorder at high $Pe$, there exists pockets of low concentration which arise as the flow front progresses faster than they could be filled. When $Pe$ is lowered, diffusion effectively becomes more important and so these pockets are instead filled up over a similar time scale to the rate of progression of the flow front. This causes the front width to decrease. For very high $Pe$ numbers, the low concentration pockets are almost completely unfilled as the diffusivity is so low that these pockets are unable to be filled. Therefore, by the time half the concentration reaches halfway down the length of the chip, there now exists untouched pores that dilute the concentration profiles, further increasing the front width.

For high disorders at low $Pe$, pockets that usually contain low concentrations are instead
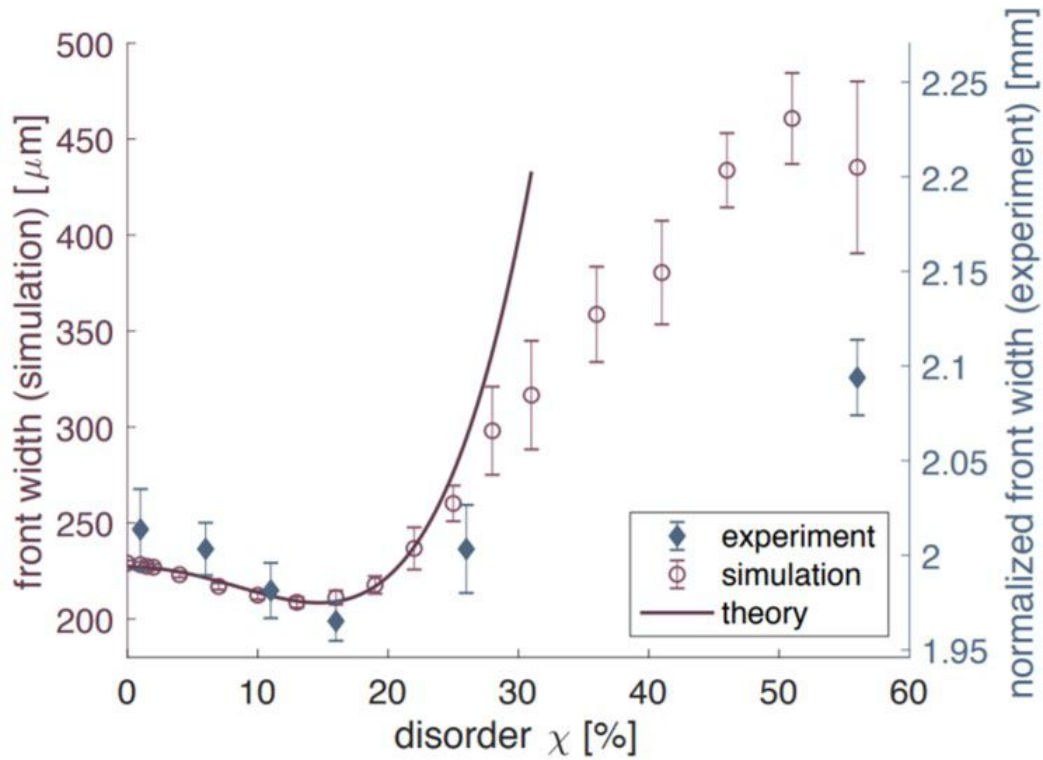
Figure 4.18: Comparison of front width measurements for experiments, simulations and theory. Simulations use different y-axis due to design of simulations but the non-monotonic trend still appears with increasing disorder. The theory also predicts non-monotonicity up until around 30% disorder. Experiments, simulations and theory are all performed at $Pe \approx 30$

filled before the front of the flow can reach halfway down the length of the chip. In this case, the flow throughout the system is dominated by diffusion, and therefore due to the disorder, the front width now increases as disorder increases. For high disorders at high $Pe$, the lower diffusivity means that lane mixing dominates and the front width decreases as a result.

This is shown quantitatively in Fig 4.19b produced in simulations by Felix Meigel and Karen Alim. Here, the perpendicular Péclet number, rate of advection vs diffusion in the direction perpendicular to the pressure gradient, is used from flow statistics. For low disorder, the front width first decreases at low $Pe$ before greatly increasing for higher $Pe$ values. Higher disorders will change in a similar manner but to a lesser degree. At low $Pe$, the front width remains higher than for low disorders and the non-monotonic trend seen before disappears. The front width then first decreases with increasing $Pe$ before increasing again. However, the front width fails to increase at the same rate at which the front width increases for lower disorders. This means that the non-monotonic trend will only exist for high enough values of $Pe$.
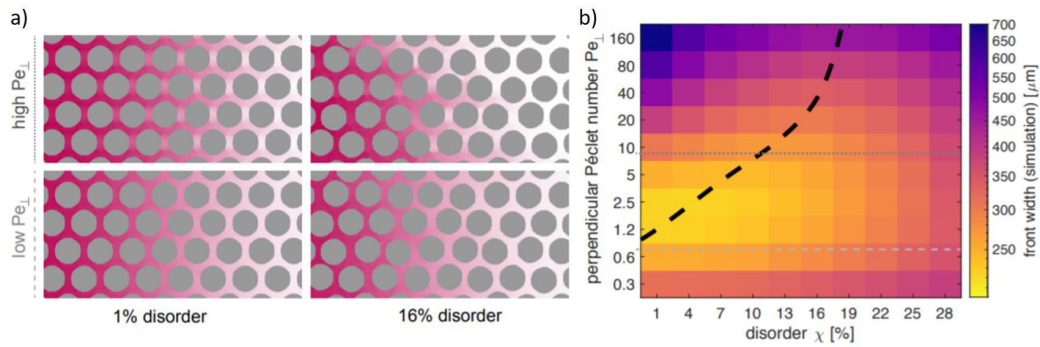
Figure 4.19: Comparing effect of $Pe$ at different disorders. a) Simulation snapshots show that a sharpening of the front width only occurs for large enough $Pe$ values. At low $Pe$ values, disorder only has a small effect when transport in all pores is dominated by diffusion. b) How front width measurements in simulations are affected by varying $Pe$ number. Grey dotted lines represent $Pe$ values used in (a). Black dotted line shows the disorder values where the minimum front width occurs at different $Pe$ values. Non-monotonicity only arises for $Pe \gg 1$. Figure reproduced from [91].

## 4.3 Discussion and Conclusions

The aim of this project was to investigate the effect that varying degrees of disorder would have on dispersive transport through a porous medium. To do this, analogue porous media were produced using soft-lithography techniques after development work was undertaken using ANSYS to find a suitable geometry for the system. To investigate dispersive transport in this system, fluorescein dyed-water was injected into an already water saturated medium held within a darkened box and imaged using UV fluorescence methods. Time lapse images were then taken until the dyed-water completely saturated the system. Image analysis was undertaken on the resulting images, with intensity profiles produced along the length of the system to see how the dyed-water concentration evolved over time in various areas of the medium. Most results were taken at the point when half the maximum normalised concentration value reached the halfway point down the system. At this point, the front width is measured by looking at the range between 75% and 25% of the maximum normalised concentration value. Simulations were also produced by colleagues Karen Alim and Felix Meigel to study the same effect, and the results compared to experimental data.

The surprising result of this work is the non-monotonic effect that increasing disorder has on the measured front width, shown for both experiments and simulations (Fig 4.18). This effect can be understood by looking at further experimental work done with particle tracking (Section

4.2.1). We find at increasing small degrees of disorder, lane mixing enhances the flow between parallel lanes and allows pores that were previously only accessed via slow diffusion to be filled faster, creating a smaller front width. This subtle effect is then overshadowed for larger disorders, as large areas of closely packed pillars prohibit fast flow and in turn create larger areas of low concentration, rapidly increasing the size of the front width.

Simulations also investigated what effect $Pe$ has on this non-monotonic trend, and found that it will only exist for large enough values of $Pe$ (Figure 4.19), as otherwise diffusion dominates and allows for more saturation before the front can spread out significantly. This is supported by analysis done by colleagues Felix Meigel and Karen Alim [91], which shows that for high $Pe$ values, the variance of the first passage time can be written in the form shown in Eq 4.10. This accurately predicts the non-monotonicity by showing how the variance will decrease with increasing disorder by $\chi^2$ before rapidly increasing as the term $\chi^4$ dominates. This non-monotonicity in first passage time allows us to understand why the front width therefore follows a similar trend. This graphical analysis helped to show that this only occurs for high enough $Pe$ values.

What this shows is that there exist optimal geometries that a porous system can take to improve transport efficiency throughout the porous medium. We can understand this by investigating how the interplay between advection and diffusion on a macroscopic scale affects the overall macroscopic transport properties. We then have to consider not only the rate at which fluid flows across the system, but also the disorder, and indeed the positioning of the obstacles. This positioning of the particles is what makes up what can be considered a network of tubes of various sizes. It is then the distribution of these tube sizes that dictates the flow distribution throughout the system, and therefore the transport of solutes around the system.

# Chapter 5

# Fluid Flow in Responsive Porous Media

So far in this thesis, ideas surrounding complex porous media have been investigated. This has included how correlations between particle sizes play an effect on the invasion of fluid and how disorder affects fluid transport and the mixing of solutes. In both these cases, however, the particles have been given a set position once manufactured, which they cannot move from. In some natural porous media [103, 104], the particles are not only disordered, but are able to be shifted or deformed by the action of fluid. This will then affect the remaining invasion process, as pore throats open and close as the fluid creates a pressure on the particles. For example, by pushing sediments around, this can create similar geometries to those seen in the previous chapters, with areas of small pore throats and areas of large pore throats [25].

In general, we can understand how deformation of the particles in a porous medium can lead to new invasion patterns by first looking at the pressure it takes to invade via a pore throat. The capillary entry pressure is given by Eq 5.1 where $P_c$ is the capillary entry pressure, $\gamma$ is the surface tension, $\theta$ is the contact angle, and $a$ the pore throat width:

$$P_c = \frac{2\gamma \cos(\theta)}{a} \tag{5.1}$$

From Eq 5.1, it is obvious that if the pore throat width $a$ increases, then the capillary entry pressure, which is the pressure required for the fluid to invade a given pore throat, will decrease making it easier to invade. Likewise, if $a$ decreases, then the fluid requires a larger pressure difference to invade. So if a particle deformed or shifted from its original position, then the value of $a$ will also vary depending on the type of change that occurs. Initially preferential pathways could be ignored as the invading fluid now explores different pores, given the changes in entry pressures. What this can lead to is a new type of invasion pattern, termed here as *capillary fracturing*, which has been experimentally investigated previously (Figure 5.1) [40]. These fracturing patterns are qualitatively identifiable by the presence of only a few thin fingers that invade only a small amount of a porous region before exiting the system. In other words,

a. viscous fingering     b. capillary fingering     c. fracturing
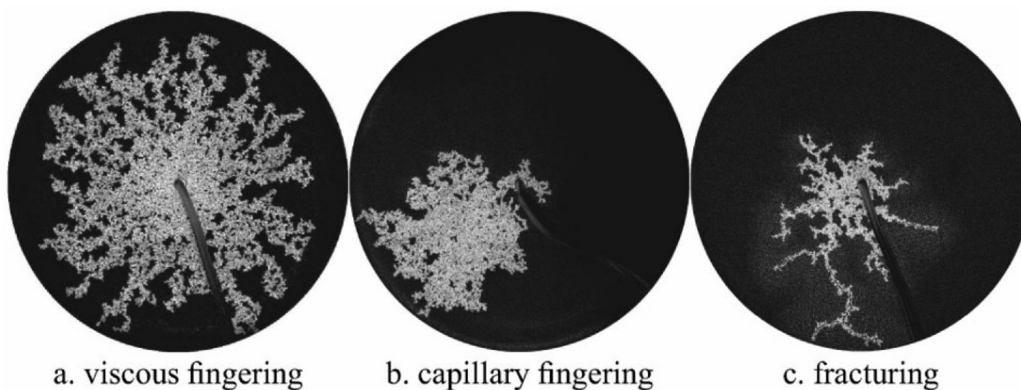
Figure 5.1: Transition towards capillary fracturing in granular media. Thin layer of water-saturated glass beads confined in cell with weight applied. White area shows invasion pattern produced from air injection into the center on the beads. a) Viscous and b) capillary fingering patterns occur when mechanical forces resist hydrodynamic forces, and c) a fracturing pattern occurs when hydrodynamic forces dominate. Figure reproduced from [40].

in the language employed in Chapter 3, it is a highly inefficient invasion pattern. This pattern is found to occur when the capillary entry pressure, $P_c$, of a pore throat is comparable to the pressure that would move the obstacles that surround that pore throat.

In the work done by Holtzman et al. [40], air was injected into a water-saturated bed of glass beads, with a weight placed on top. In Figs 5.1a and 5.1b, the invasion pattern depends on whether viscous or capillary forces dominate, and such patterns are common in fixed porous media. This limit applies to this case when the weight is heavy enough to cause the glass beads not to be displaced. Fig 5.1c shows instead the fracturing pattern that can occur when the weight on the glass beads is light enough that the particles are more easily able to be displaced. In this case, the pattern depends on whether or not the hydrodynamic forces that attempt to open the pores dominates over the mechanical forces that attempt to resist the displacement. Therefore, the transition from fingering to fracturing patterns can occur by increasing the injection rate of the invading fluid, or reducing the weight or bead size.

In this chapter, I will describe my experiments with PDMS chips containing pillars on a square or triangular lattice with disorder introduced via random assignment of the pillar radii between a given range. Given that pillars are used instead of beads, a new way of quantifying the competing hydrodynamic and mechanical forces is required to understand which regime the experiments will fall in.

Firstly, the effect of hydrodynamic forces can be understood by looking at the change in capillary entry pressure, from Eq 5.1, due to deformation of the pillars that form the pillar

throat. This change in entry pressure, $\delta P_c$, is the difference between the original required entry pressure, $P_c$, defined by Eq 5.1 and the new entry pressure, $P_{new}$, due to the change in the throat width, $\delta a$, is given by Eq 5.2.

$$P_{new} = \frac{2\gamma\cos(\theta)}{a + \delta a} \tag{5.2}$$

For the system as a whole we can consider the average entry pressure, $\overline{P_c}$, and average throat width, $\overline{a}$, instead:

$$\delta\overline{P} = \overline{P_c} - \overline{P}_{new} = \frac{2\gamma\cos(\theta)}{\overline{a}} - \frac{2\gamma\cos(\theta)}{\overline{a} + \delta\overline{a}} = (2\gamma\cos(\theta))(\frac{1}{\overline{a}} - \frac{1}{\overline{a} + \delta\overline{a}}) \tag{5.3}$$

We will see how we define $\delta\overline{a}$ later in the chapter, in section 5.1.2. What we can now see from Eq 5.3 is that if $\gamma$, $\cos(\theta)$ and $\overline{a}$ are kept constant, as is the case, then the effect of deformation can be quantified and adjusted by varying $\delta\overline{a}$.

What we have shown in Eq 5.1 is there is a required pressure for the invading fluid to enter a pore throat of a given width. However, it is the fluid pressure then deforms the pillars and changes the entry pressure as given by Eq 5.2. The competing force against this deformation is the elastic force related to the size of the pillars. We are able to quantify the way the two competing forces lead to a diversity of entry pressures by looking at how disordered the system is and, in particular, the standard deviation of throat sizes. If all pillars are exactly the same size, then the standard deviation in pore throats will be zero, and thus the variation in capillary entry pressures will also be non-existent. However, if we increase the range of radii that the pillars can be, and therefore the disorder in the system, it follows that the standard deviation in the capillary entry pressures will increase. This gives us a way of quantifying the effect of disorder on the expected deviation, $P*$, on any pore away from its average value:

$$P* = \sigma(P_c) = \sigma(\frac{2\gamma\cos(\theta)}{a}) \tag{5.4}$$

where $\sigma(P_c)$ represents the standard deviation in capillary entry pressures. Like in Eq 5.3, if $\gamma$ and $\cos(\theta)$ are constant, then $P*$ is completely dependent on the various pore throat widths, $a$, and thus the possible range of radii that the pillars can be.

Finally, we can create a dimensionless group by taking the ratio of the two competing effects:

$$\frac{\delta\overline{P}}{P*} = \frac{\overline{P_c} - \overline{P}_{new}}{\sigma(P_c)} = \frac{(2\gamma\cos(\theta))(\frac{1}{\overline{a}} - \frac{1}{\overline{a} + \delta\overline{a}})}{\sigma(\frac{2\gamma\cos(\theta)}{a})} \tag{5.5}$$

Eq 5.5 represents the magnitude of fluctuations in the invasion due to deformation vs the magnitude of fluctuations due to disorder. This gives us a way of determining which effect dominates

how the opening pressures of pores will be in any situation, and is dependent on the amount of deformation possible and the geometry of the system.

In this chapter, I will use Eq 5.5 to explore the various regimes between deformation and disorder to see when fracturing patterns occur and how disorder restricts these patterns. I will implement new experimental techniques to allow for a wide range of deformations and disorders to be explored in the low $Ca$ regime and will analyse these experiments by using image processing techniques. This will be done for two different types of invasion boundary conditions, consisting of when the invading fluid is (i) injected at a constant pressure and (ii) when it is injected at a constant flow rate. This allows for a comparison between the two conditions and shows that the fracturing patterns are strongly enhanced under constant flow rate injection.

## 5.1 Experimental Setup

### 5.1.1 Manufacturing Method

The general manufacturing method is outlined in section 2.1 and I follow the same methods as a basis for the experiments here. Summarised here is the key differences in these methods from Chapter 3 and Chapter 4, building on the manufacturing methodology described in Chapter 2. In particular, these methods allow for making tall pillars, and pillars that hang down without touching the bottom wall of the chip.

MatLab is used to generate the geometry of the porous region for the PDMS chips. Two different lattice configurations were used to accommodate the simulations produced by colleagues for the two different types of injection, constant pressure and constant flow rate. For the constant pressure experiments, circular obstacles are situated on a triangular lattice with a lattice spacing of $a = 150$ µm between obstacles. This is done by creating a row of obstacles which are the required distance apart. The next row is then placed 129.9 µm ($\frac{\sqrt{3}a}{2}$) below the previous row and shifted 75µm ($\frac{a}{2}$) to the right, and so on. The size of the porous region is then decided by manually selecting how many obstacles to have in each row and how many rows to have.

For the constant flow rate experiments, a square lattice is instead used, to be able to compare with simulations. The methodology is almost the same as the triangular designs but instead the rows are not shifted and each row is simply placed 150 µm below the previous row. This creates a square lattice where each obstacle is $a = 150$ µm apart. Again the size of the porous region is manually selected by choosing the number of obstacles per row and the number of rows to make.

Finally, for both set of designs, disorder is added into the system by randomly varying the radii of the obstacles. A uniform case is made by having all obstacles be 40 µm in radii, although

this will be limited by manufacturing errors, estimated as $< 1\%$. The next level of disorder allows the obstacles to be any radii from a uniform range of sizes, between 35 µm to 45 µm. The allows for various sized obstacles but keeps the average radii at 40 µm. The final disorder used was in the range of 30 µm to 50 µm. Disorder in the experiments and simulations are defined by the minimum radii possible in each system, termed $rmin$. Our three disorders used then are referred to as $rmin = 40$, $rmin = 35$ and $rmin = 30$. These give a set of P* = 3.71, 37.8, 78.5, assuming 1% variation in pore sizes for the first case. It can be seen by these range of radii values that for all cases, the average radii will still be 40 µm. However, critically for the manufacturing process, the maximum possible radii is chosen so that obstacles cannot be so close that there is a risk they will merge.

These designs are made into photomasks for the manufacturing process, as described in Chapter 2. Briefly, soft lithography is used as the method for producing molds for the microfluidic chips. As part of the lithography process, SU8 photoresist is spincoated onto a dehydrated silicon wafer to create a uniform layer of photoresist before it is exposed to UV light. Critically to this application, by varying the speed at which the photoresist is spin-coated on a silicon wafer, or the type of SU8 being used, the thickness of the mold can be controlled. Any PDMS chips created from the mold will have pillar heights depending on this thickness. The amount of deformation is then dependent on the height of the pillars, how the pillars are fixed to the base and ceiling of the final chip, and the pressure acting upon the pillars at the fluid-fluid interface. The manufacturing methods will be outlined next.

### 5.1.2 Chips with Pillars Fixed at One End and Two Ends

In an initial proof-of-principle set of experiments, the porous regions contained an array of pillars that were fixed at both ends, similar to the chips used in the previous two chapters. This meant that the pillars would have to be made tall enough such that when the invading fluid is injected into the system, there would be a large enough pressure drop across the interface to cause the pillars to bend in the center. I could then look at how varying the heights of these pillars, and therefore the elasticity of the pillars, would affect invasion patterns. Not only that, but systems with pillars of the same height but different amounts of disorder could be compared to investigate how disorder affects the transition to a fracture-like patterns. To do this, the chips were first filled with water, before air was injected at a constant flow rate of 250 $\mu$L/h using a syringe pump. A camera held above the chips took images throughout the invasion. This was done for a range of pillar heights (50 $\mu$m, 120 $\mu$m, 150 $\mu$m and 190 $\mu$m) and disorders. What these experiments showed was that at low disorders, where disorder is only introduced due to
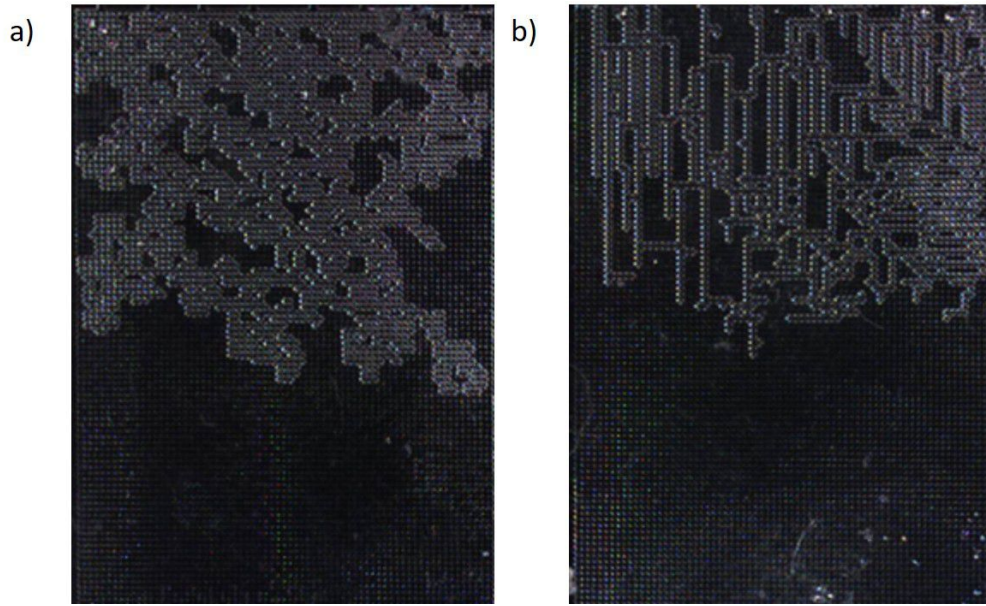
Figure 5.2: Experiments involving invasion into elastic pillars fixed at both ends. Air is injected at constant flow rate of 250 $\mu$L/h with a pillar height of 190 $\mu$m. *a)* Pillar radii range from 30 $\mu$m to 50 $\mu$m. This disorder results in a capillary fingering invasion pattern. *b)* In this case, all pillars have a radii of 40 $\mu$m. Lack of disorder leads to straight fingers, more closely resembling capillary fracturing patterns (see Fig 5.1). Both systems have pillars set on an ordered square lattice.

manufacturing errors, there appeared fracturing-like patterns for pillars with a height of 190 µm, seen in Fig 5.2. This case represents the limit of these experiments, with the tallest (and hence most flexible) pillars, with the least possible natural disorder.

However, it is difficult using this system to see if further increasing the heights of these pillars to make them more elastic would cause the pattern to develop as a fracture-like pattern for the higher disorders. This is because of the limit of how thick the wafer can be coated during manufacturing and thus limits on the height of the resultant PDMS pillars. Above 200 $\mu$m, it was found that because the PDMS pillars were much taller than their diameter ($\approx 80\mu$m), then as the pillars were removed from the master mold, they could be stretched or pulled off, causing irreversible damage to their shape. This becomes more likely the greater the difference between height and width. As the height was limited, another method for exploring a large range of elasticity was developed. To achieve this, a system where the pillars hang over a well rather than be fixed at both ends was used. From looking at Eqs 5.6 and 5.7 [105] which show the maximum possible deflection for both a beam with one fixed end, $\delta a_1$, and one fixed at both ends, $\delta a_2$, it is clear that having a hanging pillar allows for greater deformations:

$$\delta a_1 = \frac{1}{8} \frac{W l^4}{K I} \tag{5.6}$$

$$\delta a_2 = \frac{5}{384} \frac{W l^4}{K I} \tag{5.7}$$

where $W$ is the uniform load on the pillar (force per unit length), $l$ is the length of the beam, $K$ is the modulus of elasticity and $I$ is the moment of inertia. $W$ is a loading force per unit length, and can be related to the maximum capillary pressure in the throat. Roughly speaking, a hanging pillar will deflect about an order of magnitude more than a pillar fixed at both ends.

The first attempts to produce hanging pillars involved using rectangular strips of black electrical tape which were cut such that they were slightly larger than the pillar area and then placed on top of a clear glass slide. The glass slide was then placed in a splutter coater and coated with titanium and gold before the tape was peeled away to leave a makeshift mask for producing the wells. Standard microfabrication techniques are then used to produce rectangular PDMS wells with various depths (8 µm, 10 µm, 20 µm). Both the PDMS well and chips are plasma cleaned for 6 minutes to allow them to adhere to one another. The chips are placed on top of the well, such that the pillars hang over the well, which was then placed on top of a glass slide. The depths of the wells are such that the average pore throat width is always greater than the distance between the bottom of the pillars and the bottom of the well. This means that flow between the pillars is still more favourable to flow underneath the pillars.

Demonstrated in Fig 5.3 is that the pillar deformation is now significant for pillar heights of only 150 $\mu$m when they are injected with air. Shown here is a difference image of a sample of pillars before and after pore invasion as a result of fluid injection at a constant flow rate of 250$\mu$L/h. What is important to notice here is the bright areas around the pillars, which represents a shift in position of a portion of the pillars after the invading fluid has entered the corresponding pores. What this means for the experiments is that a higher effective elasticity, or amount the pillars can bend, is achievable for the range of heights that can be produced from this manufacturing method than what could be achieved for the same range of pillar height when fixed at both ends.

After these experiments were first undertaken, the method for producing hanging pillars was adjusted. While having a shallow well was necessary to ensure that the invading fluid didn't flow underneath the pillars, the pillars would still often stick to the bottom of the well while the glass slide and chip were being adhered to each other. It was found to be more reliable to instead coat a glass slide with PDMS of thickness 10µm and carefully cut out a rectangular slice from the slide. Only the glass slide was then plasma cleaned meaning that because the pillars themselves

Figure 5.3: Difference image from before and after invasion for hanging pillars with air injected at a constant flow rate of 250 $\mu$L/h and a pillar height of 150 $\mu$m. Bright areas surrounding each pillar, and not connected to the menisci, indicate deformation of pillars produced by the injection of an immiscible fluid, and the forces arising from the internal tension.

were not subjected to plasma cleaning and as such would not stick to the glass bottom of the well. This method was used for the remainder of experiments in this chapter.

## 5.2   Constant Pressure Experiments

The preliminary experiments shown in section 5.1.2 were conducted using constant flow-rate injection via a computer-operated syringe pump. However, some simulations being performed alongside these experiments relied on injection being performed at a constant injection pressure. As such, the experiments were adjusted to instead use fluid injection via constant pressure using the setup shown in Figure 5.4.

The aim when designing a constant pressure experiments is to have most of the pressure drop in the injection phase of the experiment. To this end, the properties of the fluid and tubing is to produce a volumetric flow rate comparable to what can be achieved by the syringe pumps. To achieve a pressure drop of   10,000 Pa, a reservoir is placed at a height h = 1 m below the chips. Given that $P = \rho g h$ and $\rho \approx 1000 kg/m^3$ for a water/glycerol mixture, this generates a pressure drop of about 10,000 Pa.

The pressure loss in a cylindrical pipe of a given length and can be written using the Darcy-
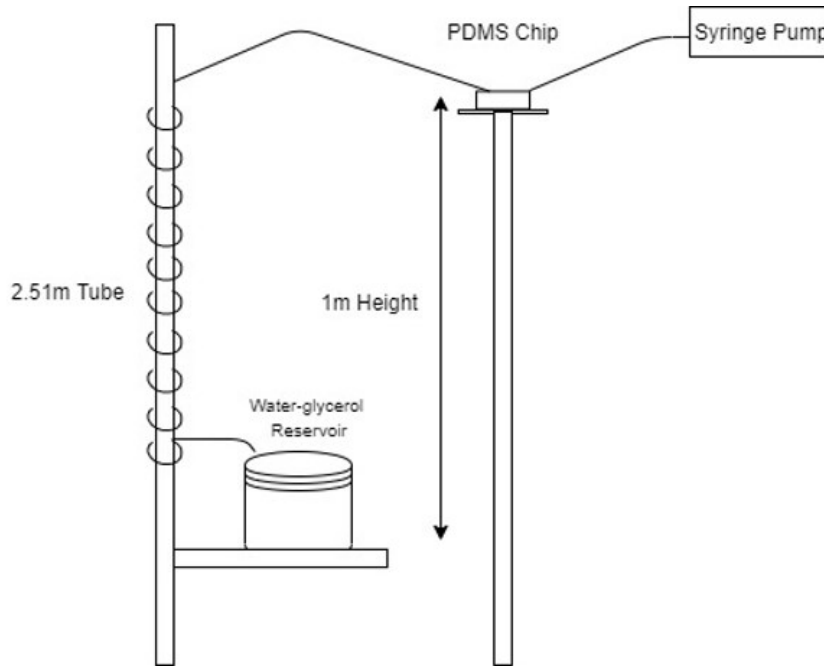
Figure 5.4: Diagram depicting the experimental setup used to produce air invasion at a constant pressure of 10 kPa.

Weisbach equation [106] in the form:

$$\frac{\Delta P}{L} = \frac{128}{\pi} \cdot \frac{\mu Q}{D_c^4} \tag{5.8}$$

where $\frac{\Delta P}{L}$ is the pressure loss per unit length, $\mu$ is the dynamic viscosity of the fluid, $Q$ is the volumetric flow rate and $D_c$ is the diameter of the cylindrical tube. The diameter, $D_c$, of the PTFE tubing used was 0.3 mm and the viscosity of the water/glycerol mixture used was 0.019 Pa·s, measured using a DHR rheometer. To achieve a volumetric flow rate Q ≈ 150 µL/h given these values, Eq 5.8 can be rearranged to find that the tube length required is 2.51m. This setup is used to achieve constant pressure experiments, comparable to the boundary conditions designed into the matching numerical simulations performed by Enrico Segre and Ran Holtzman, see section 5.2.1.

For the experiments, a syringe pump first injected either oil or a water-glycerol mixture backwards through the PDMS chip and down the length of the PTFE tubing into a reservoir of the mixture. The choice of either oil or a water-glycerol mixture as the defending fluid was varied to explore the effect of viscosity on the invasion patterns. The syringe is left attached to the injection tubing until all air bubbles inside the PDMS chip disappear via diffusion. The syringe is then removed from the tubing and air invades at a constant pressure as the fluid is siphoned off

into the reservoir. This pressure was varied to investigate if different pressure drops would first create fracturing patterns and then see if higher pressures would sustain these patterns at higher disorders. These pressures ranged from 2,000 Pa to 10,000 Pa. This allows the experiments to be directly comparable to the simulations.

### 5.2.1 Numerical Method

The simulations produced by colleague Enrico Segre and Ran Holtzman use the same geometry as the experiments, and are based on the methods documented further in the thesis of Oshri Borgman [107]. The coordinates previously generated to create the photomasks are used as the basis for setting up a pore-network model. The simulations are supplied with initial parameters, such as elasticity of each pillar, here encoded as a spring constant, the surface tension and the pore throats where the interface between the invading and defending fluid first exists. Both capillary pressure and viscous pressure are included in the model. This involves using two modelling approaches, grain-based which looks at meniscus stability from pore geometry, and pore-based which resolves fluid pressure from the pore topology and geometry.

For each time step of the invasion process, the following steps take place. The position of the invasion front is located, given the filling status of each pore, this ranging from 1 for invaded and 0 for non-invaded pores. The fluid pressure in each pore is evaluated and used to calculate the new pore throat width. There is then a check for new meniscus instabilities and the flow network is updated accordingly. Finally, the filled status of each invaded pore is updated in a manner consistent with the model described in Chapter 3. The simulations are stopped when any pore in the outer boundary is invaded.

### 5.2.2 Results

The constant pressure experiments showed there existed some effect of elasticity on the resulting invasion patterns, as shown in Fig 5.5. What is seen there is that for the shorter pillars, the invading fluid does not cause significant deformation of the pillars. In Fig 5.5(a), all pillars have a radius of 40 µm, where disorder only occurs due to manufacturing uncertainty. Because there is no direct route out of the porous region for the invading fluid, the majority of the pores are invaded en route to exiting the porous region and the fluid invades with a relatively compact front. However, this is not the case for pillars more than double the height of these pillars, seen in Fig 5.5(b). In this case, more significant deformation of the pillars occurs, up to 9.5 $\mu$m for heights of 130 $\mu$m compared to only 0.4 $\mu$m for heights of 60 $\mu$m, due to the pressure drop across the fluid interface and this difference creates fracture-like patterns. Here, thin long fingers extend

into the porous medium with shorter thin fingers branching off.
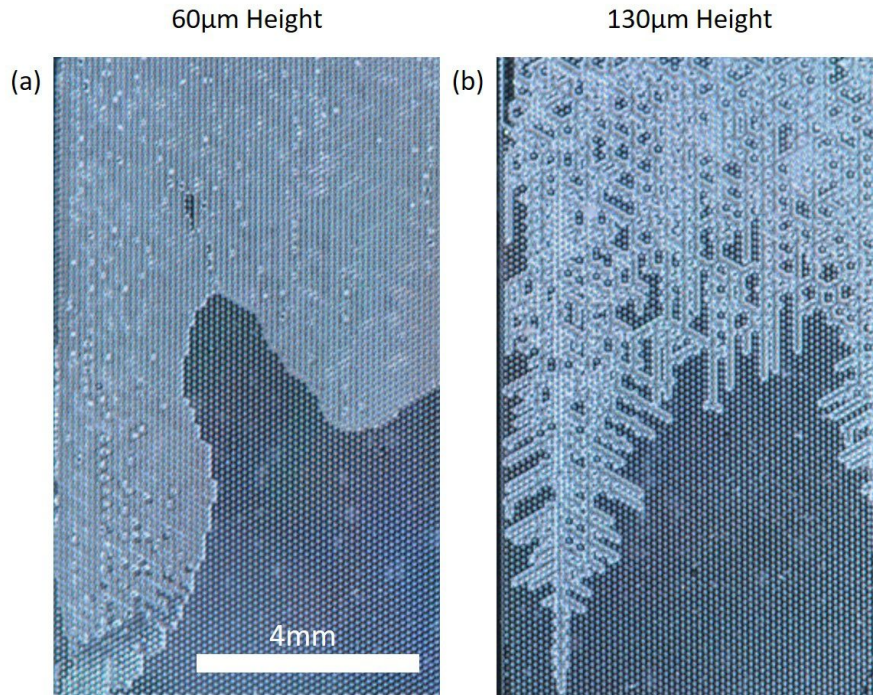


Figure 5.5: Experiments ran at a constant pressure of 4,000 Pa with air invading into an oil-saturated medium where pillars are all 40 µm in radii. (a) Pillars 60 µm in height. Fluid invades the majority of pores along a compact front as pore throat widths aren't affected by invading fluid and therefore all pores are equally preferred for invasion. (b) Pillars 130 µm in height. Thin fingers appear from which shorter fingers branch off of. These taller pillars are more readily deformed by invading fluid and create a cascading path for the invading fluid to follow.

Although promising, the issue that commonly occurred with these experiments was that the invading fluid often invaded underneath the hanging pillars, with some examples of this issue shown in Fig 5.6. In Fig 5.6(a), we see how a fluid that totally invades underneath the pillars looks. It is noticeably a different colour to when the fluid invades between the pillars. Because the fluid invades underneath, the defending fluid is still trapped above and in between the pillars, causing the different shading. This was a very common effect and was in some cases combined with the expected invasions of the pillar layer. For example, in Fig 5.6(b), the invading fluid invades between the pillars in some areas, but is also met by areas where the fluid invades underneath. This flow underneath will have a significant effect on the path that the invading fluid takes and therefore these experiments cannot be used to investigate invasion patterns.

Given the common occurrence of these issues, these experiments were not conclusive enough to provide results from which to further quantitatively analyse and understand the invasion
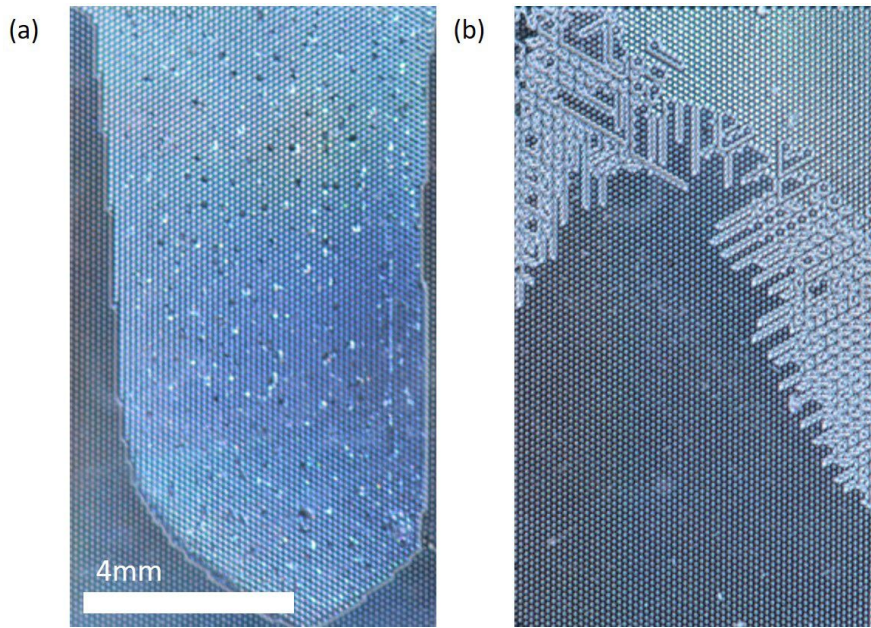
Figure 5.6: Common issues that arose with the constant pressure experiments. a) Invading air can flow underneath the pillars rather than through them. This effect is noticeable by a distinct shading of the invaded area. b) Air invades partially underneath and partially in between the pillars. In this case, any flow underneath will advance invading air into areas it might not have normally entered.

patterns for a constant pressure injection. There were some conditions for which the experiments produced invasion patterns that could be compared to the numerical simulations, such as the two experiments shown in Fig 5.5. These mostly occurred for when P = 4 kPa for $rmin = 35$ and $rmin = 40$, along with some results at various combinations of P and $rmin$. However, thanks to simulations ran by colleagues Enrico Segre and Ran Holtzman, we are able to still investigate what theoretically should be the case for constant pressure injections in the same system as was used in the experiments.

Numerical simulations were run investigating a wide range of elasticities (pillar heights), injection pressures and disorders ($rmin$). Shown in Figure 5.7 is a range of these simulations at a particular injection pressure, 10 kPa, that is similar to the pressures achieved in the experiments. The pillar's elasticity is shown on the y-axis and is represented by $K$ (the modulus of elasticity), with completely rigid on the top row, and disorder is shown on the x-axis. The cases that match those in the experiments are for $K = 1.5$ MPa

For a constant pressure of 10 kPa, patterns emerges for the higher disorders which are somewhat similar to those seen in Fig 5.5(b), in that there exists a leading finger with smaller fingers branching off a short distance. However, consistently for $rmin = 40$ the majority of the chip is

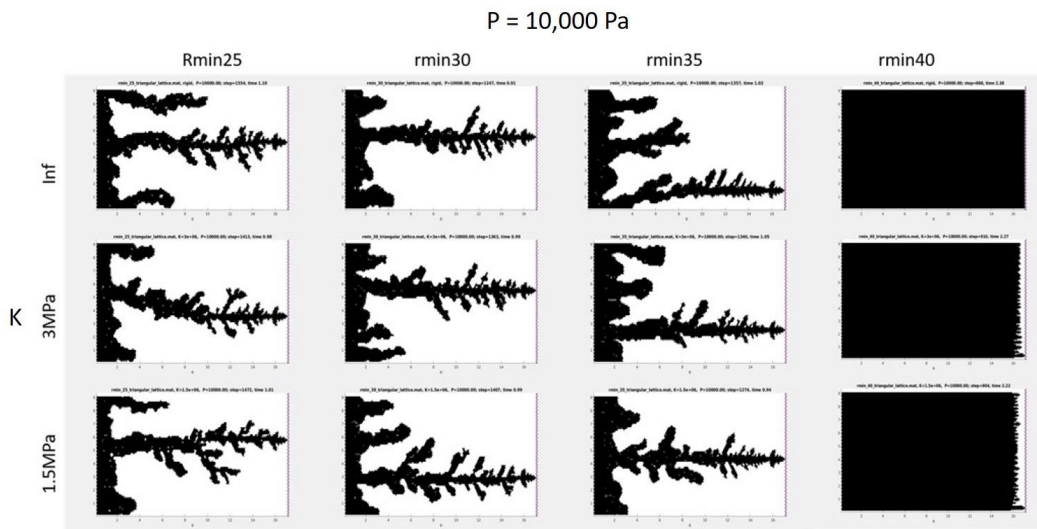Figure 5.7: Elastic simulations of air invasion at a constant pressure of 10 kPa. Elastic modulus, K, and disorder, *rmin*, are varied.

invaded before breakthrough. This is because, unlike in the experiments, there are no manufacturing errors in the pillar sizes and thus every pillar is the exact same size. The air therefore invades every pore as it progresses through the chip forming a compact front invasion pattern. For the simulations with disorder, some patterns appear, typically with one major finger that takes over and propagates that length of the chip. While this looks like some kind of branching and fracturing pattern, a similar pattern appears when $K = \text{Inf}$ ($K$ taken as infinite), where the pillars are completely rigid. As the system is rigid, the patterns must be due to the geometry of the system and the disorder in pore throat widths along with any numerical noise, rather than any kind of deformation that might be opening up the pore throats.

The simulations were also ran at different pressures to check if there existed any patterns that could be linked to fracturing when a high enough pressure was used. Interestingly, for $P = 30$ kPa, there existed a regime that could be attributed to fracturing, see Fig 5.8. Here, we see a fracture-like pattern for $K= 1.5$ MPa and $rmin = 40$. Previously, for $P = 10$ kPa in Fig 5.7, no pattern was seen for $rmin = 40$ systems as there existed no preferential pathways due to the opening of pore throats. However, when $P = 30$ kPa, there now exists an invasion pattern than has a main fracture line with shorter fingers branching off, and which changes significantly as the system's elastic response is varied.

To explore the low very low disorder regime, new simulations were ran with disorders of $rmin = 38$, $rmin = 39$ and $rmin = 39.5$. I designed the geometries used for these simulations using the methodology described in section 5.1.1 and chose radii that was similar to what the
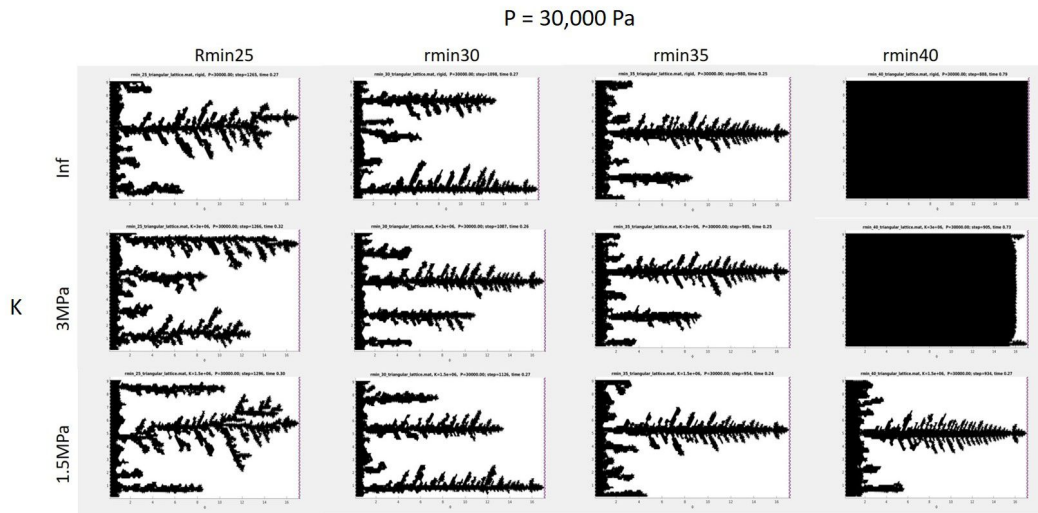
Figure 5.8: Elastic simulations of air invasion at a constant pressure of 30,000 Pa. The elastic modulus, $K$, and disorder, $rmin$, are varied.

radii of the experimental $rmin = 40$ systems would be, due to the manufacturing tolerances. A pressure of $P = 10$ kPa was used so that we could investigate if indeed the level of disorder at $rmin = 35$ was too large for the pressure at 10 kPa to allow fracture patterns to appear. Not only that, but a larger range of $K$ was used to see if making the system extremely elastic would make a difference. Similar to the patterns produced in Fig 5.7, the systems with disorder $rmin = 38$ and $rmin = 39$ showed that making the system totally rigid did not affect the invasion patterns. However, for $rmin = 39.5$ at $K < 1.5$ MPa, there appeared invasion patterns that would disappear with increasing values of $K$, leading to a purely compact front advancing when $K$ was infinite. However, an interesting feature of these patterns is that the large fracture that can sometimes be seen protrudes later from the uniform invading front at $K = 0.5$ MPa than at $K = 1$ MPa. This is not expected, as for a more elastic system, the fracture pattern would likely occur sooner given how easy it would be to deform the pillars and create a fracture.

However, the disorders used in these simulations are too low to be reproducible in experiments where there was a manufacturing tolerance of about 1% during the production of the pillars, which is larger than the range of radii in the simulations. Therefore, the resulting patterns are not quantitatively compared to one another and are instead used here to give an indication of what patterns should theoretically occur, and in what regime, for fluid invasion at constant pressure. We find that there exists some resemblance of a fracturing pattern when $P = 30$ kPa, $K = 1.5$ MPa and $rmin = 40$, but this is such a narrow set of parameters, and where issues of numerical noise may be relevant, that a new experimental and numerical method for investigating an elastic porous medium was needed.
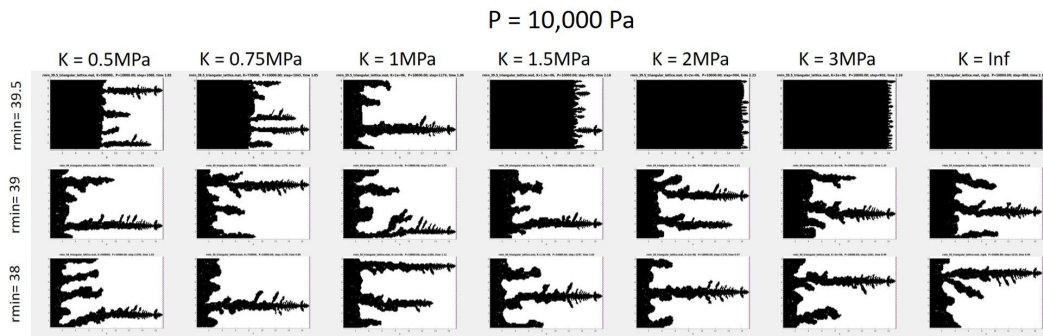
Figure 5.9: Elastic simulations of air invasion at a constant pressure of 10 kPa, focusing on very low disorders. Elastic modulus, $K$, and disorder, $rmin$, are varied.

## 5.3 Constant Flow Rate Experiments

In order to explore the effects of the injection boundary conditions on invasion patterns a new injection method was now used, in the form of a constant flow rate. Here, a syringe pump is used to inject the fluid into the chip at a constant rate by controlling the speed of the syringe pump via a computer. The chips are again housed in a darkened box with a low-angled light below the chips to illuminate the interface between the two fluids. A camera is placed above the chips to image the invasion of the fluid over time. The syringe pump and computer are kept outside the darkened box to allow control of the pump and camera during the experiments.

Initially, the same geometry as for the constant pressure experiments was used. This consisted of pillars on a triangular lattice with disorder introduced by randomly varying the radii of the pillars between a set range, keeping the average radii of all the pillars at 40 µm. Air was injected into the water-saturated systems at a rate of 469 µL/h, which corresponds to $Pe \approx 21$ and $Ca \approx 4 \times 10^{-5}$. These experiments produced some patterns of interest, particularly when experiments with pillars of different heights are compared for $rmin = 40$ systems. Seen in Fig 5.10(a), for short pillars of height 65 µm the invading fluid explores most of the initial porous region, advancing in a compact front, before flowing down one side of the region. Note that this asymmetry of one side of the chip being favoured over the other was a common occurrence with this set of experiments and could be due to potential defect in the chips. Fig 5.10(b) shows the effect of increasing the pillar heights to 130 µm. At this height, the pillars are more easily deformed and thin fingers invade in a straight line down the length of the porous region. This invasion pattern invades much less area compared to in Fig 5.10(a) for the same geometry, which is one way of defining fracturing patterns.

However, as with the constant pressure experiments, the majority of these experiments experienced issues with the invading air flowing underneath the pillars. To address this, the defending
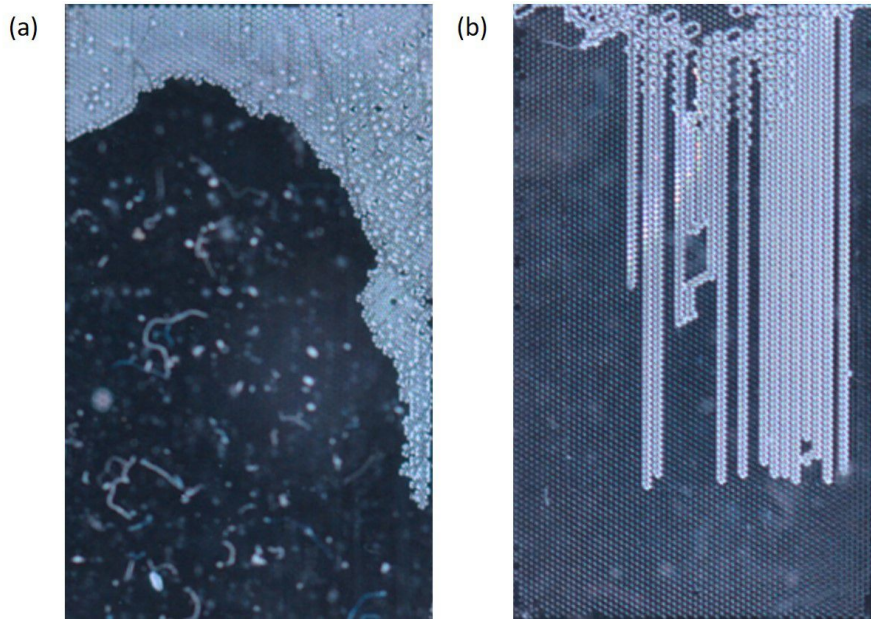
Figure 5.10: Air injected into water saturated chip at a constant flow rate of 469 µL/h. (a) For pillars with a height of 65 µm, fluid invades a large area as a compact front before flowing down one side of the porous region. (b) In contrast, for pillars with a height of 130 µm, long thin fingers invade into the porous region, with less area being invaded in comparison to shorter, more rigid pillars.

fluid was changed from water to a refractive index oil. The choice of oil was also such that refractive index of the oil would highlight the interface between the two fluids and was viscous enough to stop air easily flowing underneath the pillars. The viscosity of the oil is 0.01 Pa·s and has a high refractive index, $n_D = 1.6320$ [108]. Along with substituting the defending fluid, the injection speed was reduced to 188 µL/h, corresponding to $Pe \approx 8.4$, to try and improve the issues that were occurring.

These experiments produced a range of invasion patterns that allowed for comparison between different elasticities and disorders. Shown in Fig 5.11 is a sample of these experiments. Similar to the previous experiments, at a height of 65 µm and a low disorder of $rmin = 40$, the air invades into the porous region and explores the majority of the pores in a compact front, as shown in Fig 5.11(a). However, when the pillar height is increased to 130 µm, the fluid invades a large amount of the porous region but thin fingers interconnect with one another as the pores are invaded, leaving many islands of defending fluid trapped behind the front. These fingers are then restricted in width for chips at the same height when disorder is increased to $rmin = 35$ µm, as seen in Fig 5.11(c). With pillars now having a radius randomly assigned between 35µm and 45µm, the pattern now resembles a capillary fingering pattern, with a large amount of pores
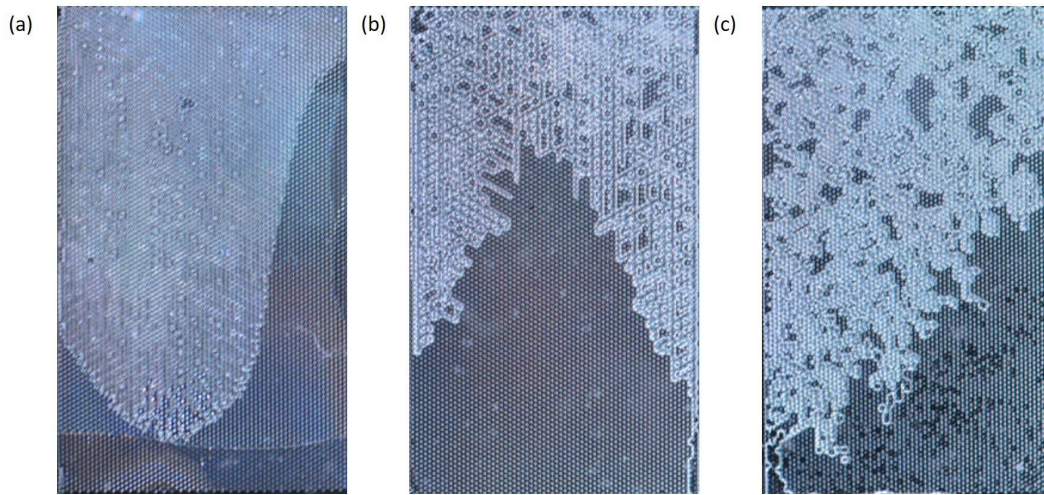
Figure 5.11: Air injected into oil saturated chip at a constant flow rate of 188 µL/h. (a) For pillars with a height of 65 µm, the invading air explores most of the porous region as the pillars do not deform. (b) For pillars with a height of 130 µm at $rmin = 40$, numerous thin fingers appear. This pattern shows fracture-like invasion with straight fractures branching off from each other. (c) For pillars with a height of 130 µm at $rmin = 35$, the disorder introduced now causes the thin fingers to be distorted into a dendritic pattern with many trapped areas.

invaded but trapped clusters of defending fluid being left behind the flow front.

These patterns indicate that the experiments are being performed in the region of phase space where a transition occurs from dendritic invasion to fracturing, as the pillar height is increased, and that a small introduction of disorder will restrict this fracturing. However, for the triangular lattice chips, manufacturing issues meant that further heights were unable to be explored. In the interest of time, the decision was made to return to the square lattice chips previously shown for the preliminary experiments in Fig 5.2. Using this square lattice geometry, chips with heights of 50 µm, 120 µm, 150 µm and 190 µm were made. This allowed for the possibility of exploring the transition region from non-fracturing to fracturing patterns, and to see if tall enough pillars would continue to show fracturing patterns for different disorders. This was accompanied by simulations done by Soumyajyoti Biswas for comparison, based on constant flow rate invasion in the low $Pe$ limit. This will be summarised in Section 5.3.2, after a brief digression here about image analysis.

## 5.3.1 Image Analysis Process

The images taken during the experiments were processed using MatLab. The following method was used to attempt to identify which pores were invaded, so that quantitative measures could

be extracted for comparing experimental regimes of pattern formation.

Only the final image in each sequence, just after breakthrough, was processed so as to analyse the final invasion pattern when the invading air first exits the porous region. The first image in the sequence, just before the air invades into the porous region, is also used for image subtraction later in the image analysis process. In the code I wrote for this purpose, the user selects the top left and top right pillar of the porous region which allows the code to then rotate and crop the image around the porous area, as is the case for Fig 5.12a). The coordinates and radii of the pillars, used originally to generate the photomasks, is then loaded in and scaled to fit the cropped area. A difference image between the final and first image in the sequence is taken to highlight the invaded areas, shown in Fig 5.12b). A Gaussian filter with a width of 4 pixels is applied to the image. A common issue with the invaded areas is the interface between the invading and defending fluid is clear and bright but the center of the invaded pores is dark, and therefore thresholding does not produce a useful result. To try and address this, the intensity in the center of pore throats is measured using the as-designed coordinates of each pillar. This is done for every pore throat in the system and where the intensity in a pore throat meets a certain threshold that pore throat is marked, a sample of this shown in Fig 5.12c). Then to determine if a pore is filled, the code looks at if the pore throat directly opposite is also marked. If both pore throats are marked as filled, then the pore between the two throats is also classed as filled and a square with dimensions the same as the scaled pore is added to the pore for further analysis purposes. A final image then creates a reduced image, which has a single pixel corresponding to if a pore is filled, seen by 5.12d).

However, there are a couple of issues that arise from this method. The area that is chosen to be the center of the pore throat for the intensity measurements involves the manual selection of the top left and top right pillars by the user. This can lead in some cases to the intensity being measured close to the pillars rather than the center of the throat if the selections are not exactly aligned. In this case, the intensity will be lower than it should be and the throat will be marked as not filled. This eventually leads on to pores also not being classed as filled and gaps appearing in the invasion pattern.

Another common issue is that, due to noise in the images, sometimes caused by slight camera movements between the first and final image in the sequence, there were areas that were classed as filled pores which clearly weren't and vice versa, with areas that should be filled being classed as empty. This created final images were unable to be analysed.

Finally, if there were areas with alternating lanes that were filled and unfilled, the methodology used to find filled pores would fill lanes that hadn't been invaded. This is because the adjacent lanes that had been invaded would both have pore throats with a high enough intensity
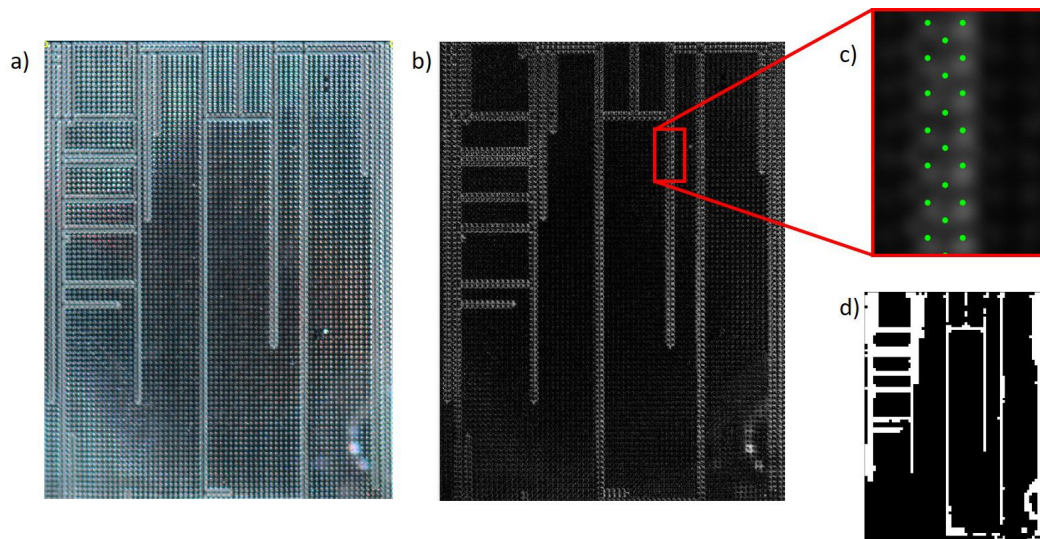
Figure 5.12: Workflow of analysis for experimental images. a) The final image in each sequence is rotated and cropped. b) A difference image is calculated between the final and first image in each sequence. c) The intensity is then measured in each pore throat. Throats that meet a cutoff intensity are marked (here with green pixels). d) If opposite pore throats are both marked, then the pore between throats said to be filled. The reduced image here shows each pore as a pixel either filled (white) or empty (black).

value. Therefore, for the lane between these two invaded lanes, the pore throats either side of it were also classed as filled, and therefore the pores that make up the lane would be incorrectly filled. This was an issue for the more elastic systems, where straight lines of invasion were common, and made analysis of these images impossible. These issues meant that the intended quantitative analysis of the experimental images was unable to be satisfactorily completed and instead only a qualitative analysis of the images will be used for the rest of the chapter.

However, a metric had already been designated for analysis and was measured in the numerical results explained in the following section. This metric was a measure of how ordered, or "straight", the resulting invasion patterns were. To do this, every pore that had exactly 2 neighbouring pores are identified. The code would then identify the position of these two neighbouring pores in relation to the pore of interest. If the 3 pores made a corner L-shape, or a symmetric equivalent, then the pore of interest was given a value of $-\frac{1}{2}$. If the 3 pores made either a vertical or horizontal straight line, it would be given a value of 1. The reason for these values is that there is 4 possible configurations of L-shapes to 2 configurations of straight lines for the 3 pores. This is then normalised by the number of ordered and disordered pores that exist. Written as an equation, where $p$ is the number of ordered straight pores, and $n$ is the number of disordered corner pores, then the order parameter, $\Omega$, can be written as:

$$\Omega = \frac{p - \frac{n}{2}}{p + n} \tag{5.9}$$

For a crack-like invasion of straight segments, $\Omega$ will approach one, but for a random invasion pattern, it should be close to zero.

### 5.3.2   Numerical Method

The simulations run by Soumyajyoti Biswas use the same geometry as the experiments and are based on methods reported in [75]. The simulations also consider a square lattice where each lattice site represents an elastic pillar. Each pore, that is the space between four adjacent pillars, is initially filled with a liquid that dries from one side due to air invasion, essentially simulating fluid invasion at vanishingly small $Pe$. Invasion pressures are decided by the radii of the pillars, which are assumed to have a random but uniform fluctuation around an average value. This fluctuation is sampled from the uniform distribution (-d,d), where $d$ characterises the strength of the disorder.

Under these conditions, air invasion is simulated from one side of the lattice for different values of disorder. The simulations define a Monte Carlo time step as one sweep of the lattice (one update attempt per pore). The simulations then look at first passage times and define it as the time at which any pore at a given distance from the start of the invasion line is first invaded.

### 5.3.3   Results

Shown in Fig 5.13 are some of the resulting invasion patterns from the experiments. These images are ordered with increasing $\frac{\delta\overline{P}}{P_*}$ derived from Eq 5.5. To calculate values of $\frac{\delta\overline{P}}{P_*}$, a measurement of the curvature of the fluid-fluid interface is taken to calculate the pressure drop across the interface that acts upon the pillars. Along with the standard deviation of the pore throat sizes, calculated using the as-designed coordinates of each pillar, a value for $\frac{\delta\overline{P}}{P_*}$ can be calculated using Eqs 5.5 and 5.6. Errors associated with the values for $\frac{\delta\overline{P}}{P_*}$ arise from manufacturing errors when producing pillars heights and diameters, see section 5.1.1. The images are arranged such that the top four images are when $\frac{\delta\overline{P}}{P_*} < 1$ and therefore disorder is the dominating feature of the system, and the bottom four images are when $\frac{\delta\overline{P}}{P_*} > 1$ and the elasticity of the pillars is the dominating feature.

Looking at the images for when $\frac{\delta\overline{P}}{P_*} < 1$, we see that the invasion patterns resemble capillary fingering patterns, where the geometry of the system is what decides where the fluid invades and the amount of trapped defending fluid that remains after the invading fluid exits the porous region. As we increase $\frac{\delta\overline{P}}{P_*}$ to around 1, we start to see signs that elasticity is having an impact
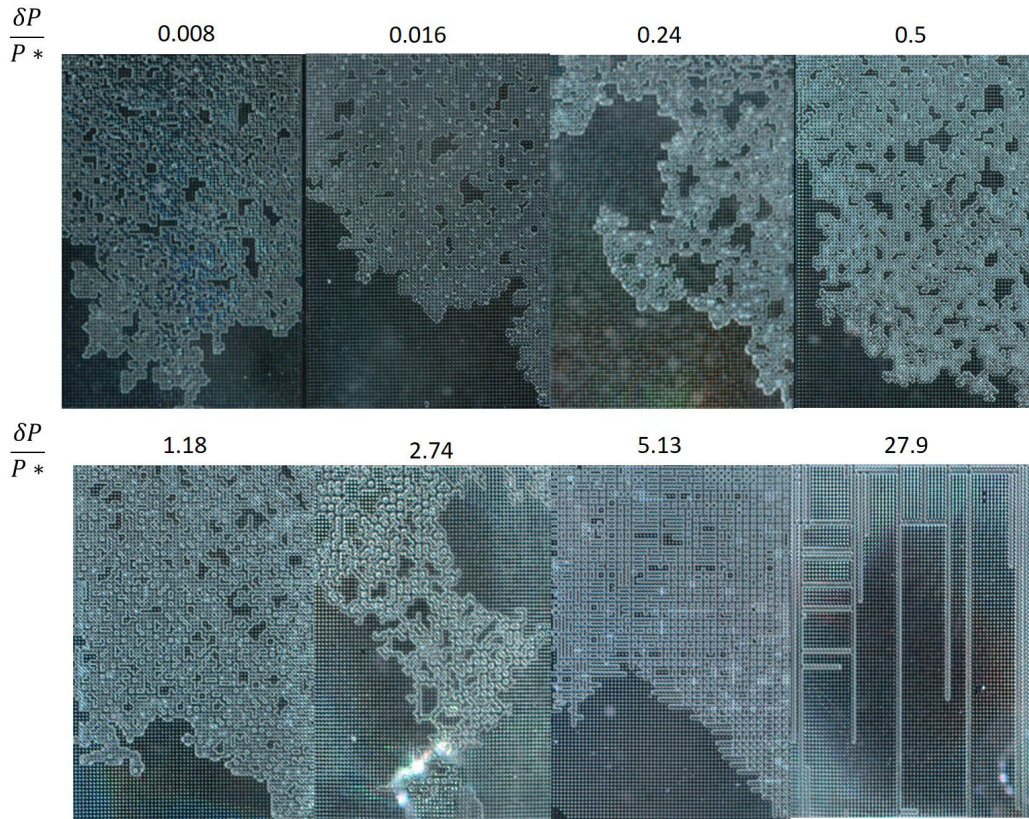
Figure 5.13: Experimental images of air invading into oil-saturated system with increasing $\frac{\delta \overline{P}}{P_*}$. At $\frac{\delta \overline{P}}{P_*} < 1$, the invading fluid follows a path set predominantly by the disorder in the system. For $\frac{\delta \overline{P}}{P_*} > 1$, the pillars begin to deform as air invades and the elasticity of the pillars dominates over the disorder in pillar sizes.

on the invasion pattern. Comparing $\frac{\delta \overline{P}}{P_*} = 1.18$ to $\frac{\delta \overline{P}}{P_*} = 0.5$, while the pattern still doesn't quite resemble a fracturing pattern, there now exist multiple sites where defending fluid is trapped within a single pore. Within the invading fluid, there can be seen to be thin fingers that together make up the bulk of the invaded area. This is made even clearer as we move up to $\frac{\delta \overline{P}}{P_*} = 2.74$, highlighted by a time series of images in Fig 5.14. Here, it is clear that short, thin fingers make up the invading pattern, but that disorder still causes these fingers to change direction frequently. What can be difficult to see in this image is that pores adjacent to those invaded are left with trapped defending fluid. This is due to the constriction of these pores as the pillars that make up the pore throats are bent inwards, causing invading fluid to flow around rather than through these pore throats. The case for $\frac{\delta \overline{P}}{P_*} = 5.13$ shows how these thin fingers extend further as disorder has even less of an effect on the flow and therefore doesn't divert each finger from its straight path as regularly, as seen in a time series in Fig 5.15. Again, lanes adjacent to those invaded are left with trapped defending fluid as pore throats are restricted due to the increased

Figure 5.14: Experimental images of air invading into oil-saturated system at $\frac{\delta \overline{P}}{P*} = 2.74$. Images taken as invasion proceeds, from left to right.

bending of pillars.

Finally, when $\frac{\delta \overline{P}}{P*} \gg 1$, as is the case for $\frac{\delta \overline{P}}{P*} = 27.9$, the disorder has such a little effect on the flow that one pore wide fingers extend down the length of the porous region. This creates an avalanche effect as the pillars at the tip of the invading finger open up, and therefore preferential flow is generally in the same direction as initial invasion. In this regime, the saturation at breakthrough is much lower than for previous invasion patterns, and there exist areas of large trapped fluid. As less of the porous region is invaded, when the invading fingers deviate and link together with other invading fingers, it creates the large rectangular areas of trapped fluid.

While I wasn't able to use image analysis to quantitatively compare results from experiments and simulations, we can compare the displacement patterns qualitatively and look at metrics that were gathered from the simulations to better understand the effect that elasticity has on fluid flow in porous media. As described in Sec 5.3.2, disorder is introduced into the numerical system by adding a random value from a uniform distribution, *(-d,d)*, to the required entry pressure of each pore throat, mean value of 643 Pa. The corresponding d-values for the experiments at *rmin*
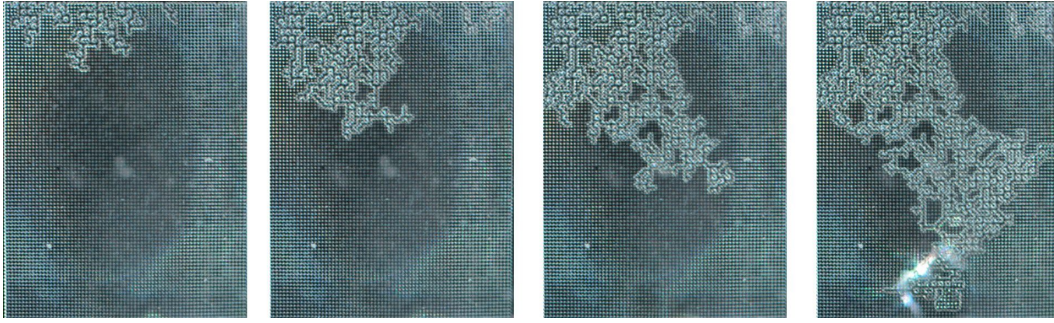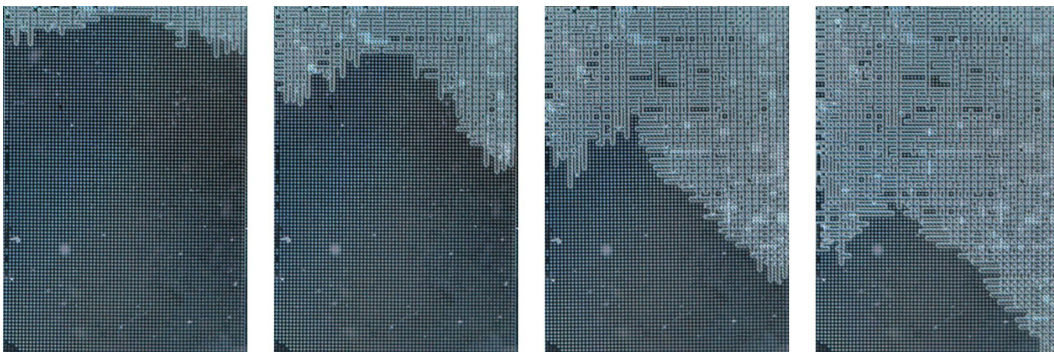


Figure 5.15: Experimental images of air invading into oil-saturated system at $\frac{\delta \overline{P}}{P*} = 5.13$. Images taken as invasion proceeds, from left to right.
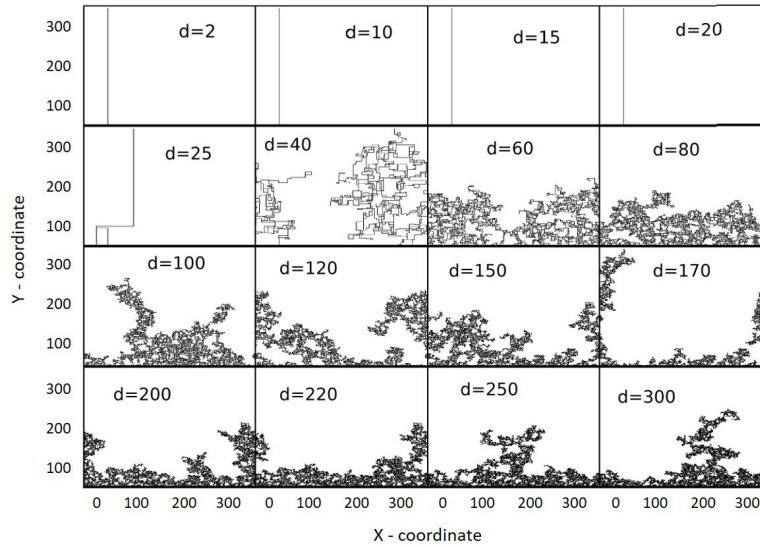
Figure 5.16: Fluid invasion patterns for a constant flow rate invasion produced by simulations done by Soumyajyoti Biswas. Here, d represents disorder by the maximum amount the average capillary entry pressure can be randomly changed from. The X and Y coordinates indicate the positions of the pores in the simulation.

$= 40$, 35 and 30 are, respectively $d = 9.05$, 80.3 and 143. These are calculated from how much the capillary entry pressures change from a completely ordered system, where all pore throats are the same size, to the largest possible pore throat based on the minimum possible radii of two pillars in each system. The resulting patterns from the simulations are shown in Fig 5.16. At low disorder, for d $\leq$ 20, the invading fluid is not perturbed by the disorder at all and a singular crack-like finger invades through the porous region. For slightly increased disorder, when d $=$ 25, there is some slight disturbance in this finger as the fluid changes direction a small number of times before eventually cascading down a singular lane similar to the lower disorder systems. For increasingly higher disorders, starting at d $=$ 40, the disorder now starts to more frequently alter the direction in which the fingers invade. This still leads to thin fingers but these take longer to exit the system and explore more of the pores before exiting. At the highest disorders, d $\geq$ 80, the invasion patterns now look less like they are made of thin fingers and instead resemble capillary fingering patterns, where a large majority of pores are explored and disorder dominates the flow of the invading fluid over the elasticity of the pillars.

As described in Eq 5.9, the invasion pattern can be described by an order parameter, $\Omega$, with values between 0 and 1, with a value of 0 being an invasion that consists of randomly varying invasion patterns, with a finger equally likely to advance in any direction and a value of 1 being an invasion pattern that consists of a singular straight line. These values are measured from the
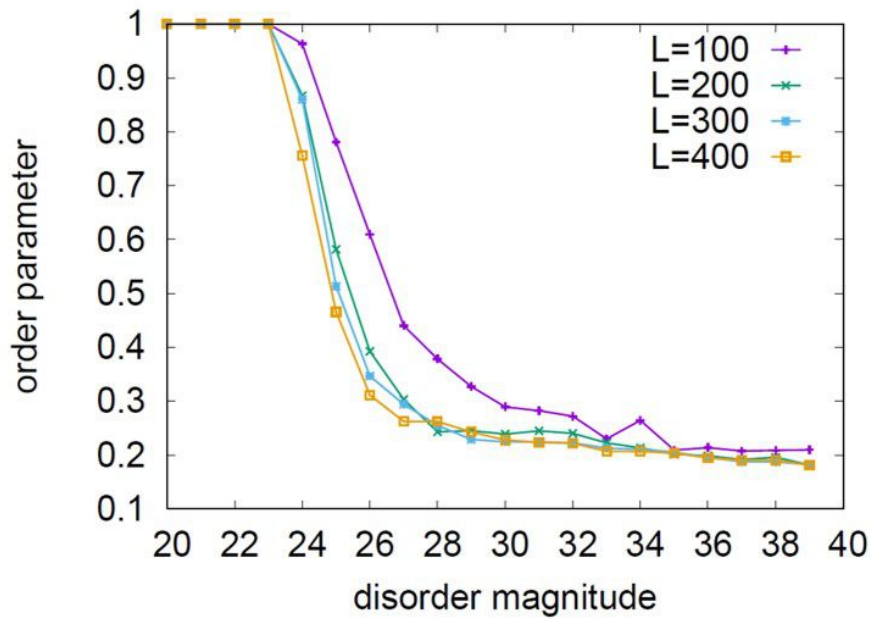
Figure 5.17: Order parameter, $\Omega$, as measured from invasion patterns produced in the simulations by Soumyajyoti Biswas. For values of $\Omega = 1$, the patterns consist of a straight line. For values of $\Omega = 0$, there exists no straight lines and all pores are explored. The graph highlights the disorder range at which the patterns transition from completely ordered to disordered. Here, L represents the system size, which is an LxL block of pores.

displacement patterns at disorders between 20 and 40 and the results are shown by the graph in Fig 5.17. The graph highlights the disorders at which the invasion patterns transition from completely ordered values of 1. The order parameter first starts to drop at d = 24 as disorder changes the direction of the main invading finger. The order parameter then drops off quickly with increasing disorder as small increases in disorder have a larger effect on the invasion pattern and the invasion is forced to explore more pores by the disordered geometry of the system. The order parameter then starts to plateau at a constant lower value for d > 27. At these disorders, the invading fingers already now explore a large amount of the porous region and therefore increasing the disorder has no significant effect of the how ordered the patterns are.

## 5.4 Discussion and Conclusions

Shown in this chapter is that fracturing patterns appear for fluid invasion into highly ordered porous media. This occurs when the elasticity of the pillars that form the porous medium is large enough that an elastic response dominates the flow of the invading fluid over the disorder in the system. These fracture-like patterns can be characterized by thin fingers which extend

linearly into the porous region and where invasion restricts further flow into adjacent pores and lanes by the bending of the pillars and the constriction of pore throats. These patterns can be seen by the experiments in Fig 5.13 when $\frac{\delta \overline{P}}{P_*}$, which is the ratio of elasticity to disorder in the pillars, is greater than 2, and that the fractures become more prominent as $\frac{\delta \overline{P}}{P_*}$ increases.

Simulations focusing on constant flow rate boundary conditions produced by Soumyajyoti Biswas also confirm how disorder restricts the fracture patterns and extends on the experiments by quantifying the patterns by extracting an order parameter for the type of invasion patterns shown in Fig 5.17. This parameter shows that the transition in invasion pattern, from completely ordered to disordered, occurs in a narrow disorder range which corresponds in the experiments to the systems noted by $rmin = 40$ and $rmin = 35$. However, even at these disorders, this transition is only present for certain choices of pillar heights, as for short pillars the manufacturing tolerance in the pillar sizes means that any fracture-like pattern is restricted. The graph also shows that the order parameter quickly plateaus with increasing disorder as the invading fluid already explores the most of the porous region and therefore further increasing disorder has little effect on how straight the patterns are. In other words, this predicts that the transition in invasion patterns is abrupt as $\frac{\delta \overline{P}}{P_*}$ increases.

Both of these results come from when the invading fluid is injected at a constant flow rate, rather than at a constant pressure. Interestingly, we don't find that fracturing patterns occur under a wide range of parameters in either experiments or simulations, when invasion is run under constant pressure. Under these conditions, thin fingers do appear in certain limits, which could be suggestive of a fracture pattern, but the simulations show that these patterns do not necessarily disappear when the pillars are made completely solid. This indicates that the bending of pillars was not the reason for these invasion patterns, which instead could attributed to the geometry of the system. The reason that fracture patterns occur at constant flow rate and not at constant pressure is possibly that the pressure in the constant flow rate invasion is built up at the tip of the invasion and therefore an avalanche effect occurs, whereby as soon as a finger appears, the flow favours continuing in the direction this finger extends. This is only then restricted when disorder is introduced and the entry pressures of pore throats stops this avalanche effect. However, for constant pressure invasions, the pressure is spread across the interface rather than localized, meaning that an avalanche effect won't occur at the tips and the invading fluid will create large finger patterns.

This new understanding of when fracture patterns occur and how they are restricted by disorder has applications in fracking [109] where a fluid is injected at high pressure to create fractures underground, which allows for oil to be extracted. We have shown that if the disorder within a system is greater than the elasticity of the medium in which the fluid is being injected,

then fractures will not occur.

# Chapter 6

# Summary and Conclusions

Presented in this thesis is a study of complex porous systems and how fluid flows through such a system for both immiscible and miscible fluid-fluid displacement. The work I have done has involved novel experimental techniques which have been developed collaboratively alongside numerical work performed by colleagues. In this work, I have helped show how to characterise disorder in porous media, along with a variety of situations where awareness of such disorder is required to make predictions that go beyond those possible with only knowing macroscopic properties of a system.

In Chapter 3, I introduced the idea of a spatially correlated porous system in the context of fluid-fluid displacement. Here, I looked at how porosity and disorder affects the invasion pattern we see. This tends to be some form of capillary or viscous fingering, depending on how the fluid is injected or the properties of the invading and defending fluids. However, shown along with simulations produced by Oshri Borgman, Enrico Segre and Ran Holtzman, is that for the same overall porosity, positioning the obstacles that make up the porous system near other obstacles similar in size will affect how fluid flows through the system. To investigate this, experimental poly-dimethilsiloxane (PDMS) chips were made using the microfabrication methodology outlined in Chapter 2. This involved pillars situated on a triangular lattice that form a circular cell. Air invades through a central inlet and displaces a water-glycerol mixture as it invades radially outwards through the porous region. The results of these experiments, along with the simulations, show that for the low $Ca$ regime in which the experiments ran, increasing the correlation length reduced trapping, reduced sweep efficiency and lowered the amount of interfacial area. The patterns produced more closely followed the pore geometry and therefore preferred to explore the large areas of open pore throats, rather than more evenly explore the porous region, as was the case for lower correlation length. This shows that knowing the disorder of the system alone is not enough to predict invasion statistics, and that the connectivity of the pores and the spatial distribution of the corresponding pore sizes also needs to be considered.

Explored in Chapter 4, is the effect disorder has on transport phenomena. This builds on Chapter 3, where I considered immiscible fluid-fluid displacement, but now looks at the case where the invading and defending fluids can easily mix together. To investigate how the

95

distribution of pore sizes affects the transport phenomena, for example of a dissolved solute, I use experimental rectangular microfluidic cells which in accompaniment with numerical work on matching geometries performed Felix Meigel and Karen Alim. The PDMS chips in this work, consist of cylindrical pillars positioned randomly within the porous region. To introduce this disorder, all pillars are initially set on a hexagonal lattice, before being randomly shifted from their lattice positions by a percentage of their diameter. This percentage is how disorder is quantified in the system. The chips are initially saturated with plain water, before fluorescein-dyed water is injected into the system. The experiments are housed in a dark box along with a camera and UV light causes the dyed-water to fluoresce so images can be taken. The intensity of the images is calibrated so concentration measurements across areas of the porous medium can be measured. Of interest was how the front of the invading dyed-water changed with increasing disorder. This was measured by taking intensity line profiles along the length of the porous region and examining the point when half the maximum concentration reached halfway across the length of the chip. Interestingly, as consistently shown by both experiments and numerical simulations, was that there was a non-monotonic trend in the front width with increasing disorder. This meant that after a small increase in disorder, the front width of the dyed-water shrank before rapidly increasing for higher disorders. This was shown to be due to how the pores connected with one another, as with a small but finite disorder, the pores more effectively mixed with one another, creating a smoother front. However, as disorder increased, clusters of pores became only accessible to the dyed-water by way of slow diffusion, creating a more jagged flow front. This work has implications for how organisms assemble themselves to efficiently transport nutrients throughout their system [32].

Finally, in Chapter 5, I use novel manufacturing techniques to allow the PDMS pillars that make up the porous region to be elastic enough such that they bend under the pressure incident upon them when a fluid invades. The previous two chapters have explored both miscible and immiscible fluid-fluid displacement. However, the geometry can also be connected by the opening and closing of adjacent pore throats due to the deformation or motion of the obstacles that make up them. To investigate this, I explored two injection methods, first where the invading fluid invades at a constant pressure and then when it invades at a constant flow rate. In contrast to the previous chips made in Chapter 3 and Chapter 4, the pillars here are made such that only one end is fixed and the other end is free to bend as the fluid invades. I also introduce disorder into the system by randomly assigning the pillars a diameter from a uniform distribution, while keeping the average pillar diameter the same for each set of systems. For the constant flow rate experiments, I show that fracture-like patterns occur when the elastic response of the pillars is much greater than the disorder in the system. These patterns are identifiable by

their thin straight fingers that invade only a small amount of the porous region before reaching breakthrough. However, when the disorder of pillars becomes a more significant effect, these fracture patterns are restricted and capillary and viscous fingering patterns begin to appear. Interestingly, the experiments, along with accompanying simulations performed by Soumyajyoti Biswas, Enrico Segre and Ran Holtzman show that these fracturing patterns are much more likely to appear for when the invading fluid is injected at a constant flow rate, and not for constant pressure injections.

What all these projects show is that there are hidden complexities within each system, pertaining to a microscopic characterisation of their inherent disorder, that previously haven't been properly considered when making predictions about fluid invasion into porous media. These complexities show that the connectivity of the pores is a vital part of the geometry in addition to characterising the porosity or disorder of the system. This new understanding of fluid flow in porous media has significance in many applications such oil recovery and the mixing of nutrients in organisms.

# References

[1] K. Grammer and R. Thornhill. Human (Homo sapiens) facial attractiveness and sexual selection: the role of symmetry and averageness. *Journal of comparative psychology (Washington, D.C. : 1983)*, 108(3):233–242, 1994.

[2] Joanna E Scheib, Steven W Gangestad, and Randy Thornhill. Facial attractiveness, symmetry and cues of good genes. Technical report.

[3] C. G. J. Jacobi. Ueber die Figur des Gleichgewichts. *Annalen der Physik und Chemie*, 109(8-16):229–233, 1 1834.

[4] K R Sreenivasan and C Meneveau. The fractal facets of turbulence. *Journal of Fluid Mechanics*, 173:357–386, 1986.

[5] Jun Li and Martin Ostoja-Starzewski. Edges of Saturn's rings are fractal. *SpringerPlus*, 4:158, 4 2015.

[6] Martin Kemp. Leonardo da Vinci's laboratory: studies in flow. *Nature*, (571):322–323, 2019.

[7] Ashwin R Vasavada and Adam P Showman. Jovian atmospheric dynamics: an update after Galileo and Cassini. *Reports on Progress in Physics*, 68(8):1935–1996, 2005.

[8] J Siddique, D Anderson, and Andrei Bondarev. Capillary rise of a liquid into a deformable porous material. *Physics of Fluids*, 21, 1 2009.

[9] Ahmed Niameh Mehdy Alhusseny, Adel Gharib Nasser, and Nabeel M J Al-zurf. High-Porosity Metal Foams: Potentials, Applications, and Formulations. In *Porosity - Process, Technologies and Applications*. 2018.

[10] Kamaljit Singh, Hagen Scholl, Martin Brinkmann, Marco Di Michiel, Mario Scheel, Stephan Herminghaus, and Ralf Seemann. The Role of Local Instabilities in Fluid Invasion into Permeable Media. *Scientific Reports*, 7(1):444, 2017.

[11] Nguyen Lam Quoc Cuong, Nguyen Hong Minh, Hoang Manh Cuong, Phan Ngoc Quoc, Ngo Hoang Van Anh, Nguyen Van Hieu, Nguyen Lam Quoc Cuong, Nguyen Hong Minh, Hoang Manh Cuong, Phan Ngoc Quoc, Ngo Hoang Van Anh, and Nguyen Van Hieu. Porosity Estimation from High Resolution CT SCAN Images of Rock Samples by Using Housfield Unit. *Open Journal of Geology*, 08(10):1019–1026, 9 2018.

[12] A B Abell, K L Willis, and D A Lange. Mercury Intrusion Porosimetry and Image Analysis of Cement-Based Materials. *Journal of Colloid and Interface Science*, 211(1):39–44, 1999.

[13] Binyu Ma, Qinhong Hu, Shengyu Yang, Na Yin, Hongguo Qiao, Tao Zhang, and Mianmo Meng. Multiple Approaches to Quantifying the Effective Porosity of Lacustrine Shale Oil Reservoirs in Bohai Bay Basin, East China. *Geofluids*, 2020:8856620, 2020.

[14] Harald Ibach. *Physics of Surfaces and Interfaces.* Springer, 2006.

[15] John Fanchi. *Principles of Applied Reservoir Simulation.* 3rd edition, 2006.

[16] Eyvind Aker, Knut Jørgen Måløy, and Alex Hansen. Simulating temporal evolution of pressure in two-phase flow in porous media. *Physical Review E*, 58(2):2217–2226, 8 1998.

[17] Abdus Satter and Ghulam M Iqbal. 3 - Reservoir rock properties. In Abdus Satter and Ghulam M Iqbal, editors, *Reservoir Engineering*, pages 29–79. Gulf Professional Publishing, Boston, 2016.

[18] Grunde Løvoll, Yves Méheust, Renaud Toussaint, Jean Schmittbuhl, and Knut Jørgen Måløy. Growth activity during fingering in a porous Hele-Shaw cell. *Physical Review E*, 70(2):26301, 8 2004.

[19] R Hilfer. Capillary number correlations for two-phase flow in porous media. *Physical Review E*, 102(5):53103, 11 2020.

[20] Xiaojing Fu, Luis Cueto-Felgueroso, and Ruben Juanes. Pattern formation and coarsening dynamics in three-dimensional convective mixing in porous media. *Philosophical Transactions of the Royal Society A: Mathematical, Physical and Engineering Sciences*, 371(2004), 12 2013.

[21] Myriam Peyrounette, Yohan Davit, Michel Quintard, and Sylvie Lorthois. Multiscale modelling of blood flow in cerebral microcirculation: Details at capillary scale control accuracy at the level of the cortex. *PLOS ONE*, 13(1):e0189474–, 1 2018.

[22] Paolo Fantinel, Oshri Borgman, Ran Holtzman, and Lucas Goehring. Drying in a microfuidic chip: Experiments and simulations. *Scientific Reports*, 7(1), 12 2017.

[23] Tannaz Pak, Nathaly Lopes Archilha, Iara Frangiotti Mantovani, Anderson Camargo Moreira, and Ian B. Butler. An X-ray computed micro-tomography dataset for oil removal from carbonate porous media. *Scientific Data*, 6, 2019.

[24] Stephen Whitaker. Flow in porous media I: A theoretical derivation of Darcy's law. *Transport in Porous Media*, 1(1):3–25, 1986.

[25] B. Sandnes, E. G. Flekkøy, H. A. Knudsen, K. J. Måløy, and H. See. Patterns and flow in frictional fluid dynamics. *Nature Communications*, 2(1), 2011.

[26] B Sandnes, H A Knudsen, K J Måløy, and E G Flekkøy. Labyrinth Patterns in Confined Granular-Fluid Systems. *Physical Review Letters*, 99(3):38001, 7 2007.

[27] Marek Cieplak and Mark O Robbins. Dynamical transition in quasistatic fluid invasion in porous media. *Phys. Rev. Lett.*, 60(20):2042, 1988.

[28] Marek Cieplak and Mark O Robbins. Influence of contact angle on quasistatic fluid invasion of porous media. *Physical Review B*, 41(16):11508–11521, 6 1990.

[29] Hardik S Patel and Ramakanta Meher. Effect of Heterogeneity on Imbibition Phenomena in Fluid Flow through Porous Media with Different Porous Materials. *Nonlinear Engineering*, 8(1):46–55, 2019.

[30] Haihu Liu, Yonghao Zhang, and Albert J Valocchi. Lattice Boltzmann simulation of immiscible fluid displacement in porous media: Homogeneous versus heterogeneous pore network. *Physics of Fluids*, 27(5):052103, 5 2015.

[31] Ran Holtzman. Effects of Pore-Scale Disorder on Fluid Displacement in Partially-Wettable Porous Media. *Scientific Reports*, 6(1):36221, 2016.

[32] Felix J Meigel and Karen Alim. Flow rate of transport network controls uniform metabolite supply to tissue. *Journal of The Royal Society Interface*, 15(142):20180075, 5 2018.

[33] Idan Tuval, Luis Cisneros, Christopher Dombrowski, Charles W Wolgemuth, John O Kessler, and Raymond E Goldstein. Bacterial swimming and oxygen transport near contact lines. *Proceedings of the National Academy of Sciences of the United States of America*, 102(7):2277, 2 2005.

[34] Y S Lee, W J Song, and J.-Y. Sun. Hydrogel soft robotics. *Materials Today Physics*, 2020.

[35] Luke L M Heaton, Eduardo López, Philip K Maini, Mark D Fricker, and Nick S Jones. Growth-induced mass flows in fungal networks. *Proceedings of the Royal Society B: Biological Sciences*, 277(1698):3265–3274, 11 2010.

[36] Hongtao Sun, Jian Zhu, Daniel Baumann, Lele Peng, Yuxi Xu, Imran Shakir, Yu Huang, and Xiangfeng Duan. Hierarchical 3D electrodes for electrochemical energy storage. *Nature Reviews Materials*, 4(1):45–60, 2019.

[37] A M Tartakovsky, G Redden, P C Lichtner, T D Scheibe, and P Meakin. Mixing-induced precipitation: Experimental study and multiscale numerical analysis. *Water Resources Research*, 44(6), 6 2008.

[38] Alexandre M Tartakovsky and Shlomo P Neuman. Effects of Peclet number on pore-scale mixing and channeling of a tracer and on directional advective porosity. *Geophysical Research Letters*, 35(21), 11 2008.

[39] Reza Barati and Jenn Tai Liang. A review of fracturing fluid systems used for hydraulic fracturing of oil and gas wells, 8 2014.

[40] Ran Holtzman, Michael L Szulczewski, and Ruben Juanes. Capillary Fracturing in Granular Media. *Physical Review Letters*, 108(26):264504, 6 2012.

[41] M Prat. Percolation model of drying under isothermal conditions in porous media. *Int. J. Multiphase Flow*, 19(4):691–704, 1993.

[42] Marc J Madou. *Fundamentals of microfabrication: the science of miniaturization*. CRC press, 2002.

[43] SU8-3000 Data Sheet. Technical report, Kayaku Advanced Materials.

[44] Arnaud Hemmerle, Matthias Schröter, and Lucas Goehring. A cohesive granular material with tunable elasticity. *Scientific Reports*, 6(1):35650, 2016.

[45] O. Borgman, T. Darwent, E. Segre, L. Goehring, and R. Holtzman. Immiscible fluid displacement in porous media with spatially correlated particle sizes. *Advances in Water Resources*, 128, 2019.

[46] Ran Holtzman and Enrico Segre. Wettability stabilizes fluid invasion into porous media via nonlocal, cooperative pore filling. *Phys. Rev. Lett.*, 115(16):164501, 2015.

[47] B N J Persson, O Albohr, U Tartaglino, A I Volokitin, and E Tosatti. On the nature of surface roughness with application to contact mechanics, sealing, rubber friction and adhesion. *Journal of Physics: Condensed Matter*, 17(1):R1–R62, 1 2005.

[48] Caroline A Schneider, Wayne S Rasband, and Kevin W Eliceiri. NIH Image to ImageJ: 25 years of image analysis. *Nature Methods*, 9(7):671–675, 2012.

[49] Koichi Takamura, Herbert Fischer, and Norman R. Morrow. Physical properties of aqueous glycerol solutions. *Journal of Petroleum Science and Engineering*, 98-99:50–60, 11 2012.

[50] V. Joekar-Niasar and S. M. Hassanizadeh. Analysis of Fundamentals of Two-Phase Flow in Porous Media Using Dynamic Pore-Network Models: A Review. *Critical Reviews in Environmental Science and Technology*, 42(18):1895–1976, 9 2012.

[51] Liv Furuberg, Knut Jørgen Måløy, and Jens Feder. Intermittent behavior in slow drainage. *Physical Review E*, 53(1):966–977, 1 1996.

[52] Harris Sajjad Rabbani, Vahid Joekar-Niasar, Tannaz Pak, and Nima Shokri. New insights on the complex dynamics of two-phase flow in porous media under intermediate-wet conditions. *Scientific Reports*, 7(1), 12 2017.

[53] Harris Sajjad Rabbani, Benzhong Zhao, Ruben Juanes, and Nima Shokri. Pore geometry control of apparent wetting in porous media. *Scientific Reports*, 8(1), 12 2018.

[54] Paul Meakin and Alexandre M. Tartakovsky. Modeling and simulation of pore-scale multiphase fluid flow and reactive transport in fractured and porous media. *Reviews of Geophysics*, 47(3), 9 2009.

[55] R. Toussaint, K.J. Måløy, Y. Méheust, G. Løvoll, M. Jankov, G. Schäfer, and J. Schmittbuhl. Two-Phase Flow: Structure, Upscaling, and Consequences for Macroscopic Transport Properties. *Vadose Zone Journal*, 11(3):vzj2011.0123, 8 2012.

[56] Mark L. Porter, Dorthe Wildenschild, Gavin Grant, and Jason I. Gerhard. Measurement and prediction of the relationship between capillary pressure, saturation, and interfacial area in a NAPL-water-glass bead system. *Water Resources Research*, 46(8), 2010.

[57] Yihong Liu, D. D. Nolte, and L. J. Pyrak-Nolte. Hysteresis and interfacial energies in smooth-walled microfluidic channels. *Water Resources Research*, 47(1), 2011.

[58] Pietro De Anna, Marco Dentz, Alexandre Tartakovsky, and Tanguy Le Borgne. The filamentary structure of mixing fronts and its control on reaction kinetics in porous media flows. *Geophysical Research Letters*, 41(13):4586–4593, 7 2014.

[59] Roland Lenormand, Eric Touboul, and Cesar Zarcone. Numerical models and experiments on immiscible displacements in porous media. *Journal of Fluid Mechanics*, 189:165–187, 1988.

[60] Jiří Vymětal and Jiří Vondrášek. Gyration- and Inertia-Tensor-Based Collective Coordinates for Metadynamics. Application on the Conformational Behavior of Polyalanine Peptides and Trp-Cage Folding. *The Journal of Physical Chemistry A*, 115(41):11455–11465, 10 2011.

[61] M Prat and F Bouleux. Drying of capillary porous media with a stabilized front in two dimensions. *Physical Review E*, 60(5):5647–5656, 11 1999.

[62] Suiling Wang and Catherine N Mulligan. An evaluation of surfactant foam technology in remediation of contaminated soil. *Chemosphere*, 57(9):1079–1089, 2004.

[63] Tarek Ahmed. Chapter 14 - Principles of Waterflooding. In Tarek Ahmed, editor, *Reservoir Engineering Handbook (Fourth Edition)*, pages 909–1095. Gulf Professional Publishing, Boston, 2010.

[64] Harihar Rajaram, Lin A. Ferrand, and Michael A. Celia. Prediction of relative permeabilities for unconsolidated soils using pore-scale network models. *Water Resources Research*, 33(1):43–52, 1997.

[65] Martin J Blunt. *Multiphase Flow in Permeable Media: A Pore-Scale Perspective*. Cambridge University Press, Cambridge, 2017.

[66] Zi Li, Sergio Galindo-Torres, Guanxi Yan, Alexander Scheuermann, and Ling Li. A lattice Boltzmann investigation of steady-state fluid distribution, capillary pressure and relative permeability of a porous medium: Effects of fluid and geometrical properties. *Advances in Water Resources*, 116:153–166, 2018.

[67] Karen Alim, Shima Parsa, David A Weitz, and Michael P Brenner. Local Pore Size Correlations Determine Flow Distributions in Porous Media. *Physical Review Letters*, 119(14):144501, 10 2017.

[68] Joaquín Jiménez-Martínez, Pietro De Anna, Hervé Tabuteau, Régis Turuban, Tanguy Le Borgne, and Yves Méheust. Pore-scale mechanisms for the enhancement of mixing in unsaturated porous media and implications for chemical reactions. *Geophysical Research Letters*, 42(13):5316–5324, 7 2015.

[69] Birendra Jha, Luis Cueto-Felgueroso, and Ruben Juanes. Fluid Mixing from Viscous Fingering. *Physical Review Letters*, 106(19):194502, 5 2011.

[70] Tanguy Le Borgne, Timothy R. Ginn, and Marco Dentz. Impact of fluid deformation on mixing-induced chemical reactions in heterogeneous flows. *Geophysical Research Letters*, 41(22):7898–7906, 11 2014.

[71] Christos Nicolaides, Birendra Jha, Luis Cueto-Felgueroso, and Ruben Juanes. Impact of viscous fingering and permeability heterogeneity on fluid mixing in porous media. *Water Resources Research*, 51(4):2634–2647, 4 2015.

[72] Peter K Kang, Marco Dentz, Tanguy Le Borgne, and Ruben Juanes. Anomalous transport on regular fracture networks: Impact of conductivity heterogeneity and mixing at fracture intersections. *Physical Review E*, 92(2):22148, 8 2015.

[73] Maria Pool and Marco Dentz. Effects of Heterogeneity, Connectivity, and Density Variations on Mixing and Chemical Reactions Under Temporally Fluctuating Flow Conditions and the Formation of Reaction Patterns. *Water Resources Research*, 54(1):186–204, 1 2018.

[74] M. Moura, K. J. Måløy, and R. Toussaint. Critical behavior in porous media flow. *Europhysics Letters*, 118(1):14004, 4 2017.

[75] Soumyajyoti Biswas, Paolo Fantinel, Oshri Borgman, Ran Holtzman, and Lucas Goehring. Drying and percolation in correlated porous media. *Physical Review Fluids*, 3(12):124307, 12 2018.

[76] Steffen Schlüter, Jan Vanderborght, and Hans-Jörg Vogel. Hydraulic non-equilibrium during infiltration induced by structural connectivity. *Advances in Water Resources*, 44:101–112, 2012.

[77] Oliver S. Schilling, Dylan J. Irvine, Harrie Jan Hendricks Franssen, and Philip Brunner. Estimating the Spatial Extent of Unsaturated Zones in Heterogeneous River-Aquifer Systems. *Water Resources Research*, 53(12):10583–10602, 12 2017.

[78] Holly A. Michael, Kaileigh C. Scott, Mohammad Koneshloo, Xuan Yu, Mahfuzur R. Khan, and Katie Li. Geologic influence on groundwater salinity drives large seawater circulation through the continental shelf. *Geophysical Research Letters*, 43(20):782–10, 10 2016.

[79] Wendy A. Timms, R. Ian Acworth, Richard A. Crane, Christoph H. Arns, Ji Youn Arns, Dayna E. McGeeney, Gabriel C. Rau, and Mark O. Cuthbert. The Influence of Syndepositional Macropores on the Hydraulic Integrity of Thick Alluvial Clay Aquitards. *Water Resources Research*, 54(4):3122–3138, 4 2018.

[80] Jerome Neufeld and Herbert Huppert. Modelling carbon dioxide sequestration in layered strata. *Journal of Fluid Mechanics*, 625:353–370, 2009.

[81] Michael R. Plampin, Mark L. Porter, Rajesh J. Pawar, and Tissa H. Illangasekare. Intermediate-Scale Experimental Study to Improve Fundamental Understanding of Attenuation Capacity for Leaking CO2 in Heterogeneous Shallow Aquifers. *Water Resources Research*, 53(12):10121–10138, 12 2017.

[82] Bo Liang and Andres F. Clarens. Interactions Between Stratigraphy and Interfacial Properties on Flow and Trapping in Geologic Carbon Storage. *Water Resources Research*, 54(1):72–87, 1 2018.

[83] Hasan A. Nooruddin and Martin J. Blunt. Large-scale Invasion Percolation with Trapping for Upscaling Capillary-Controlled Darcy-scale Flow. *Transport in Porous Media*, 121(2):479–506, 1 2018.

[84] Ali Ebrahimi and Dani Or. On Upscaling of Soil Microbial Processes and Biogeochemical Fluxes From Aggregates to Landscapes. *Journal of Geophysical Research: Biogeosciences*, 123(5):1526–1547, 5 2018.

[85] Joaquín Jiménez-Martínez, Tanguy Le Borgne, Hervé Tabuteau, and Yves Méheust. Impact of saturation on dispersion and mixing in porous media: Photobleaching pulse injection experiments and shear-enhanced mixing model. *Water Resources Research*, 53(2):1457–1472, 2 2017.

[86] Talal T. Al-Housseiny, Peichun A. Tsai, and Howard A. Stone. Control of interfacial instabilities using flow geometry. *Nature Physics*, 8(10):747–750, 2012.

[87] Karen Alim, Gabriel Amselem, François Peaudecerf, Michael P Brenner, and Anne Pringle. Random network peristalsis in Physarum polycephalum organizes fluid flows across an individual. *Proceedings of the National Academy of Sciences of the United States of America*, 110(33):13306–13311, 8 2013.

[88] Mihai Duduta, Bryan Ho, Vanessa C Wood, Pimpa Limthongkul, Victor E Brunini, W Craig Carter, and Yet-Ming Chiang. Semi-Solid Lithium Rechargeable Flow Battery. *Advanced Energy Materials*, 1(4):511–516, 7 2011.

[89] Laurence Belfiore. *Transport Phenomena for Chemical Reactor Design.* 2003.

[90] John Tyler Bonner. *The Biology of Cellular Slime Molds.* Princeton University Press, 2009.

[91] Felix Meigel, Thomas Darwent, Leonie Bastin, Lucas Goehring, and Karen Alim. Transport dynamics in porous media emerge from junction and not pore statistics. *Preprint*, 2021.

[92] Adolf Fick. Ueber Diffusion. *Annalen der Physik und Chemie*, 170(1):59–86, 1855.

[93] Edward Cussler. *Diffusion: Mass Transfer in Fluid Systems.* 2nd edition, 1997.

[94] Geoffrey Ingram Taylor. Dispersion of soluble matter in solvent flowing slowly through a tube. *Proceedings of the Royal Society of London. Series A. Mathematical and Physical Sciences*, 219(1137):186–203, 8 1953.

[95] M Sahimi. *Flow and Transport in Porous Media and Fractured Rock*. Wiley-VCH, 2011.

[96] R. A. Wooding, Scott W. Tyler, and Ian White. Convection in groundwater below an evaporating salt lake: 1. Onset of instability. *Water Resources Research*, 33(6):1199–1217, 1997.

[97] Felix Meigel. *Effect of disorder on dispersive transport in porous media*. MSc Thesis, University of Göttingen, 2019.

[98] Alexander P Demchenko. Photobleaching of organic fluorophores: quantitative characterization, mechanisms, protection. *Methods and Applications in Fluorescence*, 8(2):022001, 2 2020.

[99] Ansys Fluent, Release 19.2.

[100] J Crank and P Nicolson. A practical method for numerical evaluation of solutions of partial differential equations of the heat-conduction type. *Mathematical Proceedings of the Cambridge Philosophical Society*, 43(1):50–67, 1947.

[101] J.R. Lakowicz. Quenching of Fluorescence. In Joseph R Lakowicz, editor, *Principles of Fluorescence Spectroscopy*, pages 277–330. Springer US, Boston, MA, 2006.

[102] Mustafa Arık, Neslihan Çelebi, and Yavuz Onganer. Fluorescence quenching of fluorescein with molecular oxygen in solution. *Journal of Photochemistry and Photobiology A: Chemistry*, 170(2):105–111, 2005.

[103] Amir H Haghi, Stephen Talman, and Richard Chalaturnyk. Consecutive Experimental Determination of Stress-Dependent Fluid Flow Properties of Berea Sandstone and Implications for Two-Phase Flow Modeling. *Water Resources Research*, 56(1):e2018WR024245, 1 2020.

[104] Bezalel Haimson and Charles Fairhurst. Hydraulic Fracturing in Porous-Permeable Materials. *Journal of Petroleum Technology*, 21(07):811–817, 7 1969.

[105] James Gere and Barry Goodno. *Mechanics of Materials*. Cengage Learning, 2012.

[106] Glenn O Brown. The History of the Darcy-Weisbach Equation for Pipe Flow Resistance. In *Environmental and Water Resources History*, pages 34–43. 2012.

[107] Oshri Borgman. *A pore-scale study of the effects of heterogeneity and deformation on fluid displacement in granular media*. PhD thesis, The Hebrew University of Jerusalem, 2018.

[108] Cargille Laboratories. Refractive Index Liquids Series A n=1.6320, 2018.

[109] J D Hyman, J Jiménez-Martínez, H S Viswanathan, J W Carey, M L Porter, E Rougier, S Karra, Q Kang, L Frash, L Chen, Z Lei, D O'Malley, and N Makedonska. Understanding hydraulic fracturing: a multi-scale problem. *Philosophical Transactions of the Royal Society A: Mathematical, Physical and Engineering Sciences*, 374(2078):20150426, 10 2016.